Master Thesis

A Study on New Developments and Chemical Time Scale Definitions for the Eddy Dissipation Concept

carried out for the purpose of obtaining the academic degree

Diplom-Ingenieur (Dipl.-Ing.)

submitted at TU Wien
Faculty of Mechanical and Industrial Engineering

by

Eva-Maria Wartha
Matr.Nr.: 01208963

under the supervision of

Ass.Prof. Dipl.-Ing. Dr.techn. Michael Harasek
and
Projektass. Dipl.-Ing. Markus Bösenhofer

Institute of Chemical, Environmental and Biological Engineering
E166

Affidavit

I confirm, that going to press of this thesis needs the confirmation of the examination committee.

I, Eva-Maria Wartha, declare in lieu of oath

1. that I wrote this thesis and performed the associated research myself, using only literature cited in this volume. If text passages from sources are used literally, they are marked as such.

2. that this work is original and has not been submitted elsewhere for any examination nor is it currently under consideration for a thesis elsewhere.

Vienna, 15.11.2017 Eva-Maria Wartha

Danksagung

Vielen Dank an Markus Bösenhofer, der durch seine Idee zu dieser Arbeit, diese zuallererst einmal ermöglicht hat. Dank seiner Motivation und Begeisterung für das Thema, wurde ich auch selbst immer wieder motiviert und war angespornt neues herauszufinden und auszuprobieren. Ohne seine stetige Unterstützung und Diskussionsbereitschaft wäre diese Arbeit wohl nie gelungen.

Außerdem möchte ich mich bei Michael Harasek bedanken, für die Möglichkeit meine Diplomarbeit in seiner Arbeitsgruppe durchzuführen, für den fachlichen Rat, der bei Bedarf immer bereitgestellt wurde und auch für die Freiheit, so zu arbeiten, wie ich es für richtig hielt.

Meine Dankbarkeit gilt auch der gesamten Arbeitsgruppe, die mich sehr herzlich aufgenommen hat und in der jeder bereit war zu helfen, sollte dies notwendig sein. Ganz besonders möchte ich hier auch meine netten Kollegen aus dem "CFD-Kammerl" erwähnen, die die Zeit meiner Diplomarbeit zu einer besonderen gemacht haben und durch die ich zumindest eines gelernt habe: Tischfußball zu spielen (oder zumindest zu verlieren).

Vielen Dank auch an Markus Deutsch, der sich nicht nur die Mühe gemacht hat, die Arbeit sorgfältigst zu lesen, sondern auch immer als Berater bei tikz-Problemen zur Verfügung stand.

Das beste an jedem Studium sind ganz einfach die Freunde, die man gewinnt. Deshalb vielen Dank an meine Fußball spielenden Kollegen - auch wenn ich schon manchmal abgeschossen wurde - und natürlich am wichtigsten: vielen herzlichen Dank an die Bierdienstagsrunde, auf die man immer zählen kann!

Ein riesiges Dankeschön geht natürlich an meine Familie. An meinen Vater, der Mitschuld an meinem Verfahrenstechnik Studium trägt, an meine Mutter, die dann manchmal die fachlichen Diskussionen am Mittagstisch ertragen musste und selbstverständlich an meine Schwester, die immer zu mir hält.

Zum Schluss möchte ich noch einem wichtigen Menschen in meinem Leben danken. Ich bin mir zwar nicht sicher ob seine Diplomarbeit mir mehr Nerven gekostet hat als meine eigene, aber er war immer für mich da und hat meine schlechte Laune genauso ertragen, wie sich mit mir gefreut, wenn eine Flamme nun endlich zündet und etwas funktioniert. Danke, Daniel.

Abstract

Combustion is important for humans since early days, but there are still phenomena we do not understand. Under the rising pressure of global warming a profound understanding of combustion processes is necessary to reduce emissions and improve efficiency.

Computational fluid dynamics (CFD) can be a great tool to investigate those phenomena and test certain scenarios with reduced effort. Therefore, it is important to have well calibrated simulation models. The eddy dissipation concept (EDC) is a valuable concept for simulating combustion, since it can predict combustion where mixing as well as reaction is determining. The EDC models the interaction between turbulence and chemical reactions. Any turbulence model can be applied with it. Although it has been developed over the years, there is still research on it. Recently some modifications for the application to moderate or intense low-oxygen dilution (MILD) combustion have been suggested. The goal of this thesis was to improve the EDC with regard to numerical performance and to widen the application field with suggested modifications.

For computational improvement, operator splitting was tested for splitting the descriptive ordinary differential equation (ODE)-system of the reacting parts into a chemical term and a mixing term. Through the application of operator splitting, the usage of in-situ adaptive tabulation (ISAT) is enabled. Different operator splitting methods were tested on sample problems and the best one, Strang splitting, was used for the simulation of Flame D, a piloted methane-air jet flame developed by Sydney University, to validate the solver in OpenFOAM. The results reveal that operator splitting with and without ISAT is working and gives improved predictions compared to using a global mechanism. However, there are drawbacks compared to direct integration with the detailed mechanism.

Besides improvements regarding numerical issues, also changes of EDC model constants have been suggested in literature. The newly derived relations for the EDC constants depend on the Damköhler number. The Damköhler number describes the relation between a mixing time scale and a chemical time scale. Therefore, a proper definition of a characteristic chemical time scale is necessary. Different time scale definitions were discussed and tested on sample problems. The most promising were also applied to compute the Damköhler number for Flame D. Three of the presented definitions (Ren's, Ren's product and system progress time scale (SPTS)), give promising results and one of those should be used for the calculation of the suggested modified constants in the EDC.

Kurzfassung

Menschen nutzen Verbrennung seit Jahrtausenden und trotzdem gibt es noch immer unergründete Mechanismen und Vorgänge. Aufgrund steigenden wirtschaftlichen Drucks und auch durch den Zwang Emissionen zu minimieren, ist es wichtig Verbrennungsmechanismen zu verstehen um Verbrennungsprozesse zu optimieren.

Mit Hilfe von Simulationen können Mechanismen aufgeklärt und verschiedene Szenarien mit geringem Aufwand untersucht werden. Das eddy dissipation concept (EDC) ist ein wichtiges Model, dass die Wechselwirkung zwischen Turbulenz und Reaktion darstellen kann. Neueste Bestrebungen gehen dahin, die Anwendbarkeit des EDC auch für nicht turbulente Verbrennungsregime zu gewährleisten. Außerdem wird versucht, die Prädiktion von langsamen Reaktionen, wie der NO_x Bildung, zu verbessern. Das Ziel dieser Arbeit war das EDC sowohl numerisch zu verbessern als auch dessen Anwendungsbereich durch in der Literatur vorgeschlagene Modifikationen zu vergrößern.

Um die Anwendung des EDC numerisch zu verbessern, wurde die Möglichkeit des Operator Splitting untersucht. Dieses teilt gewöhnliche Differentialgleichungen in zwei Teile, um diese separat zu lösen und so einen numerisch einfacheren Lösungsvorgang zu ermöglichen. Dies kann auf das Differentialgleichungssystem angewandt werden, welches die reaktiven Strukturen beschreibt. Dabei wird die Differentialgleichung in einen Mischungs- und einen Reaktionsterm aufgeteilt und ermöglicht sogleich die Anwendung von in-situ adaptiver Tabulation für den Reaktionsterm. Diese Methoden wurden anhand von Simulationen einer turbulenten Flamme, der Sandia Flame D, in OpenFOAM getestet. Die Simulationen zeigen gute Ergebnisse, aber direkte Integration gibt etwas genauere Vorhersagen.

Abgesehen von diesen numerischen Verbesserungen, wurden modifizierte EDC Konstanten in Abhängigkeit der turbulenten Damköhler- und der turbulenten Reynoldszahl in der Literatur vorgeschlagen. Die turbulente Damköhlerzahl ist durch das Verhältnis von chemischer Zeitskala und Mischungszeitskala definiert. Die größte Schwierigkeit stellt hierbei die Berechnung der chemischen Zeitskala dar. Eine genaue und möglichst einfache Berechnungsmöglichkeit für die chemische Zeitskala musste gefunden werden, um die Anwendbarkeit der modifizierten EDC Konstanten zu gewährleisten. Verschiedene Definitionen wurden getestet und es hat sich gezeigt, dass für die Anwendung drei Methoden (Ren's, Ren's product und system progress time scale (SPTS)) akkurate Ergebnisse bei vertretbarem Aufwand liefern.

Contents

Contents

1 Introduction

1.1 Motivation and Problem Statement

Combustion is an important part of many processes in the field of chemical engineering, for example in gasifiers, blast furnaces or waste incineration plants. A better understanding of those processes is helpful, or even needed, due to the enforced environmental standards or the rising pressure of economical performance. Simulations are an important tool here. They are relatively cheap, can predict plant behavior and can reveal non-observable mechanisms, if tuned correctly.

One concept to simulate turbulent reacting flows, is the eddy dissipation concept (EDC), which was presented by Magnussen (1981) and has been further developed by himself, ((Magnussen 1989a), (Magnussen 2005)), and others, e.g. (Parente et al. 2015). The idea of the EDC is that a reacting fluid consists of two distinct regions: the fine structures and the surroundings. The educts react in the fine structures, because only there, they are mixed at a molecular scale. The reactions in the fine structures can be modeled by global chemical mechanisms. This gives quite good results for simple standard cases, but lacks accuracy when predicting combustion with more complex settings. For example for moderate or intense low-oxygen dilution (MILD) conditions or when the slow NO_x formation should be predicted, (Lilleberg et al. 2013) and (Lysenko et al. 2014b), the results obtained by the EDC are erroneous.

Instead of using global mechanisms, also detailed chemical mechanisms can be used. The fine structures can be expressed as perfectly stirred reactors, which are described by an ordinary differential equation (ODE)-system of the size proportional to the number of species. Therefore, the computational expense increases drastically with increasing complexity of the chemical mechanisms, i.e. with increasing number of species in the system.

To improve the application of detailed chemical mechanisms with the EDC, operator splitting can be used to facilitate the integration of the ODE-system. Operator splitting splits an ODE in two ODEs, which are usually easier to solve, and solves them separately to obtain the solution. Furthermore, in-situ adaptive tabulation (ISAT) can then be used for tabulating the chemistry term. Tables for the whole ODE would become too big and not bring any improvement compared to direct integration, (Pope 1997) and (Rehm 2010).

Modifications of EDC parameters have been suggested promising improvements,

especially with regard to slower reactions and MILD conditions, (Parente et al. 2015) and (Bao 2017). The modified formulations of the EDC include the turbulent Damköhler number, which is the ratio of a turbulent mixing time scale and a chemical time scale. The knowledge of this characteristic chemical time scale is a prerequisite of the application of those modifications. In big processes, such as a blast furnace, combustion within different regimes can occur. Therefore, it is necessary to adapt the EDC depending on mixing or reaction controlled combustion. This is indicated by the Damköhler number, i.e. by the chemical time scale.

1.2 Aim of the Work

As mentioned before, operator splitting is necessary for the proper usage of ISAT within the EDC. Therefore, different operator splitting mechanisms are investigated and tested on sample problems to identify the most suitable for the usage with the EDC.

The identified method will then be used with a newly developed EDC solver in OpenFOAM for the simulation of Sandia Flame D. Measurement data for this turbulent, premixed flame is available from Barlow et al. (2005) and Schneider et al. (2003). Consequently, the implemented operator splitting and the usage of ISAT will be tested compared to other simulation data as well as to experimental data.

To apply the suggested constant modifications by (Parente et al. 2015) and (Bao 2017), the definition of a characteristic chemical time scale of the reacting system is crucial. To find a suitable time scale definition, a literature survey is conducted and the chosen calculation methods are tested on sample problems to check their applicability for the EDC.

Furthermore, the suitable time scale definitions will be applied for the calculation of the Damköhler number of Flame D. This is the first essential step for the usage of the EDC with modifiable constants.

2 Theory

2.1 Turbulence Modeling

2.1.1 General remark

The EDC describes the interaction between turbulence and chemical reactions in combustion processes. When using the EDC, the turbulence still needs to be modeled by some turbulence model, see section 2.2. Direct numerical simulation (DNS), large eddy simulation (LES) and reynolds averaged navier-stokes equations (RANS) are the three main concepts of turbulence modeling.

DNS is the computationally most expensive, since the Navier-Stokes equations are solved directly to compute a transient velocity field, (Pope 2000). The computational cost increases with Re^3 and is, therefore, only used for moderately turbulent flows, (Pope 2000).

LES resolves only the large scales when solving the Navier-Stokes equations. The influence of the smaller ones is modeled.

RANS models only solve the equations for averaged quantities. Since the computational expense for the RANS models is way less and they still give quite good results, they will be used in conjunction with the EDC in this work. RANS models can be further divided into different groups of models based on the number of equations to be solved in addition to the conservation of mass, momentum and energy, (Wilcox 1993).

The standard and the realizable k-ϵ model are two widely used two-equation models, which will be used in this work. They have often been used for the purpose of combustion simulation and have shown good results with the EDC, see (Zahirović et al. 2010). Therefore, they are described in the following sections. The Boussinesq hypothesis is the basis of these models and, hence, is described in section 2.1.2

2.1.2 Boussinesq hypothesis

The Boussinesq assumption suggests, that the turbulent shear stresses are related to the rate of mean strain through a turbulent viscosity, (Boussinesq 1877). Through the Boussinesq approximation the Reynolds stress tensor is formulated as shown in equation 2.1, where μ_{turb} is the turbulent viscosity, k is the turbulent kinetic energy and S_{ij} is the rate of the mean strain tensor (equation 2.2). Turbulence

models closing the Reynolds equations with the Boussinesq hypothesis are called turbulent viscosity models.

$$-\overline{\rho u_x' u_y'} = 2\mu_{\text{turb}} S_{ij} - \frac{2}{3}\delta_{ij}\left(\mu_{\text{turb}}\frac{\partial u_z}{\partial z} + \rho k\right) \tag{2.1}$$

$$S_{ij} = \frac{1}{2}\left(\frac{\partial u_x}{\partial y} + \frac{\partial u_y}{\partial x}\right) \tag{2.2}$$

2.1.3 Standard k-ϵ model

The standard k-ϵ model uses the Boussinesq hypothesis and, therefore, belongs to the group of turbulent viscosity models. This model is also a two-equation model because two additional transport equations are solved to describe the turbulence. Those two equations are the one for the turbulent kinetic energy k and for the dissipation rate ϵ (equations 2.3 and 2.4). This model was mainly developed from Jones and Launder (1972). In the k-ϵ model, the turbulent viscosity μ_{turb} is evaluated by k and ϵ (equation 2.5).

$$\rho\frac{\mathrm{D}k}{\mathrm{D}t} = \frac{\partial}{\partial y}\left[\left(\mu + \mu_{\text{turb}}/\,\mathrm{Pr}_{\mathrm{k}}\right)\frac{\partial k}{\partial y}\right] + \left(2\mu_{\text{turb}} S_{ij} - \frac{2}{3}\rho k\delta_{ij}\right)\frac{\partial u_i}{\partial y} - \rho\epsilon \tag{2.3}$$

$$\rho\frac{\mathrm{D}\epsilon}{\mathrm{D}t} = \frac{\partial}{\partial y}\left[\left(\mu + \mu_{\text{turb}}/\,\mathrm{Pr}_{\varepsilon}\right)\frac{\partial \epsilon}{\partial y}\right] + \mathrm{C}_{\varepsilon 1}\frac{\epsilon}{k}\left(2\mu_{\text{turb}} S_{ij} - \frac{2}{3}\rho k\delta_{ij}\right)\frac{\partial u_i}{y} - \mathrm{C}_{\varepsilon 2}\rho\frac{\epsilon^2}{k} \tag{2.4}$$

$$\mu_{\text{turb}} = \mathrm{C}_{\eta}\rho\frac{k^2}{\epsilon} \tag{2.5}$$

The terms in the model equation for the dissipation rate (equation 2.4) on the right-hand side are analogous to diffusion, generation and dissipation rates of ϵ, (Tannehill et al. 1984). Table 2.1 shows the standard values for the model parameters of the above equations (2.3 and 2.4). The k-ϵ model does not describe the viscous sublayer well, therefore, the law of the wall or wall functions can be used to model the near-wall region. They have been presented for example by Launder and Spalding (1974).

Table 2.1: Standard model constants for the k-ϵ model (Tannehill et al. 1984)

C_{η}	$\mathrm{C}_{\varepsilon 1}$	$\mathrm{C}_{\varepsilon 2}$	Pr_{k}	$\mathrm{Pr}_{\varepsilon}$
0.09	1.44	1.92	1.0	1.3

2.1.4 Realizable k-ϵ model

The realizable k-ϵ model is an improved version of the standard k-ϵ model, see section 2.1.3. It was first introduced by Shih et al. (1995b). The dissipation rate equation and the eddy viscosity formulation were changed compared to the standard k-ϵ model. An improvement over the standard k-ϵ model can be achieved for certain flows, (Shih et al. 1995b), e.g. rotating homogeneous shear flows, boundary-free shear flows including a mixing layer or a channel flow, (Shih et al. 1995b).

The main differences between the standard and the realizable k-ϵ model are found in the equations of the energy dissipation rate (equation 2.6) and in the definition of the model constant C_η (equations 2.8 to 2.13). The equation for the dissipation rate for the realizable k-ϵ model has been derived based on the exact equation for the transport of the mean-square vorticity fluctuation, (Shih et al. 1995b).

The originally constant C_η, used for the turbulent viscosity calculation, is now modeled through the mean strain tensor S_{ij}, the mean rotation rate Ω_{ij}, the turbulent kinematic energy k, the dissipation rate ϵ and a constant A_0, (Shih et al. 1995a), (equation 2.8). The modeling equations are shown in equations 2.9 to 2.13. A more detailed description and the derivation of the equations can be found in (Shih et al. 1995b). The standard values for the constants occuring in this formulation are the same as for the standard k-ϵ model (Table 2.1).

$$\rho\frac{\mathrm{D}\epsilon}{\mathrm{D}t} = \frac{\partial}{\partial y}\left[\left(\mu + \mu_{\mathrm{turb}}/\,\mathrm{Pr}_\epsilon\right)\frac{\partial\epsilon}{\partial y}\right] + C_1\rho S\epsilon - C_{\epsilon 2}\rho\frac{\epsilon^2}{k+\sqrt{\nu\epsilon}} + S_\epsilon \tag{2.6}$$

$$C_1 = \max\left(0.43, \frac{\eta}{5+\eta}\right) \tag{2.7}$$

$$C_\eta = \frac{1}{A_0 + A_s U^{(\star)}\frac{k}{\epsilon}} \tag{2.8}$$

$$U^{(\star)} = \sqrt{S_{ij}S_{ij} + \tilde{\Omega}_{ij}\tilde{\Omega}_{ij}} \tag{2.9}$$

$$\begin{aligned}\tilde{\Omega}_{ij} &= \Omega_{ij} - 2\epsilon_{ijk}\omega_k \\ \Omega_{ij} &= \bar{\Omega}_{ij} - \epsilon_{ijk}\omega_k\end{aligned} \tag{2.10}$$

$$A_0 = 4.04 \tag{2.11}$$

$$A_s = \sqrt{6}\cos\left(\frac{1}{3}\cos^{-1}\left(\sqrt{6}W\right)\right) \tag{2.12}$$

$$W = \frac{S_{ij}S_{jk}S_{ki}}{S^3}$$
$$S = \sqrt{S_{ij}S_{ij}} \tag{2.13}$$

2.2 The Eddy Dissipation Concept

2.2.1 General remark

The EDC presents a link between turbulence and combustion. Magnussen (1975) observed that reactions occur only in the smallest eddies in a turbulent flame and build the EDC based on this observation. The idea is that a reacting fluid consists of two types of regions: the fine structures and the surroundings, schematically shown in Figure 2.1. The components only react in the fine structures, because they are mixed at a molecular scale there. In the surrounding structures no reactions take place. Reaction products and educts are transferred between the surroundings and the fine structures due to turbulent mixing. This mass transfer is modeled based on a turbulence energy cascade, which will be described in section 2.2.2. The EDC was, and is, widely used since it was first presented. It has been improved and modified over the years. The original EDC from Magnussen (1981) will be presented in section 2.2.3. Its modifications are discussed in the sections 2.2.4 and 2.2.5.

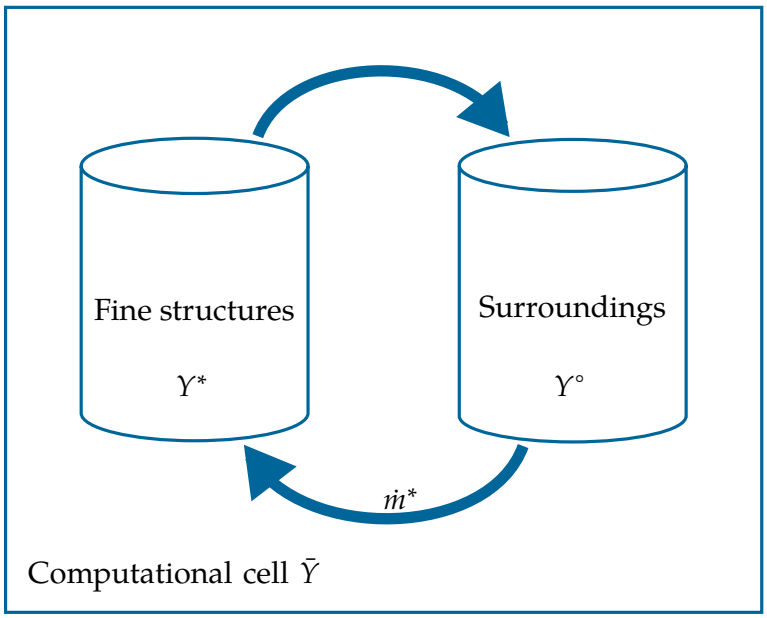

Figure 2.1: Schematic illustration of the EDC, adapted from (Rehm 2010)

In recent studies, the EDC was applied to MILD combustion regimes, revealing

that liftoff heights and temperatures are over predicted, (Christo and Dally 2005) and (Parente et al. 2015). In order to extend the validity of the EDC to MILD combustion, modifications of the model constants in the EDC have been proposed. These modifications will be discussed in the sections 2.2.6 and 2.2.7.

The EDC defines the size of the fine structures and the residence time in those. The reactions in the fine structures have to be modeled. Originally, the idea was to use a "mixed is burnt"-concept for the fine structures. This means that all the reaction educts entering the fine structures immediately react and are converted to products. This approach fails to predict reactions other than one or two-step global reactions, since it does not account for kinetic effects. Therefore, other fine structure models have been developed. The different approaches for fine structure modeling will be described in section 2.2.8.

2.2.2 Turbulence energy cascade

Turbulent flows contain a spectrum of differently sized eddies. Energy is transferred from the big to the small eddies, while a small fraction of energy is dissipated at each level, (Magnussen 1981). In the energy cascade, each level is characterized by a characteristic length, velocity and strain rate ($L^{'}$, $u^{'}$, $\omega^{'}$). The first level, depicted by $'$, contains the whole spectrum of eddies. The succeeding levels include the smaller eddies of the preceding levels until only the smallest eddies are contained in the fine structure level. The fine structure level, denoted by $*$, is the level, where all the kinetic energy is dissipated. This energy cascade is schematically shown in Figure 2.2.

Through the modeling of the energy transfer between all the levels, the energy transfer to the fine structures is obtained. This is calculated by the fine structure velocity and the fine structure length (equation 2.14). The dissipation into heat and the dissipation of turbulent kinetic energy can also be expressed by the characteristic velocity, length, viscosity and a constant ξ (usually set to 0.18), see equations 2.15 and 2.16. In (Magnussen 1981) the energy cascade is discussed in detail and compared to measurement data.

The characteristic length of the fine structures L^* is of the same order of magnitude as the Kolmogorov length scale η, (Magnussen 1981). The Kolmogorov length scale is defined as a ratio of viscosity and turbulent energy dissipation, given in equation 2.19, (Kolmogorov 1890).

$$w^* = \xi_{\zeta} 6 \frac{u^*}{L^*} u^{*2} \tag{2.14}$$

$$\hat{q}^* = \xi_{\zeta}^2 15 \nu \left(\frac{u^*}{L^*} \right)^2 \tag{2.15}$$

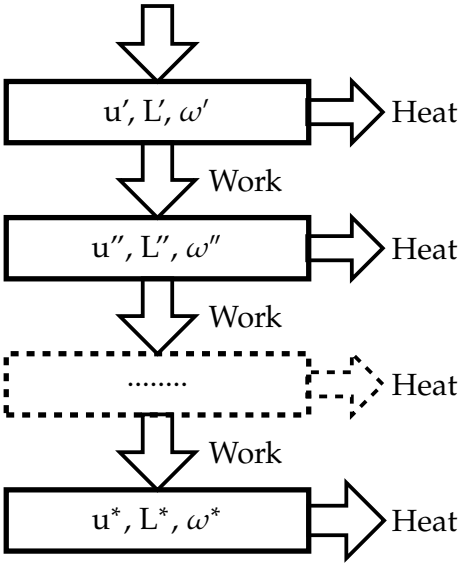

Figure 2.2: Energy cascade model, adapted from (Magnussen 1981)

$$\epsilon = \frac{3}{2} C_{D1} \frac{u'^3}{L'} = 2 C_{D1} \frac{u^{*3}}{L^*} = \frac{4}{3} C_{D2} \nu \left(\frac{u^*}{L^*} \right)^2 \tag{2.16}$$

$$u^* = 1.74 \, (\epsilon \nu)^{\frac{1}{4}} \tag{2.17}$$

$$L^* = 1.43 \frac{\nu^{\frac{3}{4}}}{\epsilon^{\frac{1}{4}}} \tag{2.18}$$

$$\eta = \left(\frac{\nu^3}{\epsilon} \right)^{\frac{1}{4}} \tag{2.19}$$

2.2.3 Original version

Characteristics of the fine structures

Based on the energy cascade, section 2.2.2, Magnussen (1981) presents the mass fraction γ^*, which is occupied by the fine structures (equation 2.20). The mass fraction is modeled as ratio of the characteristic speed of the fine structures and of the first energy level. Thus, an expression based on k, ν and ϵ can be formulated. Assuming the fine structures to be in nearly constant energy regions, the mass fraction occupied by the fine structure region is expressed as γ_L (equation 2.21), (Magnussen 1981). Furthermore, the mass transfer between the fine structures and the surroundings in relation to the fine-structure mass is given in equation 2.22 as twice the ratio of the fine structures' speed and the fine structures' length. Closely related is the fine-structures residence time τ^* (equation 2.23), which is the inverse of the mass transfer rate. The mass transfer per unit of mass of the fine structures

can be transformed to the mass transfer per unit of mass of fluid by multiplication with the fine structure mass fraction (equation 2.24).

$$\gamma^* = \left(\frac{u^*}{u'}\right)^3 = {C_\gamma}^3 \left(\frac{\nu\epsilon}{k^2}\right)^{\frac{3}{4}} \tag{2.20}$$

$$\gamma_L = (\gamma^*)^{\frac{1}{3}} = C_\gamma \left(\frac{\nu\epsilon}{k^2}\right)^{\frac{1}{4}} \tag{2.21}$$

$$\dot{m}^* = 2\frac{u^*}{L^*} = \frac{1}{C_\tau}\left(\frac{\epsilon}{\nu}\right)^{\frac{1}{2}} \tag{2.22}$$

$$\tau^* = C_\tau \left(\frac{\nu}{\epsilon}\right)^{\frac{1}{2}} = \frac{1}{\dot{m}^*} \tag{2.23}$$

$$\dot{m} = \gamma^* \dot{m}^* \tag{2.24}$$

The constants C_γ and C_τ can be related to the constants of the energy cascade C_{D1} and C_{D2}. Their values were presented by (Magnussen 1981) and (Magnussen 1989a), (equations 2.25 and 2.26). The Reynolds number of the fine structures, Re^*, can also be expressed by the constants C_{D1} and C_{D2} (equation 2.27).

$$C_\gamma = \left(\frac{3C_{D2}}{4{C_{D1}}^2}\right)^{\frac{1}{4}} \tag{2.25}$$

$$C_\tau = \left(\frac{C_{D2}}{3}\right)^{\frac{1}{2}} \tag{2.26}$$

$$Re^* = \frac{u^* L^*}{\nu} = \frac{2}{3}\frac{C_{D2}}{C_{D1}} \tag{2.27}$$

Molecular mixing and reaction processes

The mass transfer rate between a fraction χ of the fine structures and the surroundings is given by equation 2.28. Expressing the mass transfer rate per unit volume in the fine structure fraction, the equation evolves to the following expression: equation 2.29, (Magnussen 1981). R_i^* is expressed through the concentration in the fine structures and the surroundings, the mass transfer rate and the fraction of the reacting fine structures. The mass transfer rate related to the average quantities of the domain, is denoted by $\bar{R}_i$ and defined similarly as R_i^* (equation 2.30). To calculate the characteristics of the surrounding or the fine structures, e.g. $\overset{\circ}{c}$, the relationship, respectively the mathematical link, between the surroundings, $^\circ$, the fine structures, $*$, and the mean cell value, $\bar{}$, is important (equation 2.31).

$$R_i = \dot{m}\chi\left(\frac{\overset{\circ}{c_i}}{\overset{\circ}{\rho}} - \frac{c_i^*}{\rho^*}\right) \tag{2.28}$$

$$R_i^* = \frac{\dot{m}\rho^*}{\gamma_L^3}\left(\frac{c_i^\circ}{\rho^\circ} - \frac{c_i^*}{\rho^*}\right) = \frac{\dot{m}^*\gamma_L^3\rho^*}{\gamma_L^3}\left(\frac{c_i^\circ}{\rho^\circ} - \frac{c_i^*}{\rho^*}\right) \tag{2.29}$$

$$\bar{R}_i = \frac{\bar{\rho}\dot{m}^*\gamma_L^3\chi}{(1-\gamma_L^3\chi)}\left(\frac{\bar{c}_i}{\bar{\rho}} - \frac{c_i^*}{\rho^*}\right) \tag{2.30}$$

$$\bar{\psi} = \gamma^*\chi\psi^* + (1-\gamma^*\chi)\psi^\circ \tag{2.31}$$

2.2.4 Modification 1989

Since the original EDC version, section 2.2.3, underestimates the reactions in the tail of diffusion and premixed flames, Magnussen (1989a) proposed a slight modification of the mean reaction rate. This should take into account that more non-reacted fluid is entrained in the fine structures. The new expressions for the transfer rates are given in equations 2.32 and 2.33. When compared with the original expressions in equations 2.28 and 2.29, the difference is that ${\gamma_L}^2$ is used instead of ${\gamma_L}^3$ in the conversion of $\dot{m}^*$ to $\dot{m}$.

In addition to this modification the equation for the energy balance, equation 2.34 is also proposed in Magnussen (1989a), which has to be solved in addition to the species balances for the fine structures.

$$\bar{R}_i = \frac{\bar{\rho}\dot{m}^*(\gamma^*)^{\frac{2}{3}}\chi}{(1-\gamma^*\chi)\gamma_L}\left(\frac{\bar{c}_i}{\bar{\rho}} - \frac{c_i^*}{\rho^*}\right) = \frac{\bar{\rho}\dot{m}^*\gamma_L^2\chi}{(1-\gamma_L^3\chi)}\left(\frac{\bar{c}_i}{\bar{\rho}} - \frac{c_i^*}{\rho^*}\right) \tag{2.32}$$

$$R_i^* = \frac{\rho^*\dot{m}^*}{(1-\gamma_L^3\chi)\gamma_L}\left(\frac{\bar{c}_i}{\bar{\rho}} - \frac{c_i^*}{\rho^*}\right) \tag{2.33}$$

$$\hat{q}^* = \frac{\rho^*\dot{m}^*}{1-\gamma_L^3\chi}\sum_1^{n_s}\left(\frac{\bar{c}_i}{\bar{\rho}}\bar{h}_i - \frac{c_i^*}{\rho_i^*}h_i^*\right) \tag{2.34}$$

2.2.5 Modification 2005

Magnussen (2005) proposed a modification to take into account the possible extension of the reaction space to the surroundings. The definition of γ^* was changed from γ_L^3 to γ_L^2. This results in a modified expression for the transfer rate $\bar{R}_i$ (equation 2.35). It tries to improve the predictions of the EDC by increasing the mean reaction rate, in the same manner as the modification in section 2.2.4, but to a wider extend. More details about the argumentation are presented in (Magnussen 2005).

$$\bar{R}_i = \frac{\bar{\rho}\dot{m}^*\gamma_L^2\chi}{1-\gamma_L^2\chi}\left(\frac{\bar{c}_i}{\bar{\rho}} - \frac{c_i^*}{\rho^*}\right) \tag{2.35}$$

2.2.6 Extended EDC by Parente

To improve the predictions from the EDC for MILD combustion regimes, several authors, including Evans et al. (2015) and Mardani (2017) proposed to modify the model constants C_τ and C_γ. The modifications in these papers were found empirically. Parente et al. (2015) proposed modifications of C_τ and C_γ based on physical relations.

Two dimensionless numbers which characterize turbulent (reacting) flows are used here: the Kolmogorov Damköhler number and the turbulent Reynolds number. The Kolmogorov Damköhler number describes the relation between the Kolmogorov time scale and the chemical time scale (equation 2.36). The turbulent Reynolds number is defined by the turbulent kinetic energy, the viscosity and the energy dissipation rate (equation 2.37).

The expression for the energy dissipation rate derived with the energy cascade (equation 2.16) is reformulated using the assumption that the turbulent flame speed S_{turb} is approximately the fine structures' velocity u^*. The turbulent flame speed can be expressed by the turbulent viscosity and the viscosity or by the turbulent Reynolds number (defined in equation 2.37) and the laminar flame speed (equation 2.40), (Damköhler 1940). Those relations lead to an expression for the dissipation rate depending on the turbulent Reynolds number, the laminar flame speed, the constant C_{D2}, the viscosity and the fine structures' length (equation 2.41).

$$\text{Da}_\eta = \frac{\tau_\eta}{\tau_{\text{che}}} \tag{2.36}$$

$$\text{Re}_{\text{turb}} = \frac{k^2}{\nu\epsilon} \tag{2.37}$$

$$\tau_{\text{che}} = \frac{L^*}{S_{\text{lam}}} \tag{2.38}$$

$$\tau_\eta = \sqrt{\frac{\nu}{\epsilon}} \tag{2.39}$$

The definition of those dimensionless numbers (the turbulent Reynolds number and the Kolmogorov Damköhler number) and the definition of the chemical time scale as the relation between fine structure length and laminar flame speed (equation 2.38) are used to further modify the expression for ϵ (equation 2.41). The revised expression for the energy dissipation rate ϵ and the formulation for the Kolmogorov time scale, based on the viscosity and the energy dissipation rate (equation 2.39) lead to the equation for C_{D2} (equation 2.42). Using the relationship between the constants C_{D2} and C_τ (equation 2.26) a relation for C_τ is obtained (equation 2.43).

$$S_{\text{turb}} \approx \sqrt{\frac{\nu_{\text{turb}} + \nu}{\nu}} \approx S_{\text{lam}} \sqrt{\text{Re}_{\text{turb}} + 1} \tag{2.40}$$

$$\epsilon = \frac{4}{3} C_{D2} \nu \frac{(u^*)^2}{(L^*)^2} = \frac{4}{3} C_{D2} \nu \frac{S_{\text{lam}}^2 (\text{Re}_{\text{turb}} + 1)}{(L^*)^2} = \frac{4}{3} C_{D2} \nu \frac{(\text{Re}_{\text{turb}} + 1) \left(\text{Da}_{\eta}\right)^2}{\tau_{\eta}} \tag{2.41}$$

$$C_{D2} = \frac{3}{4} \frac{1}{(\text{Re}_{\text{turb}} + 1)\, \text{Da}_{\eta}} \tag{2.42}$$

$$C_{\tau} \propto \frac{1}{\text{Da}_{\eta} \sqrt{\text{Re}_{\text{turb}} + 1}} \tag{2.43}$$

Similarly, Parente et al. (2015) derived an expression for C_{γ}. Based on the relationship between Re^*, C_{D2} and C_{D1} (equations 2.27, 2.44 and 2.40), the expression in equation 2.45 is derived. Using the definition of the chemical time scale with the laminar flame speed and the characteristic flame front length (equation 2.38) this equation can be further modified to equation 2.46. With the correlation of C_{γ}, C_{D2} and C_{D1} (equation 2.25), the final definition of C_{γ} dependent on Da_{η} and Re_{turb} is derived (equation 2.47).

$$S_{\text{lam}} \propto \sqrt{\frac{\nu}{\tau_c}} \tag{2.44}$$

$$\frac{C_{D2}}{C_{D1}} = \frac{3}{2} \frac{u^* L^*}{\nu} = \frac{3}{2} \frac{L^*}{S_{\text{lam}}} \frac{\sqrt{\text{Re}_{\text{turb}} + 1}}{\tau_{\text{che}}} \tag{2.45}$$

$$\frac{C_{D2}}{C_{D1}} = \frac{3}{2} \sqrt{\text{Re}_{\text{turb}} + 1} \tag{2.46}$$

$$C_{\gamma} \propto (\text{Da}_{\eta})^{\frac{1}{2}} \left(\text{Re}_{\text{turb}} + 1\right)^{\frac{1}{2}} \tag{2.47}$$

2.2.7 Extended EDC by Bao

According to Bao (2017), a drawback of Parente's model, see section 2.2.6, is that it only gives a qualitative expression for the constants C_{τ} and C_{γ}. Therefore, he suggests to derive quantitative expressions for C_{τ} and C_{γ}. The derivation of the equation for C_{γ} is quite similar to the one from Parente: the correlation between C_{D2} and C_{τ} (equation 2.26) is substituted into equation 2.42. A quantitative expression for C_{τ} is obtained depending on the Damköhler and the turbulent Reynolds number (equation 2.48).

In the derivation for C_{γ}, Bao (2017) proposes to drop the relation for flame speed (equation 2.44) and only use the relation of the small scales' length and the laminar flame speed (equation 2.38). The relation of C_{D2} and C_{D1} is reformulated (equation 2.49) based on the relation between the fine structures' speed, length and the

viscosity (equation 2.45). By using the definition of the Kolmogorov length scale (equation 2.19) and assuming that L^* is not only of the same order of magnitude, but equal to η, the Damköhler number is set equal to the fine structures length squared, divided by the chemical time scale and the viscosity (equation 2.50).

$$C_\tau = \frac{1}{2}\frac{1}{Da_\eta\sqrt{Re_{turb}+1}} \tag{2.48}$$

$$\frac{C_{D2}}{C_{D1}} = \frac{3}{2}\frac{\sqrt{Re_{turb}+1}}{\nu}\frac{(L^*)^2}{\tau_{che}} \tag{2.49}$$

$$\frac{(L^*)^2}{\nu\tau_{che}} = \frac{\left(\frac{\nu}{\epsilon}\right)^{\frac{1}{2}}}{\tau_{che}} = \frac{\tau_\eta}{\tau_{che}} = Da_\eta \tag{2.50}$$

$$C_\gamma = (Da_\eta)^{\frac{3}{4}}\sqrt{\frac{3}{2}\left(Re_{turb}+1\right)} \tag{2.51}$$

Using these assumptions, C_γ is derived (equation 2.51). According to Bao's definition C_γ is proportional to $(Da_\eta)^{\frac{3}{4}}$ instead of $(Da_\eta)^{\frac{1}{2}}$ as proposed by Parente et al. (2015). To avoid wrong results for slow reactions Bao (2017) suggests to force $C_{\gamma,max} = 2.13$, which corresponds to the original version of the EDC, section 2.2.3.

2.2.8 Fine structure modeling

Fast chemistry approach

One way to model the reactions in the fine structures is to assume infinitely fast chemistry. This means that educts immediately react, as soon as they are transfered to the fine structures. This approach is also called "mixed is burnt"-approach, (Stefanidis et al. 2006). As a consequence, the reaction is mixing controlled. Thus, the reaction rate R_{fu} can be modeled depending on the limiting substance in the reaction, equation 2.52 from (Magnussen 1981). Equation 2.53 defines the minimum concentration as the minimum of fuel and oxygen concentration normed with the stoichiometric factor. On the basis of this reaction rate definition, Magnussen (1981) also states that the temperature in the fine structures will exceed the temperature in the surrounding area due to the reaction enthalpy by ΔT (equation 2.54).

$$R_{fu} = \dot{m}\frac{\chi}{1-\gamma^*\chi}\bar{c}_{min} \tag{2.52}$$

$$\bar{c}_{min} = \min\left(\bar{c}_{fu}, \frac{\bar{c}_{O_2}}{a_{O_2}}\right) \tag{2.53}$$

$$\Delta T = \frac{\Delta h_R \bar{c}_{min}}{\bar{\rho} c_{pr}} \tag{2.54}$$

According to Magnussen (1981), the reacting fraction χ can be modeled by the fuel and product concentrations, $\bar{c}_{\mathrm{fu}}$ and $\bar{c}_{\mathrm{pr}}$, as well as the stoichiometric oxygen requirement, a_{O_2}, and γ_η (equation 2.55).

$$\chi = \frac{\frac{\bar{c}_{\mathrm{pr}}}{((1+r_{\mathrm{fu}})\gamma_{\mathrm{L}})}}{\frac{\bar{c}_{\mathrm{pr}}}{1+r_{\mathrm{fu}}} + \bar{c}_{\mathrm{fu}}} \tag{2.55}$$

In a later publication, (Gran and Magnussen 1996b), χ is calculated as a product of the probability of coexistence of reactants χ_1, the degree of heating χ_2 and the limitation due to the lack of reactants χ_3 (equations 2.56 and 2.57). For the expressions of χ_1, χ_2 and χ_3 the mass fractions are scaled by their stoichiometric coefficient (equation 2.58), (Gran and Magnussen 1996b).

$$\chi = \chi_1 \chi_2 \chi_3 \tag{2.56}$$

$$\begin{aligned} \chi_1 &= \frac{(\hat{Y}_{\mathrm{min}} + \hat{Y}_{\mathrm{pr}})^2}{(\hat{Y}_{\mathrm{fu}} + \hat{Y}_{\mathrm{pr}})(\hat{Y}_{\mathrm{ox}} + \hat{Y}_{\mathrm{pr}})} \\ \chi_2 &= \min\left[\frac{\hat{Y}_{\mathrm{pr}}}{\gamma(\hat{Y}_{\mathrm{pr}} + \hat{Y}_{\mathrm{min}})}, 1\right] \\ \chi_3 &= \min\left[\frac{\gamma(\hat{Y}_{\mathrm{pr}} + \hat{Y}_{\mathrm{min}})}{\hat{Y}_{\mathrm{min}}}, 1\right] \end{aligned} \tag{2.57}$$

$$\begin{aligned} \hat{Y}_{\mathrm{fu}} &= \frac{Y_{\mathrm{fu}}}{1} \\ \hat{Y}_{\mathrm{ox}} &= \frac{Y_{\mathrm{ox}}}{r_{\mathrm{fu}}} \\ \hat{Y}_{\mathrm{pr}} &= \frac{Y_{\mathrm{pr}}}{1 + r_{\mathrm{pr}}} \end{aligned} \tag{2.58}$$

It is not possible to use a complex reaction scheme with the "mixed-is-burnt" approach, but only a single global reaction or two consecutive reactions. This is one of the reasons, why this approach often leads to unreasonable results. Therefore, more detailed approaches have been developed and will also be used for the simulations carried out later.

Local extinction approach

The local extinction approach, presented by Byggstoyl and Magnussen (1983), is an extension of the fast chemistry approach, see above. The fast chemistry approach describes the real state quite well as long as the reaction time scale is significantly smaller than the mixing time scale. If the time scales are of the same order of magnitude, or the reaction time scale is even bigger, the reaction cannot proceed

to its full extend in the fine structures and even extinction can occur. This is not modeled by the fast chemistry approach. Therefore, an extinction time scale τ_{ext} is suggested by Byggstoyl and Magnussen (1983). The values for τ_{ext} are precalculated based on a chemical mechanism and the reaction is only assumed to happen if $\tau^* > \tau_{\text{ext}}$. If $\tau^* < \tau_{\text{ext}}$ the fast chemistry approach is used to model the reactions.

Detailed chemistry approach

The detailed chemistry approach treats the fine structures as continously stirred reactor (CSR) with constant pressure, (Gran and Magnussen 1996b). Usually, radiation heat losses are neglected, thus, the CSR is treated as an adiabatic reactor. This yields to the ODE-system, shown in equation 2.59. The first two equations depict the isobaric and adiabatic specification. The change in species concentrations depends on the change of the reaction rate $\frac{r_i^*}{\mathrm{d}t}$ and the transport due to mixing, expressed by τ^*, Y_i° and Y_i^*. When using the detailed chemistry approach, it is suggested by Gran and Magnussen (1996b) to set χ equal to unity (equation 2.60).

$$\begin{aligned} \frac{\mathrm{d}p}{\mathrm{d}t} &= 0 \\ \frac{\mathrm{d}h^*}{\mathrm{d}t} &= 0 \\ \frac{\mathrm{d}Y_i^*}{\mathrm{d}t} &= \frac{r_i^*}{\mathrm{d}t} + \frac{1}{\tau^*}(Y_i^\circ - Y_i^*) \end{aligned} \tag{2.59}$$

$$\chi = 1 \tag{2.60}$$

2.3 Operator Splitting

2.3.1 General remark

When the detailed chemistry approach for modeling the fine structures within the EDC is used, a highly non-linear (stiff) ODE-system has to be solved, see section 2.2.8. Since it is computationally expensive to solve this ODE-system, the idea is to split one ODE into two ODEs, solve them separately and obtain a solution for the original ODE from the two solutions of the simpler ODEs. This method is called operator splitting.

Another term for operator splitting methods is method of fractional steps. This displays that the subproblems are often solved on fractional, i.e. smaller time intervals, to obtain the solution after a certain time interval Δt.

The ODE in case of the EDC should be split into the mixing part and the chemical part, as shown in equations 2.61 and 2.62. Operator splitting is also necessary to

use ISAT, since tabulating for both ODE parameters distorts the ISAT table and makes the look-up inefficient, (Pope 1997) and (Rehm 2010).

$$\frac{\mathrm{d}Y^*_{i,\mathrm{che}}}{\mathrm{d}t} = \frac{r^*_i}{\mathrm{d}t} \tag{2.61}$$

$$\frac{\mathrm{d}Y^*_{i,\mathrm{mix}}}{\mathrm{d}t} = \frac{1}{\tau^*}(Y^\circ_i - Y^*_i) \tag{2.62}$$

In the following sections different operator splitting mechanisms are presented. To get the most suitable operator splitting method in context of the EDC, they will be tested later as described in section 3.1. To explain the different splitting methods in theory, a general notation for the problem is used:

$$\frac{\mathrm{d}U}{\mathrm{d}t} = AU(t) + BU(t) \text{ with t} \in [0, t_{\mathrm{end}}], U(0) = U_0 \tag{2.63}$$

2.3.2 First order methods

Additive splitting

Using additive splitting two sub problems (equations 2.64 and 2.65) are solved with the initial condition U_0 using a suitable numerical method. The solution $U(t + \Delta t)$ at the time $t + \Delta t$ is calculated via equation 2.66.

$$\frac{\mathrm{d}U^\alpha}{\mathrm{d}t} = AU(t), \text{ with } U^\alpha(t) = U_0 \tag{2.64}$$

$$\frac{\mathrm{d}U^\beta}{\mathrm{d}t} = BU(t), \text{ with } U^\beta(t) = U_0 \tag{2.65}$$

$$U(t + \Delta t) = U^\alpha(t + \Delta t) + U^\beta(t + \Delta t) - U_0 \tag{2.66}$$

Lie-Trotter splitting

The Lie-Trotter splitting scheme derived in (Trotter 1959) is also a first order splitting scheme. Similarly to the additive splitting scheme, the first subproblem (equation 2.67) is solved with the initial condition U_0. Then the second subproblem (equation 2.68) is solved using the solution from the first (equation 2.67) as initial condition. The solution from equation 2.68 is now taken as the final solution of the original ODE (equation 2.63) at $t + \Delta t$ (equation 2.69).

$$\frac{\mathrm{d}U^\alpha}{\mathrm{d}t} = AU(t), \text{ with } U^\alpha(t) = U_0 \tag{2.67}$$

$$\frac{\mathrm{d}U^\beta}{\mathrm{d}t} = BU(t), \text{ with } U^\beta(t) = U^\alpha(t + \Delta t) \tag{2.68}$$

$$U(t + \Delta t) = U^{\beta}(t + \Delta t) \tag{2.69}$$

2.3.3 Second order methods

Strang splitting

Using Strang splitting, (Strang 1963), subproblem A (equation 2.70) is solved for the time interval $\Delta t/2$ with the initial value U_0. Then subproblem B (equation 2.71) is solved for Δt using the result from subproblem A as initial condition. This solution from subproblem B is now used as the starting value for subproblem A again (equation 2.72). Subproblem A is solved on a time interval $\Delta t/2$. The obtained solution, $U(t + \Delta t)$, is now taken as the final solution of the original ODE (equation 2.73).

$$\frac{\mathrm{d}U^{\alpha}}{\mathrm{d}t} = AU(t), \text{ with } U^{\alpha}(t) = U_0 \tag{2.70}$$

$$\frac{\mathrm{d}U^{\beta}}{\mathrm{d}t} = BU(t), \text{ with } U^{\beta}(t) = U^{\alpha}\left(t + \frac{\Delta t}{2}\right) \tag{2.71}$$

$$\frac{\mathrm{d}U^{\alpha}}{\mathrm{d}t} = AU(t), \text{ with } U^{\alpha}\left(t + \frac{\Delta t}{2}\right) = U^{\beta}(t + \Delta t) \tag{2.72}$$

$$U(t + \Delta t) = U^{\alpha}(t + \Delta t) \tag{2.73}$$

Staggered splitting

When the staggered splitting scheme, (Ren and Pope 2008), is used, the equations 2.70 and 2.71 are solved as shown in Figure 2.3. The first problem is solved for Δt and the solution is used as initial value to solve the next equation from n+1/2 to n+3/2. The solution of the system is obtained as arithmetic mean of the two solutions.

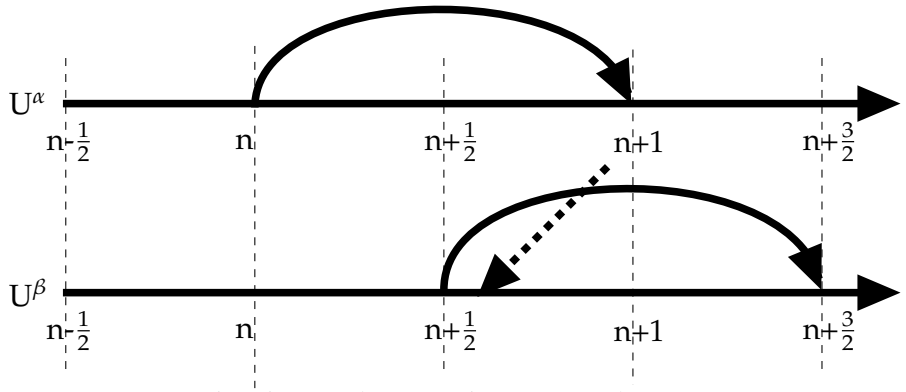

Figure 2.3: Staggered Splitting (Ren and Pope 2008)

The initial condition for the first step of calculating U^{β} is taken as the solution of U^{α} solved from 0 to $\frac{\Delta t}{2}$.

Symmetrically weighted sequential splitting

The symmetrically weighted sequential splitting (swss) scheme, first introduced by Strang (1968), builds on the Strang splitting scheme. First the Strang scheme is applied normally. Then it is applied again in opposed order, i.e. subproblem B (equation 2.71), is solved first for $\Delta t/2$, then subproblem A for Δt (equation 2.70) and again subproblem B for $\Delta t/2$ using initial conditions as explained for Strang splitting. Now we have two solutions of the ODE, U_1 and U_2. The final solution is calculated as arithmetic mean of those two solutions (equation 2.74).

$$U(t + \Delta t) = \frac{U_1(t + \Delta t) - U_2(t + \Delta t)}{2} \tag{2.74}$$

2.3.4 Iterative splitting

The iterative splitting scheme proposed by Geiser and Gedicke (2008) has higher order convergence for many problems like the one shown in equation 2.63. The application of the iterative splitting scheme is done as described in equations 2.75 and 2.76, where I denotes the function at the current time and I+1 and I-1 the solutions at t+/-Δt. When solving the subproblems, the other part is not totally neglected here, but taken into account by using the value of the function from the old time level for its calculation.

$$\frac{\mathrm{d}U_I(t)}{\mathrm{d}t} = AU_I(t) + BU_{I-1}(t) \tag{2.75}$$

$$\frac{\mathrm{d}U_{I+1}(t)}{\mathrm{d}t} = AU_I(t) + BU_{I+1}(t) \tag{2.76}$$

2.3.5 Higher order methods

Higher order methods were not considered in context of the EDC, since the gained accuracy is mostly not worth the increased computational and implementation effort, (MacNamara and Strang 2009). Moreover, second order methods are said to be the best way to achieve sufficient accuracy with acceptable complexity. Furthermore, Duarte and Massot (2015) state, that higher order methods are not suitable for stiff problems, and the problem at hand is considered a highly stiff ODE-system.

2.4 Chemical Time Scale Definitions

2.4.1 General remark

For the extended EDC models, mentioned in the sections 2.2.6 and 2.2.7, a definition of the chemical time scale of the reacting system is needed to calculate the Kolmogorov Damköhler number (equation 2.36). It is possible to define a chemical time scale for each reaction, but many of them are irrelevant for the overall evolution of the system. As the Kolmogorov Damköhler number should characterize the system, one governing chemical time scale for the ODE-system of the reactions is needed (equation 2.77). A literature survey was conducted to find methods and time scale definitions to obtain one relevant chemical time scale. Section 2.4.3 to section 2.4.13 give an overview of the definitions found in literature. A general explanation of chemical time scales is given in section 2.4.2.

$$\frac{\mathrm{d}\mathbf{Y}}{\mathrm{d}t} = \dot{\omega}(Y_1, Y_2, ...Y_{n_s}) \tag{2.77}$$

2.4.2 Chemical time scales of a system

The eigenvalues of the Jacobian matrix of the ODE-system (equation 2.77), are said to be the chemical time scales of the chemical system. The Jacobian of $\dot{\omega}$ at time t_0 is defined by:

$$\mathcal{J}_{ij} = \frac{\partial \dot{\omega}_i \left(Y^0\right)}{\partial Y_j}(Y^0) \tag{2.78}$$

To obtain the eigenvalues of a system, the Jacobian matrix has to be decomposed, shown in equation 2.79. There, $\mathbf{\Lambda}$ is a diagonal matrix containing the eigenvalues λ_i of the Jacobian, which are either complex or real, and $\mathbf{V}$ is the matrix formed by the corresponding eigenvectors.

$$\mathcal{J} = \mathbf{V} * \mathbf{\Lambda} * \mathbf{V}^{-1} \tag{2.79}$$

Subsequently, the connexion between the Jacobian and the solution of the ODE is shown. This will be needed for some of the following chemical time scale definitions. The Taylor series expansion of $\dot{\omega}$ with respect to Y^0 and Y^e is given in equations 2.80 and 2.81. If all terms with order three or higher are dropped and $E = (Y^e - Y^0)$, $E(t)$ is the solution of the linear ordinary differential equation, (2.82).

$$\dot{\omega}(Y^\mathrm{e}) = \dot{\omega}(Y^0) + \frac{\partial \dot{\omega}_i}{\partial Y_j}(Y^0) * (Y^\mathrm{e} - Y^0) + \mathcal{O}((Y^\mathrm{e} - Y^0)^2) \tag{2.80}$$

$$\frac{\mathrm{d}}{\mathrm{d}t}(Y^{\mathrm{e}} - Y^0) = \frac{\partial \dot{\omega}_i}{\partial Y_j}(Y^{\mathrm{e}} - Y^0) + \mathcal{O}((Y^{\mathrm{e}} - Y^0)^2) \tag{2.81}$$

$$\frac{\mathrm{d}}{\mathrm{d}t}E(t) = E(t) \tag{2.82}$$

2.4.3 System progress time scale

The system progress time scale (SPTS) was first introduced by Prüfert et al. (2014). The system's time scale is given in equation 2.83 depending on the Jacobian matrix and $E_0(t)$. $E_0(t)$ is chosen to be $\frac{\dot{\omega}(t_0)}{\|\dot{\omega}(t_0)\|}$, where $\|\cdot\|$ denotes the matrix norm. The time scale given here, can be interpreted as the time the system needs to react on perturbations in the direction of linearized progress, (Prüfert et al. 2014). $\tau_{\mathrm{che}}(t)$ approximates $\|\mathcal{J}\|^{-1}$ and is therefore believed to represent the time evolution of the whole system, (Prüfert et al. 2014).

$$\tau_{\mathrm{che}}(t) = (\|\mathcal{J}(t)E_0(t)\|)^{-1} \tag{2.83}$$

2.4.4 Progress variable time scale

The progress variable time scale (PVTS), also proposed by Prüfert et al. (2014), is an approximation to the SPTS with the difference that the PVTS uses the directional derivative in direction of the progress variable instead of $\dot{\omega}$. The definition is given by equation 2.84, and equations 2.85 and 2.86, where J describes the indices of the main, respectively relevant, species, which have to be predefined. In this definition, as we see in equations 2.84 to 2.86, only the main species J are relevant. The problem with this time scale definition is the choice of the most relevant species to obtain a reasonable chemical time scale.

$$\tau_{\mathrm{che}}(t) = \frac{\|\mathbf{v}\|}{\|\mathcal{J}_v(y)\|} \tag{2.84}$$

$$v_i = \begin{cases} y_i(t + \delta t), i \in \mathrm{J} \\ 0, \text{otherwise} \end{cases} \quad \text{for all } i = 1, 2, ...n_s \tag{2.85}$$

$$\mathcal{J}_v(y) = \lim_{s \to 0} \frac{\dot{\omega}_i(y + sv) - \dot{\omega}_i(y)}{s} \tag{2.86}$$

2.4.5 Inverse Jacobian time scale

The inverse jacobian time scale (IJTS) definition is also presented in the paper from Prüfert et al. (2014), but it is a combination of the methods presented by Løvås et al. (2002) and Caudal et al. (2013) with some minor modifications. The eigenvalues

of the Jacobian are approximated by the inverse of the diagonal elements of the Jacobian (equation 2.87). In the IJTS method a relevant subset of eigenvalues is defined by the condition in equation 2.88, where e_i are the canonical basis vectors and j are the species in the reactions n_s. The smallest of those time scales is used as the characteristic chemical time scale.

$$\tau_{\text{che}}(t) = \min \left| \frac{\partial \dot{\omega}_i}{\partial Y_i} \right|^{-1} \tag{2.87}$$

$$\left\| \left(\sum_{i \in \mathrm{J}} \dot{\omega}_i e_i \right) - \dot{\omega} \right\| < \varepsilon \tag{2.88}$$

2.4.6 Inverse Jacobian time scale - simple

To avoid the calculation of the Jacobian, a modified time scale based on the IJTS is suggested. The reduction of the system is carried out in the same way as for the IJTS (equation 2.88) but the approximation of the chemical time scale is different. τ_{che} is approximated as shown in equation 2.89. In the same manner as for IJTS the smallest time scale of the remaining is chosen as the governing chemical time scale.

$$\tau_{\text{che}}(t) = \min_{i \in J} \frac{1}{|\dot{\omega} e_i|} \tag{2.89}$$

2.4.7 Characteristic time scale identification

The characteristics time scale identification (CTS-ID), also called eigenvalue time scale (EVTS), presented by Caudal et al. (2013) is based on the Jacobian analysis, section 2.4.2, and gives a method to evaluate the chemical time scales according to their contribution to the overall change of the system. The eigenvalues and eigenvectors have to be transformed to a different basis first. This gives a matrix $\tilde{\mathbf{\Lambda}}$ (equation 2.90) where L_P corresponds to the real eigenvalues in $\mathbf{\Lambda}$ in descending order and $\mathbf{L}'_j = \begin{pmatrix} \Re(\lambda_j) & \Im(\lambda_j) \\ -\Im(\lambda_j) & \Re(\lambda_j) \end{pmatrix}$ for $j = P+1, P+3, ...n_s - 1$. The corresponding eigenvectors in the new basis are obtained through equation 2.91.

$$\tilde{\mathbf{\Lambda}} = \begin{pmatrix} L_P & & & \\ & L'_{P+1} & & \\ & & \ddots & \\ & & & L'_{n_s-1} \end{pmatrix} \tag{2.90}$$

$$\begin{aligned} \tilde{\mathbf{V}}_j &= \mathbf{V}_j \text{ for } j = 1, ...P \\ \left.\begin{aligned} \tilde{\mathbf{V}}_j &= \Re(\mathbf{V}_j) \\ \tilde{\mathbf{V}}_{j+1} &= \Im(\mathbf{V}_j) \end{aligned}\right\} &\text{ for } j = P+1, P+3, ...P+l-1 \end{aligned} \tag{2.91}$$

$$\hat{\gamma}_j = \frac{\left\|\tilde{\omega}_j \tilde{\mathbf{V}}_j\right\|}{\max_{k\in[1,n_s]} \left\|\tilde{\omega}_k \tilde{\mathbf{V}}_k\right\|} \tag{2.92}$$

$$\tilde{\omega} = \tilde{\mathbf{\Lambda}}\dot{\omega} \tag{2.93}$$

$$\tau(t) = min_{j\in \mathrm{J}} \frac{1}{|\lambda_j|} \tag{2.94}$$

The weight factor $\hat{\gamma}$ is calculated via equation 2.92, where $\tilde{\omega}_j$ is the j^{th} component of $\dot{\omega}$ in the new basis (equation 2.93). Thereby, a relevant subspace, denoted by the subscript J, is obtained, for all $\hat{\gamma}_j > \varepsilon$. Only considering this relevant subspace, the characteristic time scale is taken to be the smallest eigenvalue of the subspace (equation 2.94), (Prüfert et al. 2014).

2.4.8 Main direction identification

Li et al. (2017a) proposed a modification of the CTS-ID, called main direction identification (MDID), where the ranking of the eigenvalues is given by $\hat{\gamma}_j$ (equation 2.92), but then the relevance of the corresponding species is checked in addition. Therefore, a weighting matrix $H_{i,j}$ is calculated according to equation 2.96, which represents the contribution of species i along direction j and then the corresponding mole fractions $X_{i,j}$ are sorted by decreasing $\hat{\gamma}_j$ (a indicates the sorted values). Then they are sorted by increasing $H_{i,a}$ order. To check, if the most relevant species, given through the highest $\hat{\gamma}_j$, are represented sufficiently in the system state, the mole fractions $X_{1,a}$ and $X_{2,a}$ are checked against a lower mole fraction limit, X_ε. This mole fraction is chosen as 0.005 in (Li et al. 2017a), but this is not applicable, if the checked species is oxygen. The mole fractions are checked in descending $\hat{\gamma}_j$ order until condition 2.97 is met.

$$S_j = \sum_{j=1}^{n_s} \tilde{\omega}\tilde{\mathbf{V}}_j \tag{2.95}$$

$$H_{i,j} = \mathrm{sign}(S_j) \frac{\tilde{V}_{i,j}}{\sum_{k=1}^{n_s} |\tilde{V}_{k,j}|} \tag{2.96}$$

$$X_{1,a} > X_\varepsilon \text{ and } X_{2,a} > X_\varepsilon \tag{2.97}$$

2.4.9 Level of importance

The level of importance (LOI) method was introduced by Løvås et al. (2002) to reduce complex mechanisms to skeletal ones. This means a relevant subspace of

equations is defined by the LOI method. For the purpose of getting one relevant chemical time scale, the chemical time scale is determined by the highest LOI value.

The definition of the LOI parameter is given in equation 2.98, where τ_i is the chemical time scale of each reaction approximated by the diagonal elements of the Jacobian matrix (equation 2.99) and ${S^c}_{i,j}$ the sensitivity parameter, defined in equation 2.100. The other variables are: r_d, the reaction rate and $v_{j,\mathrm{d}}$, the stoichiometric coefficient, where prime denotes the reactants.

$$\mathrm{LOI}_i^j = {S^c}_{i,j}\tau_i \tag{2.98}$$

$$\tau_i = -\frac{1}{\mathcal{J}_{i,i}} \tag{2.99}$$

$${S^c}_{i,j} \approx \left| \sum_{k=1}^{n_s} \frac{\mathrm{d}c_i}{\mathrm{d}r_\mathrm{d}} \frac{v'_{j,\mathrm{d}} r_\mathrm{d}}{c_j} \right| \tag{2.100}$$

The term $\frac{v'_{j,\mathrm{d}} r_\mathrm{d}}{c_j}$ is an approximation of $\frac{\mathrm{d}r_\mathrm{d}}{\mathrm{d}c_j}$, given in (Løvås et al. 2002). No approximation of $\frac{\mathrm{d}c_i}{\mathrm{d}r_\mathrm{d}}$ in equation 2.100 was given by Løvås et al. (2002) and as the direct calculation is not straightforward and numerically expensive, it was decided to use a similar approximation as for $\frac{\mathrm{d}r_\mathrm{d}}{\mathrm{d}c_j}$. With that approximation the final expression for ${S^c}_{i,j}$ is obtained: equation 2.101.

$${S^c}_{i,j} \approx \left| \sum_{k=1}^{n_s} \frac{c_i}{v'_{i,\mathrm{d}} r_\mathrm{d}} \frac{v'_{j,\mathrm{d}} r_\mathrm{d}}{c_j} \right| \tag{2.101}$$

2.4.10 Ren's time scale

Ren and Goldin (2011) suggested to modify the mixing time scale τ^* in the EDC to a sum of a flow and a chemical time scale (equation 2.102). Therefore, they defined τ_che as a ratio of the species mass fractions and consumption rates (equation 2.103). Unfortunately, the constant in this definition, c_che, was not assigned a value in (Ren and Goldin 2011), nevertheless this method will be tested. In (Ren and Goldin 2011) it is suggested to use a user specified set of species for the evaluation of equation 2.103. Here it will be evaluated for all species whose net production rate r_fu is smaller than 0, meaning all consumed species are considered.

$$\tau^* = \tau_\mathrm{flow} + \tau_\mathrm{che} \tag{2.102}$$

$$\tau_\mathrm{che} = \mathrm{c}_\mathrm{che} \min_\mathrm{fu} \left(\frac{Y_\mathrm{fu}}{r_\mathrm{fu}} \right) \tag{2.103}$$

2.4.11 Ren's product time scale

Alternatively to using all consumed species for evaluation of the chemical time scale as in 2.4.10, it will be also tested to use all produced species. This gives the definition of τ_{che} shown in equation 2.104.

$$\tau_{\mathrm{che}} = \mathrm{c}_{\mathrm{che}} \min_{\mathrm{pr}} \left(\frac{Y_{\mathrm{pr}}}{r_{\mathrm{pr}}} \right) \tag{2.104}$$

2.4.12 Principal variable analysis

For the principal variable analysis (PVA), described by Isaac et al. (2013) a number of observations of the variables are needed, which is not available right now. Furthermore, the computational expense was considered too high to be useful for the determination of time scales during computational fluid dynamics (CFD) simulation. Therefore, the PVA is not applicable for this purpose and will not be used further in this work.

2.4.13 Computational singular perturbation

Lam and Goussis (1991) introduced computational singular perturbation (CSP) to define a slow and a fast reacting subspace. As for the EDC one relevant time scale is needed, the division into two-subspaces does not fulfill the need of obtaining one characteristic chemical time scale for calculating the Damköhler number. Therefore, this method was not used.

3 Methods

3.1 Operator Splitting

3.1.1 Implementation in Python

To test the different operator splitting methods presented in section 2.3 for the EDC, the ODE-system for the CSR (equation 2.59) was solved via direct integration and with the different operator splitting methods. Therefore, the ODE was split into a chemistry term and a mixing term (equations 3.1 and 3.2).

The tests were carried out using the programming language Python, (Rossum 1995). One cell with a CSR representing the fine structures in this cell was implemented using $\dot{m}^*$ and γ^* as input parameters (see section 3.1.2 for the parameters). The DRM22 reaction mechanism, which is a reduced mechanism of the GRI-Mech1.2, (Kazakov and Frenklach 2017), was used. The chemistry was plugged in using Cantera, (Goodwin and Speth 2017), a toolkit for chemical kinetics, thermodynamics and transport processes. To solve the ODE, either via direct integration or with operator splitting, the vode-solver from the SciPy package was used for the integration, (Jones et al. 2001).

$$\frac{\mathrm{d}Y^*_{i,\mathrm{che}}}{\mathrm{d}t} = \frac{r^*_i}{\mathrm{d}t} \tag{3.1}$$

$$\frac{\mathrm{d}Y^*_{i,\mathrm{mix}}}{\mathrm{d}t} = \frac{1}{\tau^*}(Y^\circ_i - Y^*_i) \tag{3.2}$$

3.1.2 Test cases

The values for the input parameters, $\dot{m}^*$ and γ^*, were chosen from a previously modeled Sandia Flame D, (Barlow and Frank 1998), see section 3.3 for more details on Sandia Flame D. The temperature profile of the simulated flame is shown in Figure 3.1. From x=0 to x=0.1 the methane and pilot inlet can be seen. The burner tip is located at approximately 0.1m. The location of the points, where the values were taken for the test cases, are shown schematically in Figure 3.1. The operator splitting methods were tested for seven different cases (Table 3.1). A constant time step of 10^{-5}s was chosen for the test cases. To ensure proper ignition it had to be reduced to 10^{-6}s for Case 6. This might be explained by the high $\dot{m}^*$ value in this case, which gives a low τ^*. The initial conditions for temperature and composition

were chosen to be the same for every case and were chosen quite arbitrarily as this was not the point of investigation.

Table 3.1: Parameters for operator splitting test cases

	Case 1	Case 2	Case 3	Case 4	Case 5	Case 6	Case 7
$\dot{m}^*$	363.02	17568	75.312	20.26	9657	150290	21756
γ^*	0.0048	0.0215	0.0376	0.1076	0.1078	0.1670	0.5

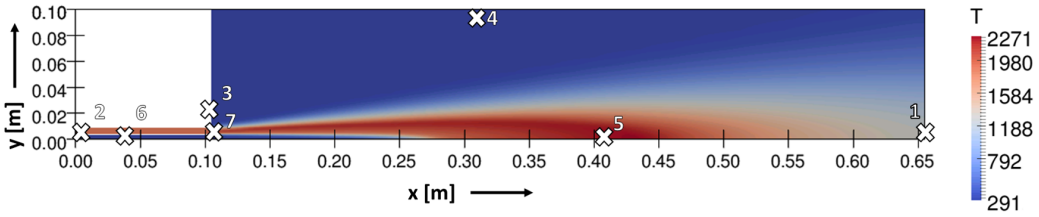

Figure 3.1: Points chosen for the operator splitting test cases

Although the order of accuracy for the operator splitting methods has been proven and is given in literature, it is tested by varying the time step size for Case 4 and comparing the error of the different results. The error is approximated by equation 3.3, as in (Ren and Pope 2008). Furthermore, these test cases were also used to show the dependency of the central processing unit (CPU) time on the time step size.

$$\text{Error}_{\max} = \frac{1}{\max\left(\left|U^{\text{DI}}(t)\right|\right)} \max\left(\left|U^{\text{DI}}(t) - U^{\text{OS}}(t+\Delta t)\right|\right) \tag{3.3}$$

3.1.3 Analytical solution - mixing part

Operator splitting divides the ODE problem into two simpler sub problems. In case of the EDC model these sub problems are a chemical part and a mixing part (equations 3.1 and 3.2). These ODEs are already easier to solve using numerical methods, as is done in the test cases presented in section 3.1.2, but the mixing part can also be solved analytically. This can lead to further speed up in the calculations. The ODE (equation 3.2) represents an inhomogeneous, first order differential equation with constant coefficients.

Using the relation between the fine structures ($*$), the surroundings ($^\circ$) and the mean cell values ($\bar{}$) (equation 2.31), the ODE is transformed into equation 3.4. The initial condition for t=0 at the new time level (n+1) is given by the fine structure mass fraction, i.e. the solution of the old time level (n) (equation 3.5).

Using the given initial condition, the solution of the ODE is obtained and given in equation 3.6. The analytical solution is a function of the species concentrations, the mixing time scale and the mass fraction of the fine structure.

$$\frac{\mathrm{d}Y_i^*}{\mathrm{d}t} = \frac{1}{\tau^* \left(1-\gamma^*\right)} \bar{Y}_i - \frac{1}{\tau^* \left(1-\gamma^*\right)} Y_i^* \tag{3.4}$$

$$Y_{i,n+1}^* = Y_{i,n}^* \tag{3.5}$$

$$Y_{i,n+1}^* = \left(Y_{i,n}^* - \bar{Y}_{i,n}\right) \exp\left(\frac{1}{\tau^* \left(1-\gamma^*\right)} t\right) + \bar{Y}_{i,n} \tag{3.6}$$

The presented analytical solution is faster to calculate than the numerical solution and will be used within the simulation in OpenFOAM to further improve the numerical efficiency.

3.2 Chemical Time Scale Definitions

3.2.1 Implementation in Python

The testing of the chemical time scale definitions was performed for one CSR in a computational cell. The same setup as for the operator splitting was used, see section 3.1.

For many of the chemical time scale definitions the computation of the Jacobian $\mathcal{J}$ is needed and for some even the decomposition of the Jacobian to the eigenvectors and eigenvalues is necessary. The Jacobian is computed using the numdifftools package provided by Brodtkorb (2017), which is based on the adaptive differentiation toolbox written by D'Errico (2006). The decomposition was computed using numpy which comes with the before mentioned SciPy package, (Van der Walt et al. 2011). The implemented methods in numpy are based on the LAPACK routines, (Anderson et al. 1999).

3.2.2 Test cases

Global reaction

To compare the results of the chemical time scale definitions with other results, it was chosen to calculate the time scale for a simple global reaction in the beginning. This test case was taken from (Prüfert et al. 2014). The test case is a one step hydrogen combustion process, see reaction equation 3.7. The species and energy source terms are based on the equations presented by Buffoni and Willcox (2010) (equations 3.8 and 3.9). It has to be stated here, that the reaction with the chosen parameters is a test case with no physical meaning, as the parameters are not chosen to fit the physical process of hydrogen oxidation. However, the chemical

time scale calculation and the analytical eigenvalue solution can be compared using this simple reaction. The used parameters are presented in Table 3.2.

$$2H_2 + O_2 \rightarrow 2H_2O \tag{3.7}$$

$$s_i = -v_i \left(\frac{W_i}{\rho}\right) \left(\frac{\rho Y_{\mathrm{fu}}}{W_{\mathrm{fu}}}\right)^{v_{\mathrm{fu}}} \left(\frac{\rho Y_{\mathrm{ox}}}{W_{\mathrm{ox}}}\right)^{v_{\mathrm{ox}}} A_{\mathrm{Arr}} \exp\left(-\frac{E_{\mathrm{Arr}}}{\mathrm{R}_{\mathrm{gas}} T}\right) \text{ with } i = \mathrm{ox}, \mathrm{fu}, \mathrm{pr} \tag{3.8}$$

$$s_T = s_{\mathrm{pr}} Q \tag{3.9}$$

Table 3.2: Parameter for the global reaction

W_{H_2}	W_{O_2}	W_{H_2O}	Q	$\mathrm{R}_{\mathrm{gas}}$	ρ [g/cm^3]
2.016	31.9	18	9800	8.394	$1.39{\cdot}10^{-3}$

Y_{H_2}	Y_{O_2}	Y_{H_2O}	T	A_{Arr}	E_{Arr}
8/9	1/9	0	300	$5.5{\cdot}10^{11}$	$4.5{\cdot}10^{3}$

Homogeneous reactors - from (Prüfert et al. 2014)

Further test cases for the chemical time scale definitions were also chosen from (Prüfert et al. 2014). From a flame simulation of a partial oxidation (POX) flame, three different positions, in three distinct zones of the flame, were taken as initial conditions for the calculation of reactions in a homogenous reactor (HR) (Figure 3.2). Furthermore, the HRS were chosen isothermal and isobaric, as in (Prüfert et al. 2014). The GRI-Mech3.0, (Smith et al. 2017), was used as reaction mechanism within Cantera, (Goodwin and Speth 2017), for the calculations. For the reaction, only the chemical part (equation 3.1), was taken into account and the mixing term (equation 3.2) was neglected. This wad done, since the purpose was to calculate chemical time scales regardless of the EDC at this point.

Test cases from flame simulation

Similarly to the test cases in 3.2.2, test cases were chosen from an existing Flame D simulation, a piloted methane-air flame, where a global mechanism was used. Instead of choosing quite different positions in the flame as in section 3.1.2, the purpose was to calculate radial profiles of the turbulent Damköhler number $\mathrm{Da}_{\mathrm{turb}}$ (equation 3.10) and the chemical time scale. Two locations for the radial profile were chosen, 0.35 m and 0.20 m upstream the burner tip. Five and six points in the hot reacting zone were defined. The points are shown schematically in Figure 3.3.

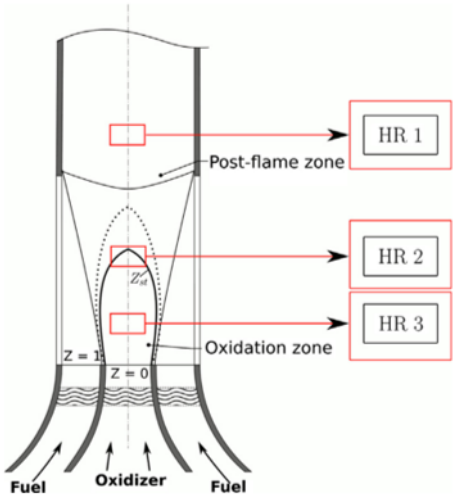

Figure 3.2: Positions of the HR in (Prüfert et al. 2014) p.420

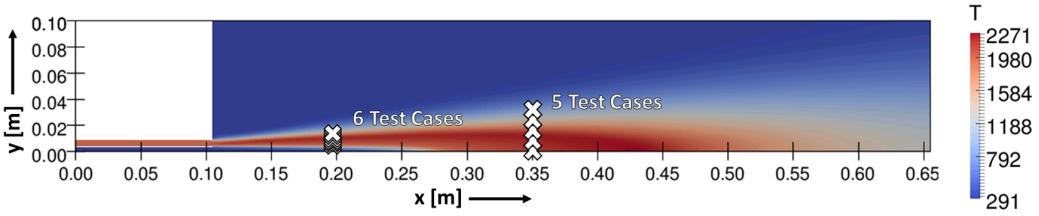

Figure 3.3: Points chosen for the test cases for chemical time scale calculations

As in section 3.2.2, the concentrations from the simulation were chosen as initial conditions for the CSR. The chemical time scale was calculated, neglecting the mixing term of equation 2.59, therefore, just considering equation 3.1. The CSR was considered adiabatic and isobaric, not isothermal this time, as it will be done in the EDC with the detailed chemistry approach. The initial conditions for the test cases are shown in the Table 3.3 and Table 3.4. The parameters to calculate the mixing time scale, τ_{mix} for Da_{turb} (equation 3.11) were also obtained from the flame simulation and are given in Table 3.5.

$$Da_{turb} = \frac{\tau_{mix}}{\tau_{che}} \tag{3.10}$$

$$\tau_{mix} = \frac{k}{\epsilon} \tag{3.11}$$

Table 3.3: Initial conditions for test cases 0.35m upstream the burner tip, species concentrations in mass fractions

y [m]	CH_4	N_2	CO_2	H_2O	O_2	T [K]
0.0028	0.0242	0.7093	0.1463	0.1201	$1.267 \cdot 10^{-4}$	2094
0	0.0256	0.7082	0.1461	0.1199	0.7631	2086
0.0111	$6.8635 \cdot 10^{-3}$	0.7232	0.1452	0.1192	$5.529 \cdot 10^{-3}$	2157
0.0187	0.0203	0.7402	0.1039	0.0853	0.0704	1742
0.0324	0.0263	0.7604	0.0335	0.0275	0.1786	836

Table 3.4: Initial conditions for test cases 0.20m upstream the burner tip, species concentrations in mass fractions

y [m]	CH_4	N_2	CO_2	H_2O	O_2	T [K]
0.00273	0.1190	0.6532	0.0818	0.0671	0.0789	1277
0.0036	0.0970	0.6582	0.1248	0.1024	0.0175	1717
0.0078	0.0411	0.6971	0.1434	0.1181	$2.474 \cdot 10^{-4}$	2031
0.0091	0.0298	0.7057	0.1447	0.1192	$6.955 \cdot 10^{-4}$	2083
0.0132	$77685 \cdot 10^{-4}$	0.7376	0.1123	0.0924	0.0569	1860
0.0144	$1.9742 \cdot 10^{-4}$	0.7443	0.0903	0.0744	9.074	1609

3.3 Simulation of Sandia Flame D

3.3.1 Grid convergence study

To examine whether the grid generated is refined enough, a grid convergence study has to be carried out. Roache (1994) proposes the grid convergence index (GCI) as a uniform measurement for grid convergence. The GCI can also be interpreted as an estimation of the calculation error due to the used grid. The formulae for the GCI for the fine and the coarse grid are given in equations 3.12 and 3.13. The GCI is calculated depending on the order of accuracy (N) of the used methods, the grid refinement ratio Ψ (equation 3.14) and the difference between the solutions ζ (equation 3.15).

$$\mathrm{GCI}_{\text{fine grid}} = K\,|\zeta|\,\frac{1}{\Psi^N - 1} \tag{3.12}$$

$$\mathrm{GCI}_{\text{coarse grid}} = \mathrm{GCI}_{\text{fine grid}} + K\,|\zeta| = K\,|\zeta|\,\frac{\Psi^N}{\Psi^N - 1} \tag{3.13}$$

K is a "safety" factor in the above given equations. Roache (1994) originally proposed $K = 3$, but also stated that this was quite conservative. In a later publication,

Table 3.5: Parameters for τ_{mix}

0.35 m upstream burner tip			0.20 m upstream burner tip		
y [m]	k	ϵ	y [m]	k	ϵ
0.0028	56.39	18212	0.0027	13.99	12797
0	55.65	17839	0.0036	28.23	28166
0.0111	58.23	18969	0.0078	83.20	83237
0.0187	41.71	11443	0.0091	81.16	76861
0.0324	92.89	1289	0.0132	44.38	29822
			0.0144	33.06	19432

(Celik et al. 2008), K was set to 1.25. As the later publication is more up to date and also Roache contributed there, it was chosen to use the value of 1.25 instead of 3 in equation 3.12 for further calculations.

$$\Psi = \frac{m_2}{m_1} \tag{3.14}$$

$$\zeta = \frac{\theta_2 - \theta_1}{\theta_2} \tag{3.15}$$

The grid refinement ratio is defined as the fraction of the coarse grid spacing m_2, and the fine grid spacing, m_1. Since the order of the numerical methods might not be known, Celik et al. (2008) proposes an estimation (equations 3.16 and 3.17). This estimation depends on the refinement ratios and the differences between the solutions. If the refinement ratio Ψ is constant, the calculation simplifies because $f(N) = 0$. The grid refinement factor Ψ might be arbitrarily chosen, but Roache (1994) recommends to use $\Psi \geq 1.1$ and Celik et al. (2008) even states that $\Psi \geq 1.3$. To ensure applicability of the GCI 1.3 will be chosen in this study.

$$N = \frac{1}{\ln(\Psi_{21})} \left| \ln \left| \frac{\zeta_{32}}{\zeta_{21}} \right| + f(N) \right| \tag{3.16}$$

$$f(N) = \ln \left(\frac{\Psi_{21}^N - \text{sign}\left(\frac{\zeta_{32}}{\zeta_{21}}\right)}{\Psi_{32}^N - \text{sign}\left(\frac{\zeta_{32}}{\zeta_{21}}\right)} \right) \tag{3.17}$$

The asymptotic range of the grid convergence is reached, if equation 3.18 is fulfilled. There 1 denotes the finest grid and 3 the coarsest. The study should be carried out for at least three grids, to get an indication if the asymptotic range is reached. Here it will be done for four grids, with different refinement ratios: from the coarsest to the succeeding they are 1.5, 1.34 and 2. A part of each grid is shown in Figure 3.4.

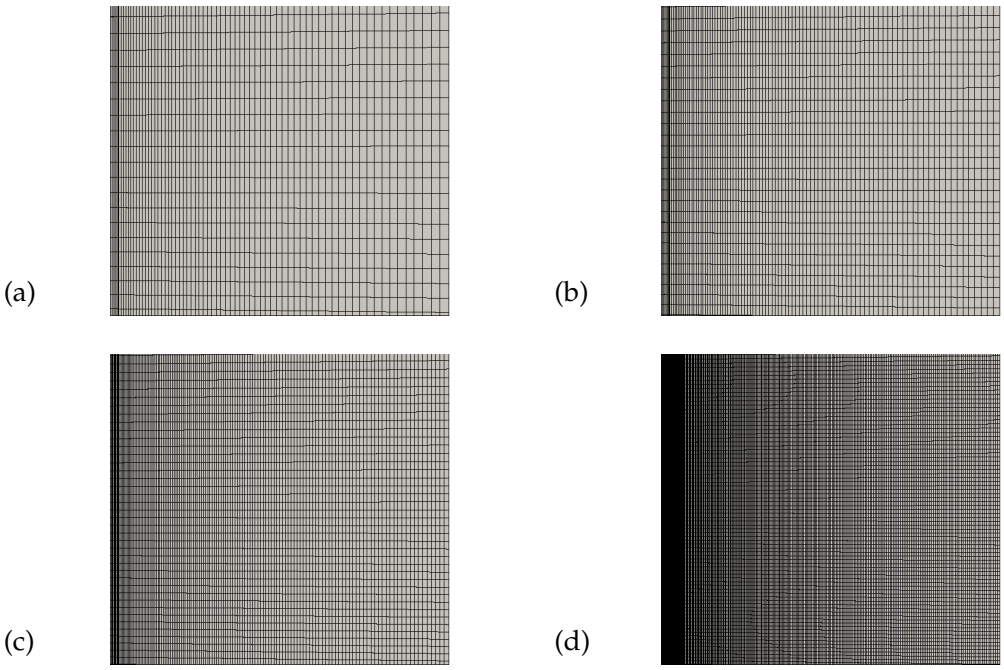

Figure 3.4: Grids used to calculate the GCI (a) 4329 cells (b) 9628 cells (c) 17316 cells, (d) 69264 cells

$$\mathrm{GCI}_{23} = \Psi^N \mathrm{GCI}_{13} \tag{3.18}$$

3.3.2 OpenFOAM simulation

Sandia Flame D was chosen to validate the implemented EDC with detailed chemical kinetics and operator splitting in OpenFOAM. The used algorithm is shown in Figure 3.5, which basically represents the pressure implicit with splitting of operator (PISO) loop, (Issa 1986). The PISO algorithm is based on the semi implicit method for pressure-linked equations (SIMPLE) algorithm, (Patankar and Spalding 1972), and modified it to be applicable for transient flows. When the continuity equation is solved, the EDC is used to take care of the changes in mass fraction, density, temperature, etc. due to chemical reactions. The calculation procedure of the EDC is shown in Figure 3.6, where the flow properties, such as the turbulent kinetic energy, the dissipation rate, the kinematic viscosity and the average mass fraction in the observed cell, are used as input variables. After solving the equations, the species reaction rates R_i^* are updated.

The used flame for validation, Flame D, (Masri et al. 1996) and (Barlow and Frank 1998), is a piloted methane/air flame with a jet diameter of 7.2mm and a pilot diameter of 18.2mm. The composition is 25% methane and 75% air by volume.

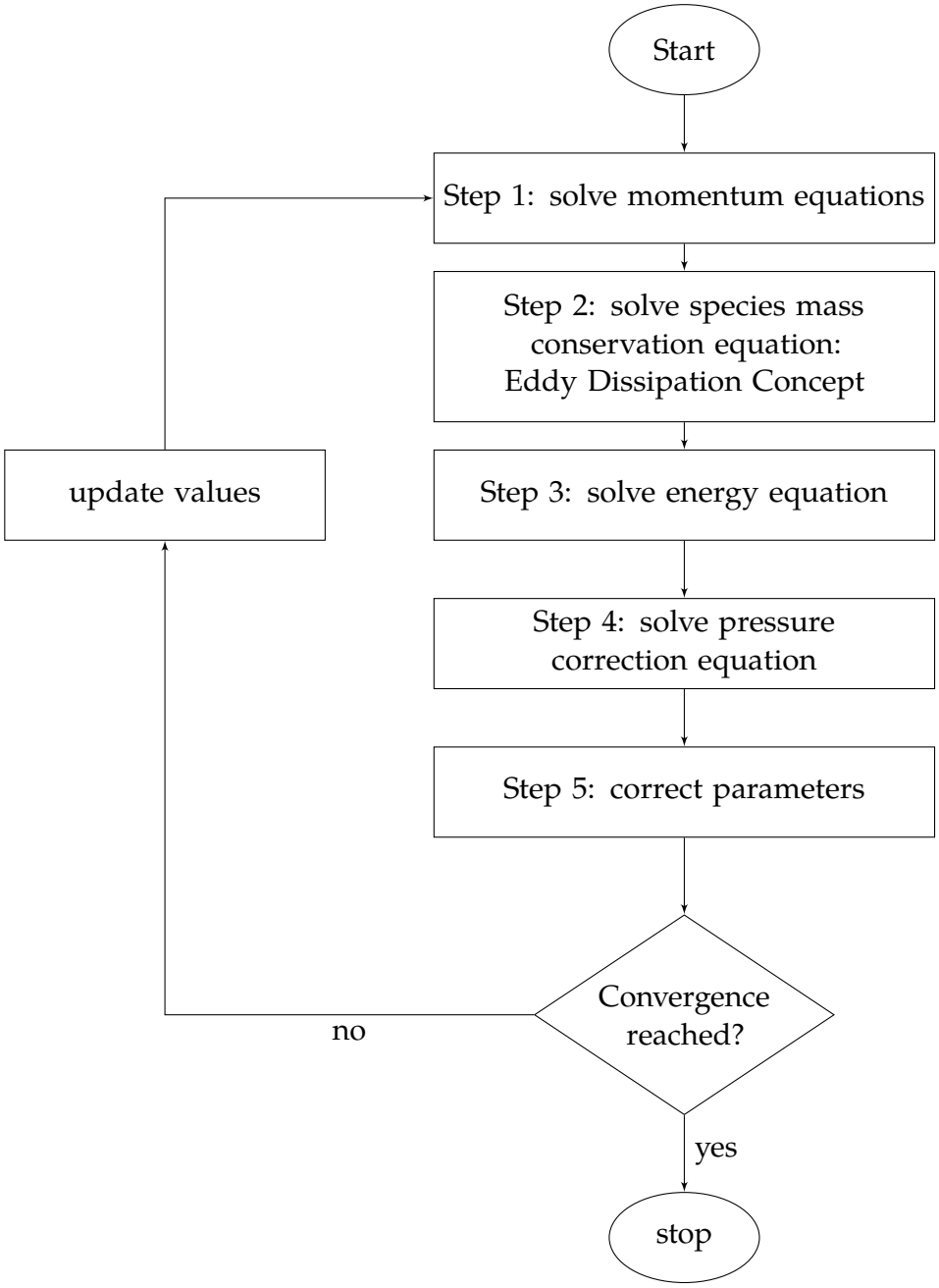

Figure 3.5: PISO algorithm in OpenFOAM

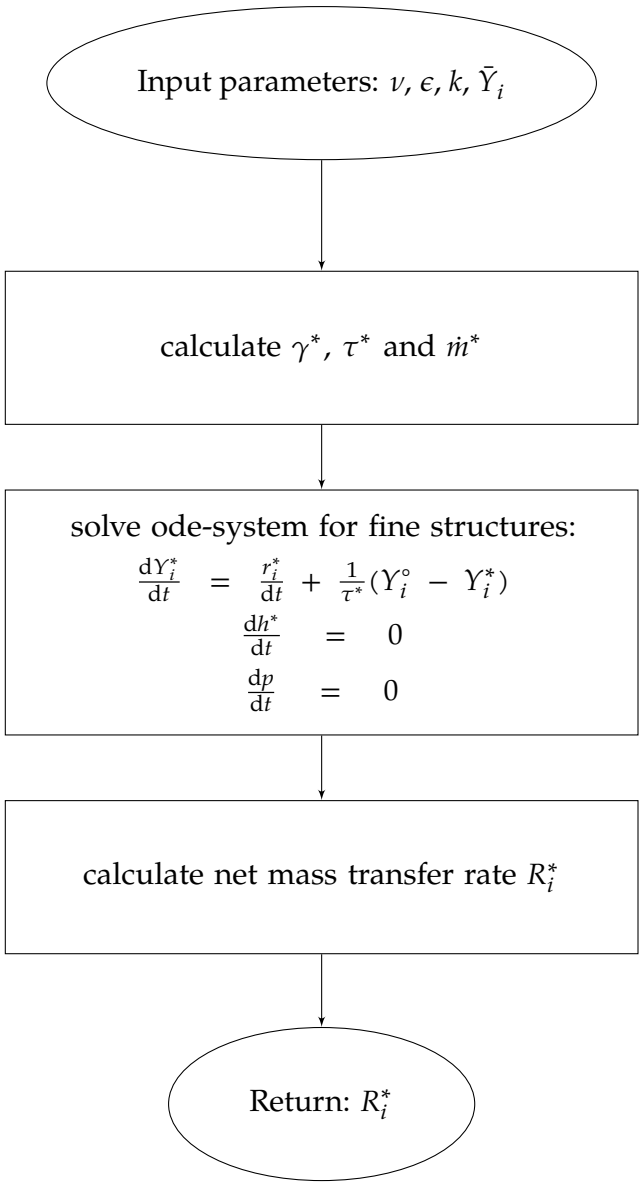

Figure 3.6: Algorithm for the EDC

The jet Reynolds number is approximately 22400 and shows small signs of local extinction. This flame has been extensively studied and measurement data for composition and velocity is provided by Barlow et al. (2005) and Schneider et al. (2003).

Besides the chemistry interaction, which is modeled by the EDC, also the turbulence has to be computed. This will be done by a two-equation turbulence model, described in section 2.1.3 and 2.1.4. The standard k-ϵ model will be used with the standard coefficients given in Table 2.1, with a modification of $C_{\varepsilon 1}$ to 1.6 and a modification of $C_{\varepsilon 2}$ to 1.6. The change of $C_{\varepsilon 1}$ was used in simulations presented by Roekaerts et al. (2000) and Li et al. (2017b) and showed good results for Sandia Flame D and JHC Burner. The modification of the constant $C_{\varepsilon 2}$ has been proposed by various researchers for Flame D simulation, e.g. Roekaerts et al. (2000), Chen et al. (1999), Zahirović et al. (2010) and has been modified to 1.6 in (Roekaerts et al. 2000) and (Zahirović et al. 2010) and to 1.8 in (Chen et al. 1999). Zahirović et al. (2010) investigated those turbulence models for application to Flame D in ANSYS Fluent and concluded that the realizable k-ϵ model is the most suitable. Therefore, this model will also be used for the flame simulations. Due to the high computational effort when using detailed chemical kinetics, the different turbulence models will be first tested on the coarsest grid used in the grid convergence study with a global mechanism. The best fitting turbulence model is then used for further simulations.

Modifications of the reaction source term, compared to the original formulation, have been proposed by Magnussen (1981) and Magnussen (2005), see section 2.2. To compare the different formulations, Sandia Flame D will be simulated using each of those with a global and a detailed chemical mechanism, respectively. Those calculations will only be conducted on the coarsest grid due to computational limitations.

For the comparison of the implemented operator splitting mechanism, the operator splitting with ISAT and the direct integration, the original formulation from Magnussen (1981) will be used.

All simulations to be carried out after the grid study are summarized in Table 3.6 with the different parameters.

3.3.3 Chemical time scale calculation

The chemical time scale definitions investigated in Python were integrated as a post processing tool in OpenFOAM, called “chemicalTimeScales”. The chemical time scales will be computed for Flame D, employing a global mechanism and a detailed mechanism to compare the effect of radical species on the chemical time scale. Furthermore, the turbulent Damköhler number will be computed to investigate if the chemical time scale calculations give reasonable results for Sandia Flame D.

Table 3.6: Simulationmatrix carried out for Flame D

Case	EDC version	mechanism	operator splitting	ISAT	turbulence model
1	original	global	off	off	standard k-ϵ
2	original	global	off	off	st. k-ϵ, $C_{\varepsilon 1} = 1.6$
3	original	global	off	off	st. k-ϵ, $C_{\varepsilon 2} = 1.6$
4	original	global	off	off	realizable k-ϵ
5	original	GRI-3	off	off	standard k-ϵ
6	original	GRI-3	off	off	st. k-ϵ, $C_{\varepsilon 1} = 1.6$
7	original	GRI-3	off	off	st. k-ϵ, $C_{\varepsilon 2} = 1.6$
8	original	GRI-3	off	off	realizable k-ϵ
9	original	global	off	off	to be chosen
10	1989	global	off	off	to be chosen
11	2005	global	off	off	to be chosen
12	original	GRI-3.0	off	off	to be chosen
13	1989	GRI-3.0	off	off	to be chosen
14	2005	GRI-3.0	off	off	to be chosen
15	original	GRI-3.0	on	off	to be chosen
16	original	GRI-3.0	on	on (tol:10^{-4})	to be chosen
17	original	GRI-3.0	on	on (tol:10^{-6})	to be chosen

4 Results and Discussion

4.1 Operator Splitting

The results of the operator splitting test cases defined in section 3.1.2 are shown in Figure 4.1 to Figure 4.4. For all cases the methane mass concentration and the temperature were plotted over time. The calculations were all carried out for the same time, five seconds, but in some figures the results are only shown for a shorter time, because the gradients are the highest in the beginning and, therefore, the biggest deviations between direct integration and operator splitting can be seen there.

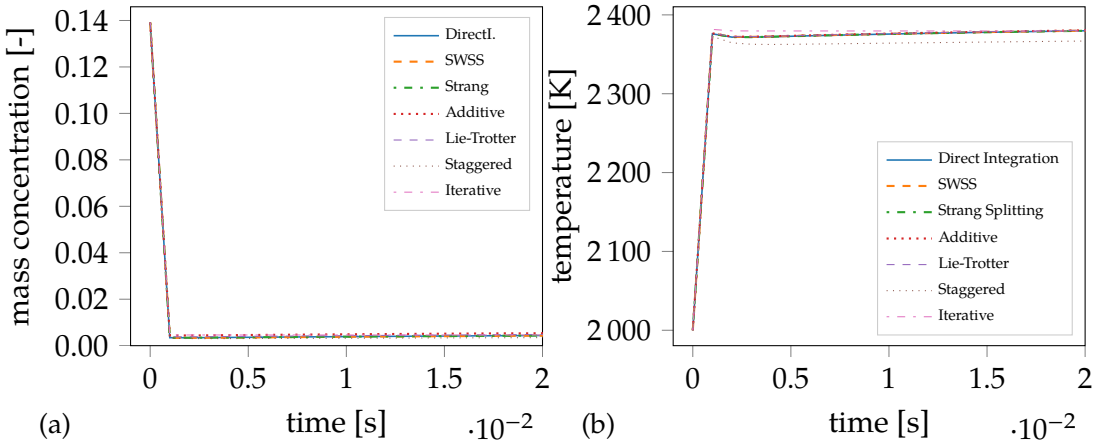

Figure 4.1: Operator Splitting - (a) methane mass concentration in Case 1 (b) temperature in Case 1

Iterative and staggered splitting show the highest deviations compared to direct integration for most cases. Therefore, it can be concluded that those operator splitting methods should not be used in the context of the EDC and will not be used for the flame simulation in the following. For cases one to four the obtained data from all the remaining methods show good agreement with the data obtained by direct integration. One exception is the methane mass concentration calculated by Additive splitting in Case 2 (Figure 4.2(a)). There, the results from Additive splitting are diverge significantly.

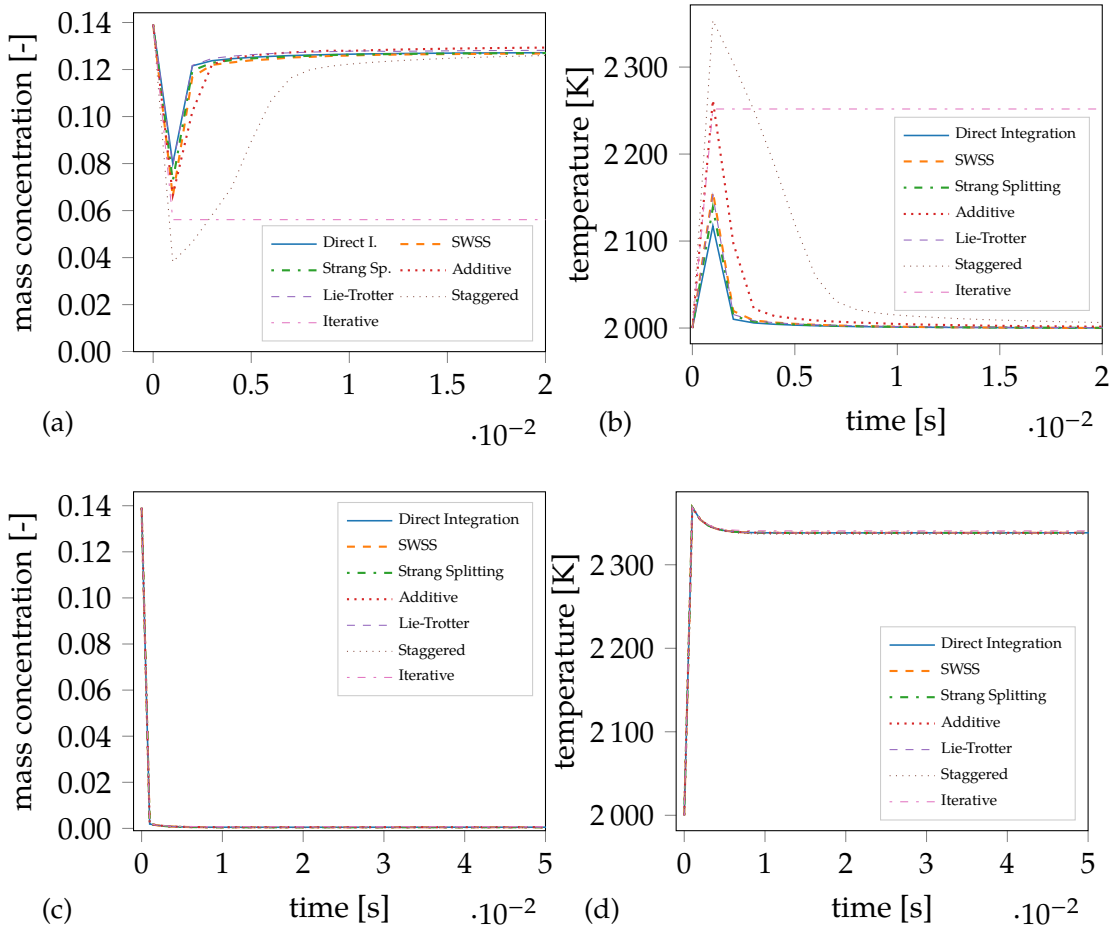

Figure 4.2: Operator Splitting - (a) methane mass concentration in Case 2 (b) temperature in Case 2 (c) methane mass concentration in Case 3 (d) temperature in Case 3

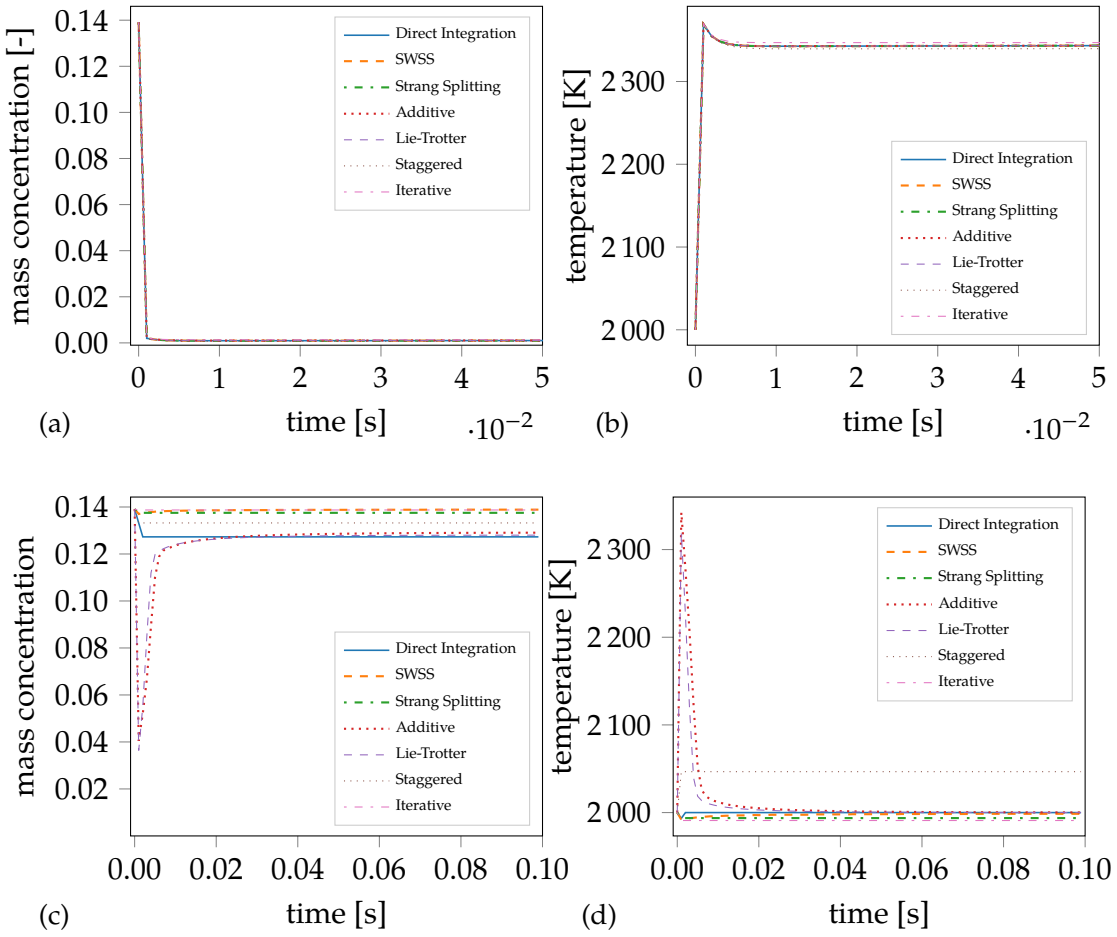

Figure 4.3: Operator Splitting - (a) methane mass concentration in Case 4 (b) temperature in Case 4 (c) methane mass concentration in Case 5 (d) temperature in Case 5

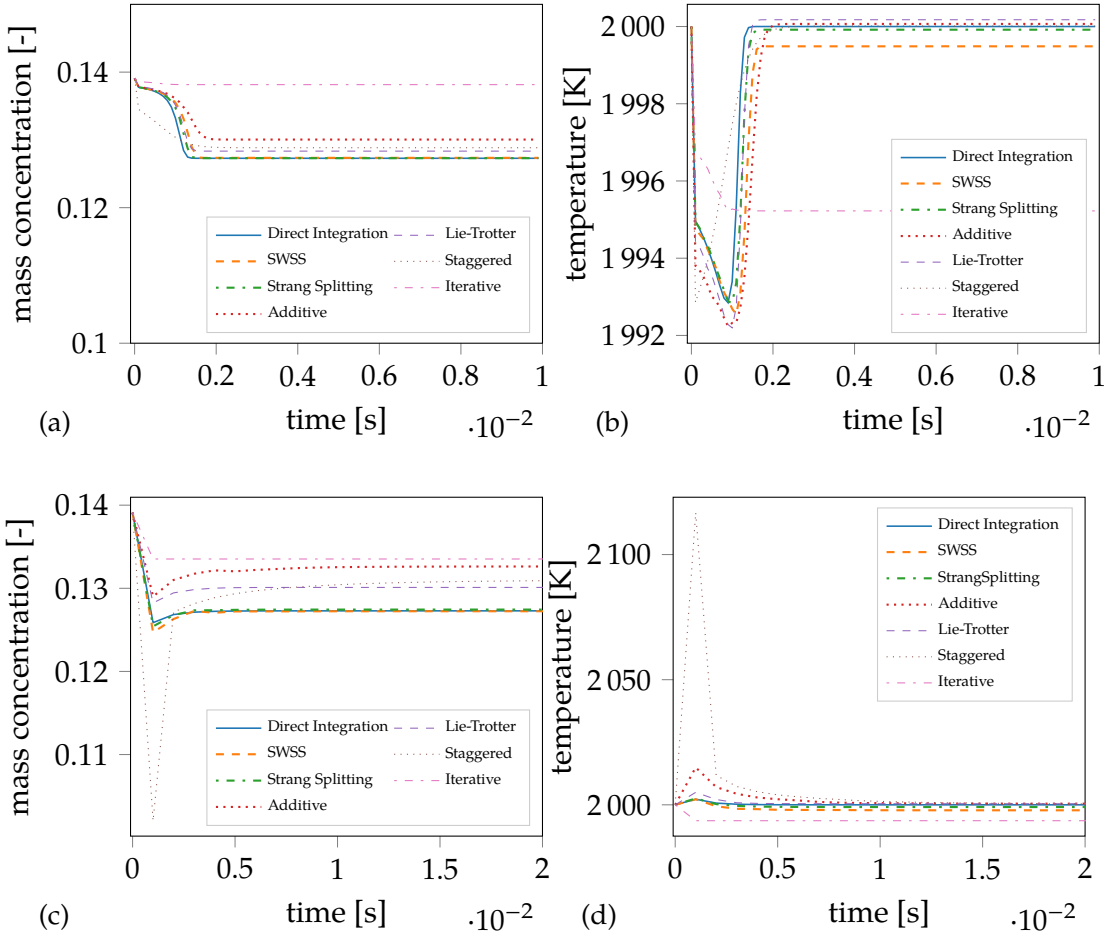

Figure 4.4: Operator Splitting - (a) methane mass concentration in Case 6 (b) temperature in Case 6 (c) methane mass concentration in Case 7 (d) temperature in Case 7

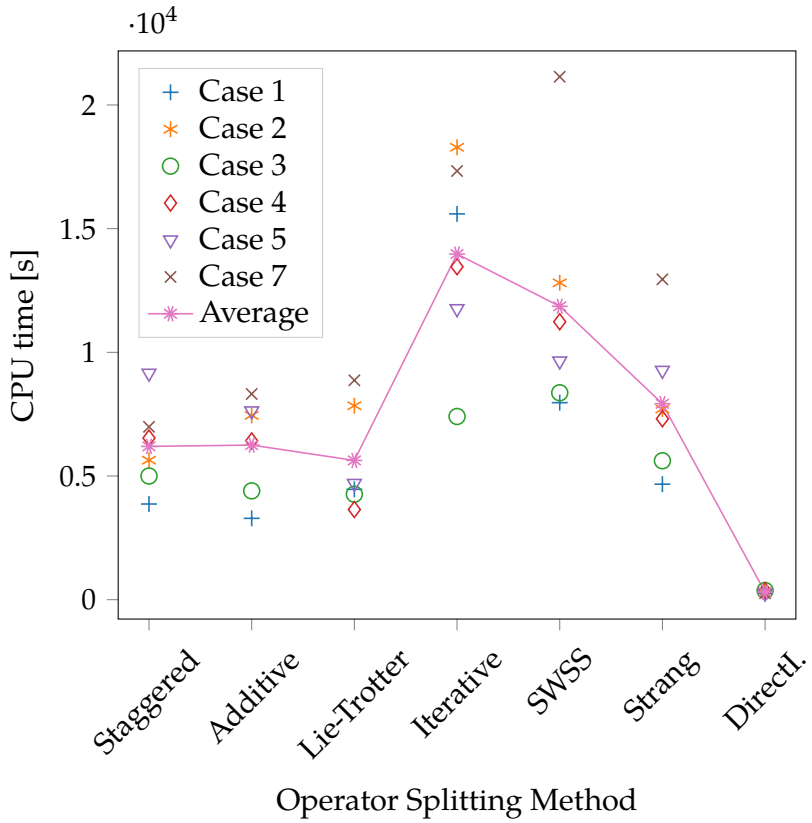

Figure 4.5: Computational time of the different Operator Splitting Methods

In Case 5 none of the used operator splitting methods gives the same mass concentration and temperature profiles as the direct integration. A reason might be that the chosen initial conditions for temperature and composition do not work well with the input parameters $\dot{m}^*$ and τ^*. However, they might not occur in this combination in the flame simulation and, therefore, give nonphysical results. Moreover, the results from direct integration do not seem very reasonable. Therefore, Case 5 is not taken into account in the following considerations.

For Case 6 Strang splitting shows the best results. The swss gives also quite good results for the methane mass concentration but lacks of accuracy for the temperature. Strang splitting and swss also give the best results for Case 7.

Figure 4.5 compares the calculation times of all test cases. It shows that direct integration is by far the fastest method using time steps of 10^{-5} seconds. Since the time step is quite small, the function calls contribute to a great part to the overall computational cost. As described in section 2.3, the operator splitting methods need two to four times more function calls than direct integration. One improvement in computational time can be achieved through the usage of ISAT for the chemical part of equation 3.1, which is planned for the later simulations.

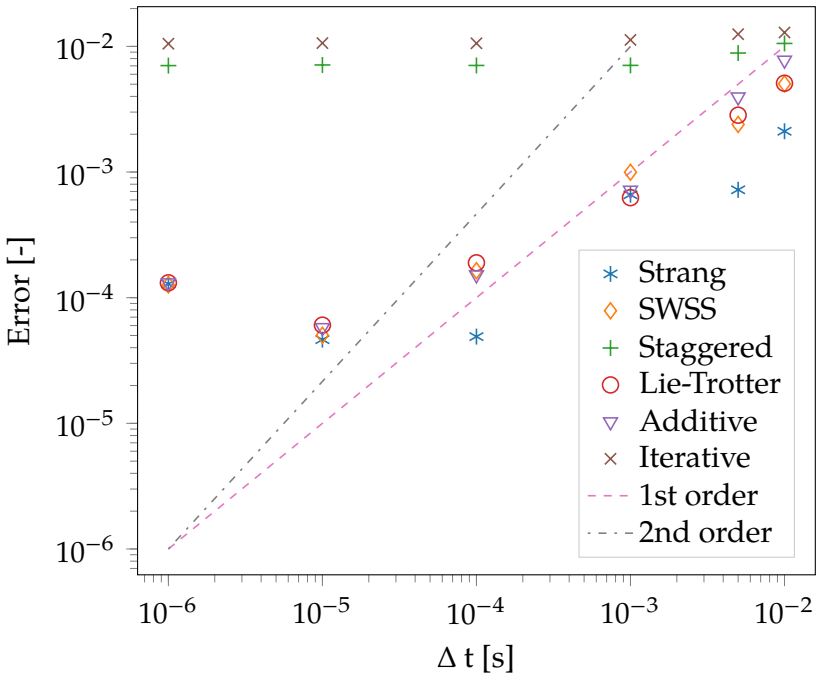

Figure 4.6: Error of the different operator splitting methods depending on Δt

The operator splitting test cases suggest that either Strang splitting or swss should be used in combination with the EDC as a result of their accuracy. As the computational time is a key factor, the more efficient method of both is chosen.As seen in Figure 4.5, this is Strang splitting.

An efficient way to reduce computational time for operator splitting is to increase the time step, since the computational cost reduces way more for the operator splitting than for direct integration when the time step increases (Figure **??**). In some cases the operator splitting methods are even faster than the direct integration.

For the order estimation of the different operator splitting methods, Case 4 was computed with varying time steps and the error was calculated as described in equation 3.3 with the methane concentration. The results are shown in Figure 4.6, including indicators for 2nd and 1st order accurate behavior. Especially for very small time steps the calculated errors do not agree with the expected order given in literature (Figure 4.6). One reason for this bad agreement in the range of small time steps could be the machine error, which effects the calculation and increases the error there. For bigger time steps starting from approximately 10^{-4} seconds, the estimated order fits well to the expected order, except for Iterative and Additive splitting.

4.2 Chemical Time Scale Definitions

4.2.1 Global Reaction

The obtained results in this work differ from the results published by Prüfert et al. (2014) (Figure 4.7). Comparing the mass concentration profiles (Figure 4.7(c) and Figure 4.7(a)) reveals that the reaction starts approximately 100 seconds later in the work of Prüfert et al. (2014) then in this work, although the same parameters for the equation were supposedly used.

With regard to the differences in the concentration, also differences in the calculated chemical time scales are expected, because the formulae for the chemical time scale depend on the concentration. It holds for both calculations that the chemical time scales change at the same time as the concentration does. This is expected, considering the dependency of τ_{che} on the concentrations. Although the time scale plots can not be the same due to different concentration profiles, some similarities in the trend can be observed for IJTS and SPTS. Still, also there is a difference of more than two orders of magnitude for those time scales.

Considering the PVTS the trend in Figure 4.7(d) and Figure 4.7(b) is totally different. The high time scales given by PVTS in the calculation of Prüfert et al. (2014) are justified by the definition of the main species for the PVTS. Only H_2O was defined as the main species this case, which is not existing in the beginning of the reaction. This might explain different results compared to the other methods, but does not explain why the trend should look as shown in Figure 4.7(d) and not as in Figure 4.7(b).

The results of the EVTS in the Python calculation did not show any trend in the chemical time scale, but gave a scattered plot with time scales in the order of 10^{19} to 10^{-5} and was therefore excluded from Figure 4.7(b).

Since the global reaction presents a very simple system, there is an analytical solution for the eigenvalues (equation 4.1). This algebraic solution was also included in Figure 4.7(d) and shows a good agreement with all definitions besides PVTS, SPTS and Ren's Product time scale. The reason for the deviation of the chemical time scale calculated by Ren's Product time scale can be explained: τ_{che} is only calculated dependent on the product species, similarly as PVTS here. The product is not available until the reaction starts and, therefore, can not give accurate predictions of τ_{che} before H_2O is present. The same argumentation holds for PVTS.

$$\lambda_i = \begin{cases} -\left(2 * r * y_{\text{H}_2} y_{\text{O}_2} + r y_{\text{H}_2}^2\right) \\ 0 \\ 0 \end{cases} \tag{4.1}$$

The differences in the results of the Python calculation and the results of Prüfert et al. (2014) might be due to different parameters used in equation 3.8. Nevertheless,

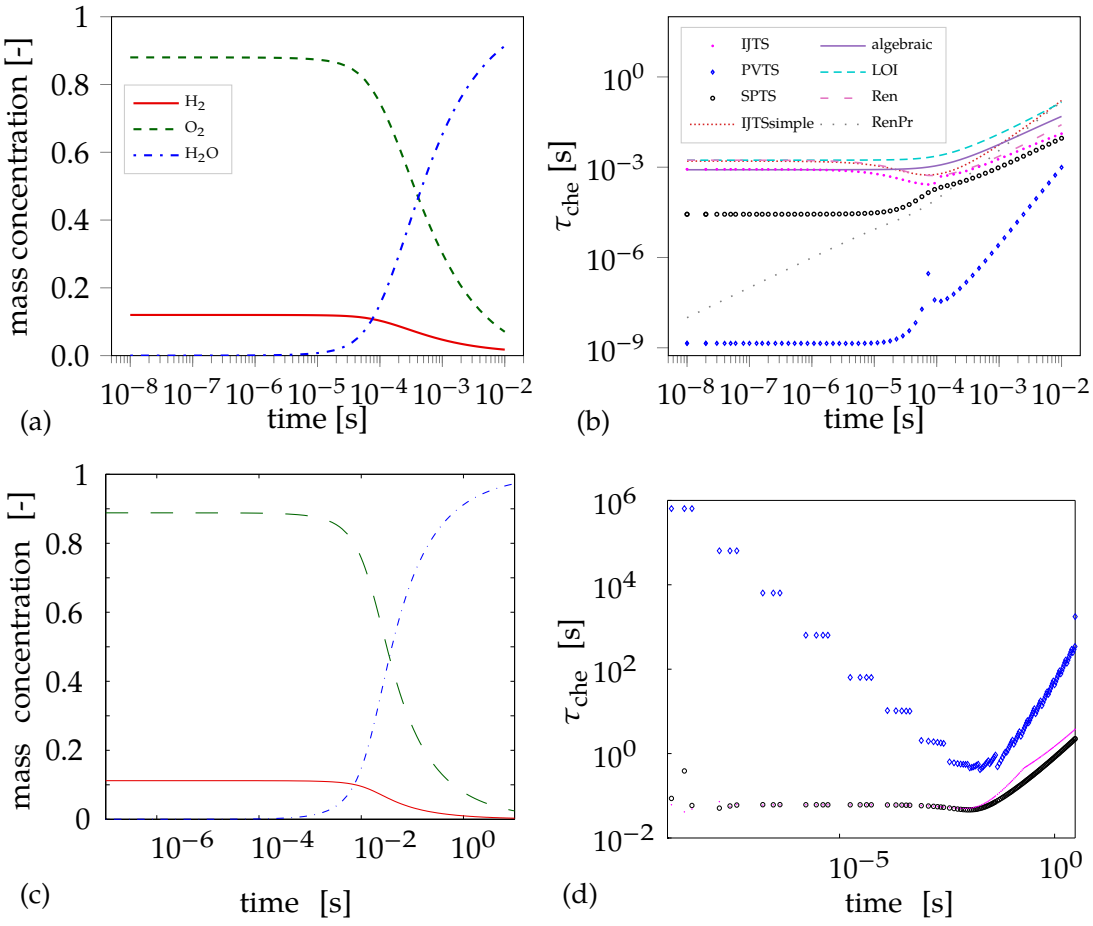

Figure 4.7: Concentration of the global reaction (a) from calculation in Python (c) adapted from (Prüfert et al. 2014) and chemical time scales of the global reaction (b) from calculation in Python (d) adapted from (Prüfert et al. 2014)

all the methods which agree well with the algebraic solution might be promising. More information can be drawn from further investigations on more complex test cases, which are explained in the following paragraphs.

4.2.2 Homogeneous reactors - (Prüfert et al. 2014)

The results of the test cases, which were also taken from (Prüfert et al. 2014) as described in section 3.2.2, are presented in this section. Concentration profiles obtained by the Python calculations are compared to the ones from Prüfert et al. (2014). They show a very good agreement (Figure 4.8 to Figure 4.10). This is an improvement compared to the results from the global reaction, shown in section 4.2.1.

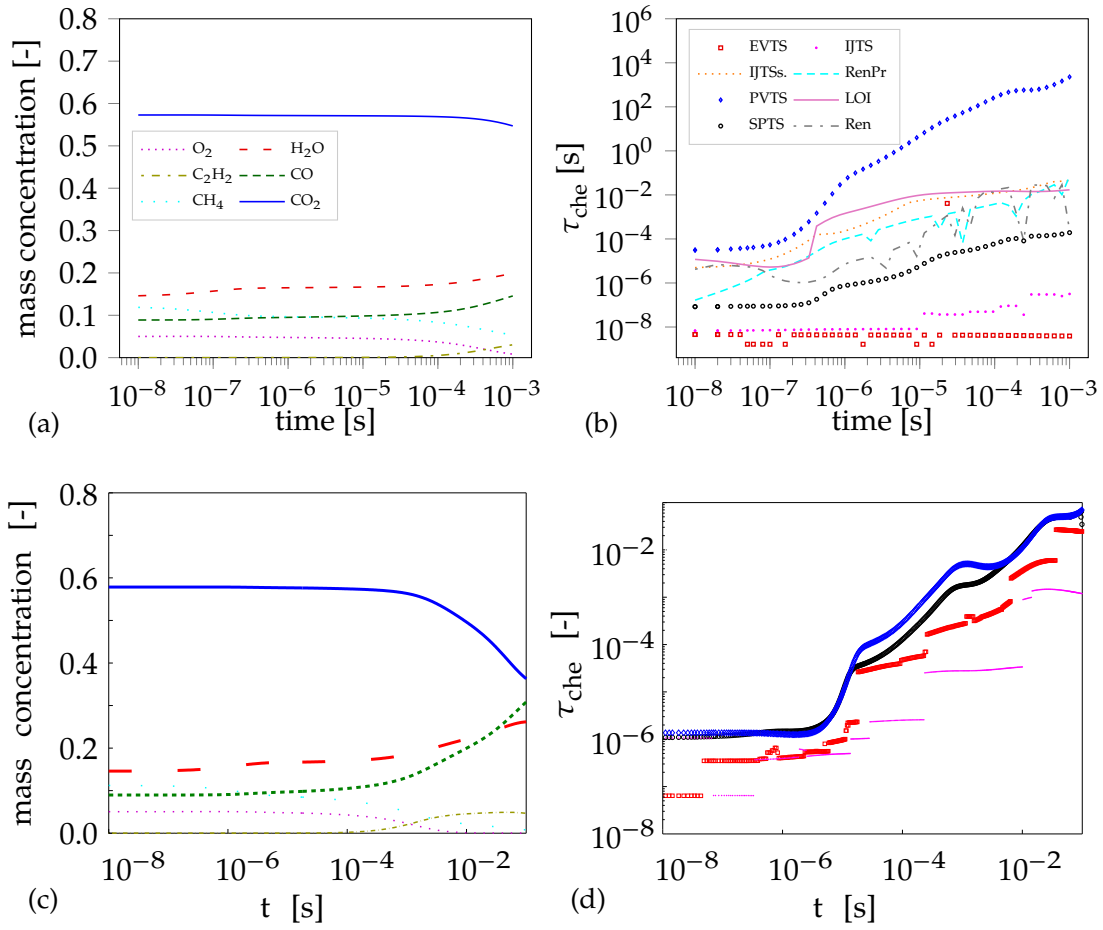

Figure 4.8: Concentration of HR1 (a) from Python calculation (c) adapted from (Prüfert et al. 2014) and chemical time scales (b) from Python calculation (d) adapted from (Prüfert et al. 2014)

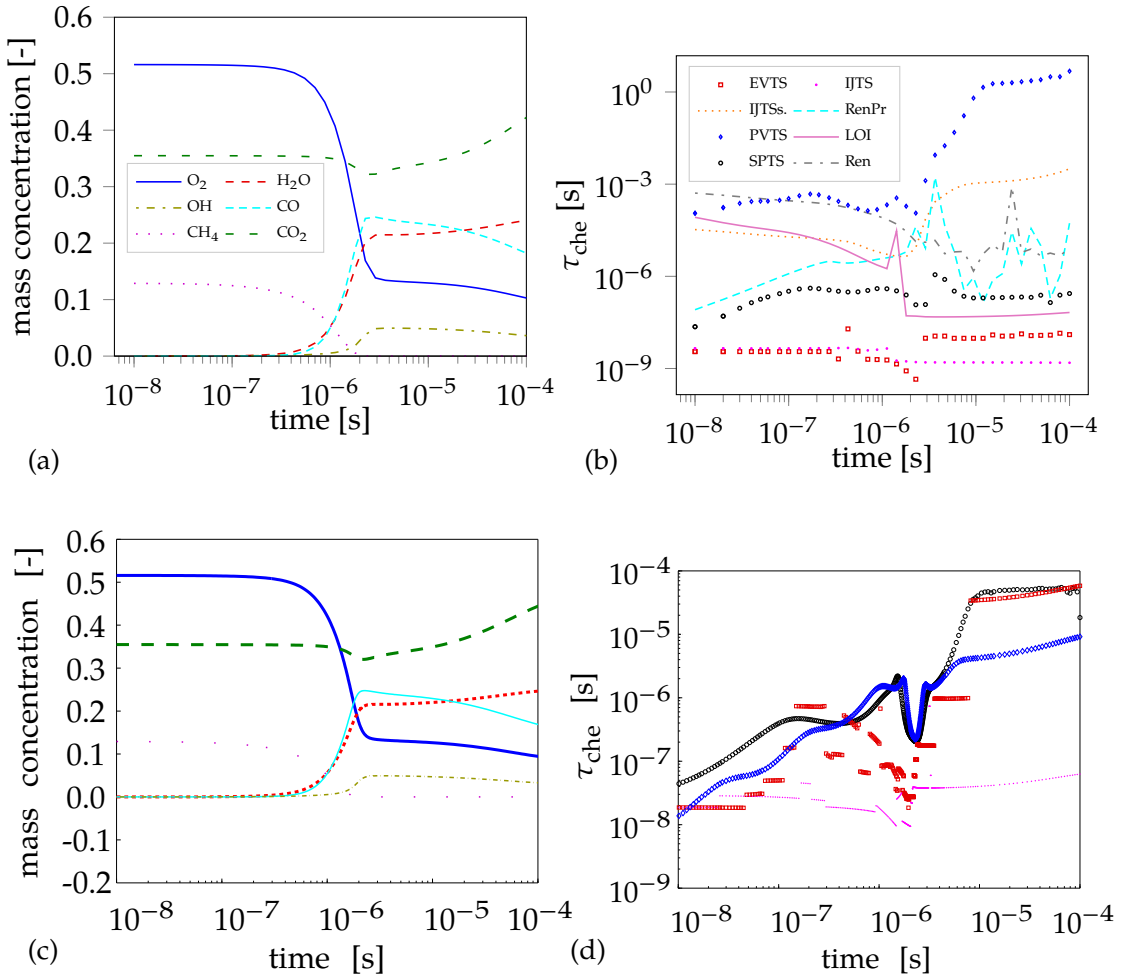

Figure 4.9: Concentration of HR2 (a) from Python calculation (c) adapted from (Prüfert et al. 2014) and chemical time scales (b) from Python calculation (d) adapted from (Prüfert et al. 2014)

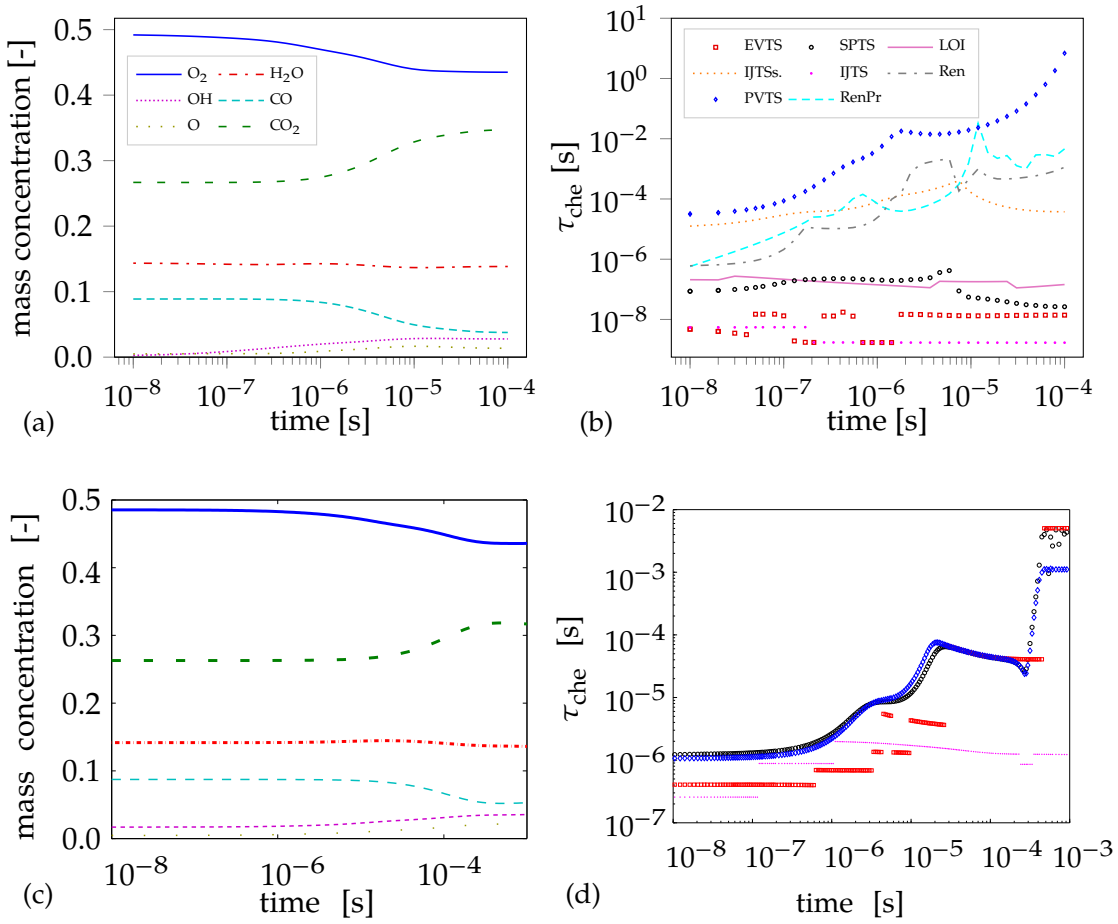

Figure 4.10: Concentration of HR3 (a) from Python calculation (c) adapted from (Prüfert et al. 2014) and chemical time scales (b) from Python calculation (d) adapted from (Prüfert et al. 2014)

The chemical time scales' temporal evolution (Figure 4.8 to Figure 4.10) for the methods calculated by Prüfert et al. (2014) as well as for this thesis show differences in the results. The magnitude of τ_{che} is always different, but there is some resemblance in the trend for SPTS, IJTS and PVTS. The differences might be explained by the employed numerical methods for the computation of the Jacobian and the eigenvalue/eigenvector decomposition. In (Prüfert et al. 2014) Matlab was used for the calculation, which partly uses different methods for the mentioned numerical calculations than Python. Furthermore, the used chemistry library, Cantera from Goodwin and Speth (2017), was taken from different release versions, which could also lead to a difference although the same mechanism has been used, GRI-3.0 from (Smith et al. 2017).

Since there are no measurements of chemical time scales and no other computation of similar cases in literature available, there is still some uncertainty in the results of the methods. Thus, no proper method could be identified. Therefore, this grants the results from the flame simulation test cases in section 4.2.3 special importance, because these can be qualitatively validated with the Damköhler number, as described in section 3.2.2.

4.2.3 Test cases from flame simulation

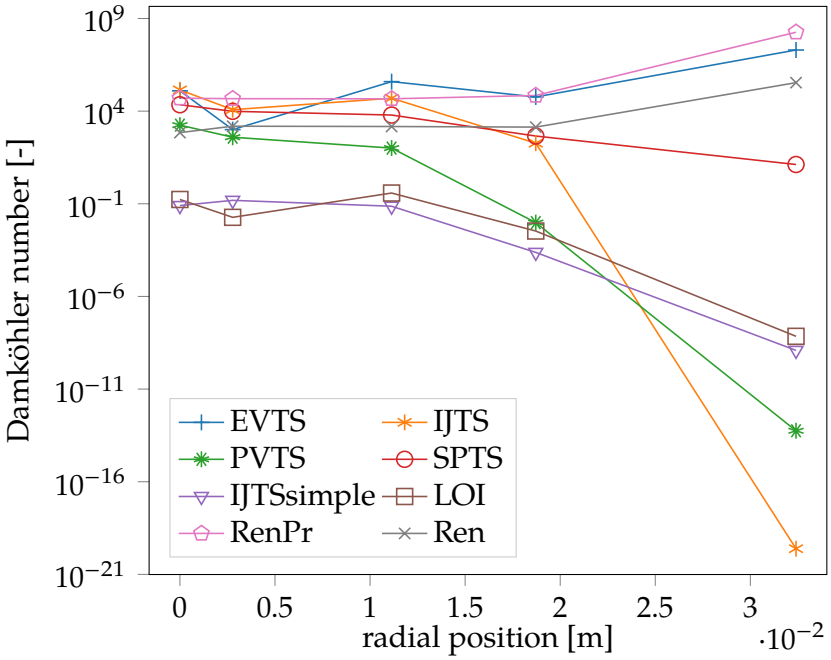

Figure 4.11: Radial profile of the Damköhler number 0.35 m upstream the burner tip

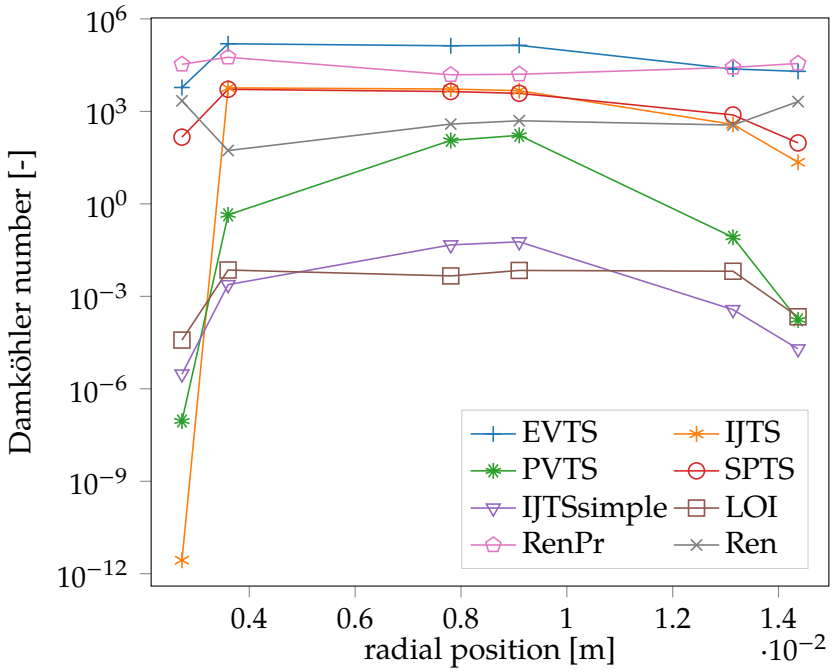

Figure 4.12: Radial profile of the Damköhler number 0.20 m upstream the burner tip

For the test cases defined in section 3.2.2, the Damköhler number has been computed and plotted over the radial position. The results for the radial profile at 0.35 m and 0.20 m meter upstream the burner tip are shown in Figure 4.11 and Figure 4.12. Since the combustion in Flame D is mixing controlled, the Damköhler number is expected to be significantly greater than unity. Furthermore, the radial profile of Damköhler is supposed to be "W"-shaped because it is an under stoichiometric flame. Such flames feature an inner and an outer reaction front and a lack of oxygen in between. As a consequence, reactions are slower in the regions which are lacking oxygen.

At 0.35 m upstream, the Damköhler number is for all presented methods above 1 near the center, except of LOI method and IJTSsimple. For the points farer away from the center, the Damköhler number differs quite a lot between the methods and even gets far below one for some. Probably the last point of investigation was chosen outside the flame reaction zone. When no reactions occur, the calculation of the chemical time scale does not work, consequently neither the calculation of the Damköhler number. The "W"-shaped profile is also not recognizable for the Damköhler number 0.35 m upstream, no matter which method is considered. This can also be due to the points chosen too far away from the burner tip and the sparse resolution in the flame zone.

For the Damköhler number 0.20m upstream the burner tip (Figure 4.12) the

calculation methods LOI, PVTS, and IJTSsimple do not give reasonable values. With the mentioned methods a Damköhler number below 1 is obtained at some points. Compared to the test cases at 0.35m upstream (Figure 4.11), the last points of the profile look much more reasonable. They seem to be still in the reaction zone. The Ren's product time scale, Ren's time scale and LOI method show the "W"-shaped profile.

One problem with the results here is that the flame was only simulated with a global mechanism. Thus, only a small number of species and no radical species are present. Since radical species are highly reactive, they might be important for the chemical time scale calculation. Therefore, it can only be concluded that Ren's product, Ren's time scale and the LOI might work for a global mechanism, but the methods should be tested when a detailed mechanism has been used. This will be done in OpenFOAM, as described in section 3.3.3.

4.2.4 Computational effort of the different methods

Figure 4.13 shows the computational expense of the different methods in the presented test cases. Ren 's and Ren's product time scale are always amongst the methods with the least computational demand. The reason is quite obvious: for Ren's and Ren's product time scale neither the Jacobian nor their decomposition has to be computed. The same holds for IJTSsimple. Also PVTS does not require the Jacobian, therefore, it also requires less computational time than other methods, e.g. EVTS.

All the other methods require the Jacobian matrix to be computed, which is computationally expensive. Therefore, the methods EVTS, IJTS, SPTS and LOI require a lot more computational time. One exception is the LOI method when applied to the global reaction (Figure 4.13(a)). Since the global reaction is a special, non-physical, case here and will not be the future application field.

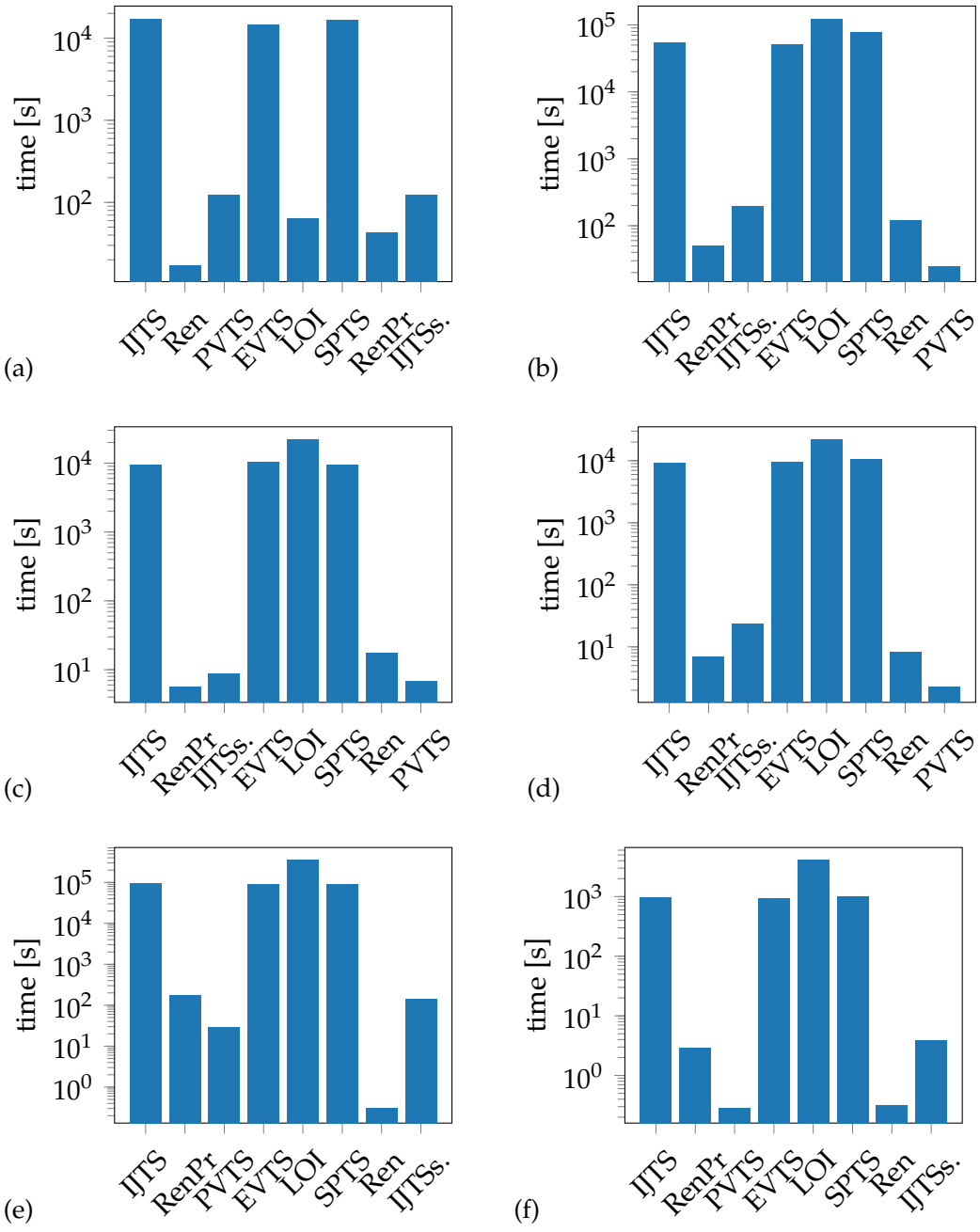

Figure 4.13: CPU time of the different methods (a) global reaction (b) HR1 (c) HR2 (d) HR3 (e) Flame simulation at 0.35 m upstream, 0.0028 m radial position (f) Flame simulation at 0.20 m upstream, y=0.0027 m radial position

4.3 Flame Simulation

4.3.1 Grid convergence study

A grid convergence study was carried out for four different grids, as explained in section 3.3.1. Originally, Sandia Flame D was simulated with a grid depicting 10 cm of the pilot and methane inlet and 50 cm from the burner tip on. Unfortunately, pressure fluctuations occurred near the inlets. These pressure fluctuations led to changes in the other parameters and for some cases even to extinction.

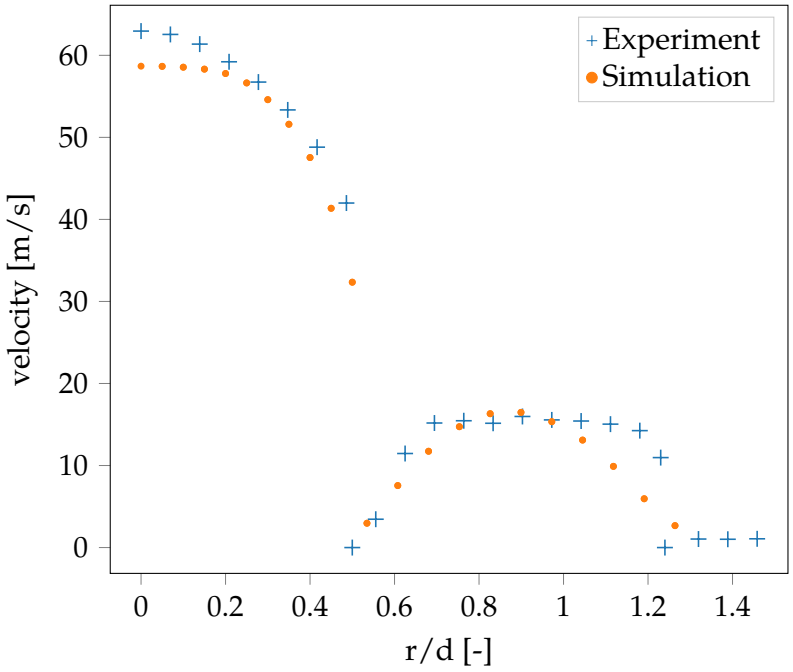

Figure 4.14: Comparison of the velocity profile at the methane and pilot exit with measurement data from (Schneider et al. 2003)

To cope with the pressure fluctuations, the pilot and methane inlet were simulated separately until a steady state profile was obtained. All relevant quantities at the exit were then mapped as boundary conditions on the jet and pilot inlet of the remaining grid (which depicts 50 cm of the flame from the burner tip on).

To ensure correct boundary conditions for the flame, the velocity profiles obtained from the simulation of the inlets were compared with measurement data from Schneider et al. (2003) for Flame D. The profiles show good agreement between simulation and measurement data (Figure 4.14). It can be concluded that mapping the inlet profiles is a valid procedure for the simulation.

To calculate the grid convergence index, the ratio of the difference between two grid solutions to the finer grid solution ζ is needed (equation 3.15), (Roache 1994).

The first problem when trying to calculate the GCI is that the different solutions are not available on the same grid points if the refinement ratio is no integer. To overcome this problem the solutions of the finer grids are mapped on the coarse grid using the mapFields utility in OpenFOAM. Additionally, mapping all the coarse grid solutions on the finest grid was tested.

Furthermore, even if the solution is available on the same points, a second problem remains on which point to choose for the calculation of ζ and which quantity to examine. Roache (1994) presented a sample problem, the Burger's equation, for calculating the GCI. There he chose one point for calculating the GCI, but it is not clear how to choose a representative point in a flame for determining the accuracy of a grid. Therefore, ζ was calculated for all grid points available using the temperature and the mean value was taken for further calculations.

Table 4.1 shows the different grids with their refinement ratio (defined with the grid listed above) and the GCI results, calculated with the values mapped on the coarsest as well as on the finest grid. The order of accuracy estimated by equations 3.16 and 3.17 was approximately 1.3 for the solution mapped on the coarse grid and 1 for the solution mapped on the fine grid. The grid convergence index shows, that the finest grid has the smallest GCI and, therefore, the most accurate results with 3.5 and 4.38 percent. The estimated error, the GCI respectively, for the coarsest grid is quite big with 13.6 and 16.6 percent.

The results differ depending on the approach used to obtain the data at certain points. However, they show the same trend and the results are in the same order of magnitude.

Table 4.1: GCI for the different grids based on the temperature

number of cells	refinement ratio	GCI [%] mapped to Coarse	GCI [%] mapped to Fine
4329	-	13.6	16.6
9628	1.5	5.17	7.5
17316	1.34	3.07	4.9
96264	2	3.5	4.38

Since it is not quite clear how the points for the grid convergence study should be chosen, the reliability of the results for the grid convergence are questionable. Furthermore, the fact that the influence of the mapping can be seen in the estimation of the order as well as in the final result, brings doubt to the reliability of the results. Therefore, the temperature, velocity and species concentrations for CH_4, CO_2, O_2 and H_2O obtained by the different grids were also compared with the measurement data for Flame D from Barlow and Frank (1998) and Schneider et al. (2003). The axial profiles from the center are shown in Figure 4.15. The other radial profiles are

shown in the appendix (Figure A.1 to Figure A.9). The plots are all scaled by the jet diameter d=7.2mm and r and x define the radial and axial position, respectively.

In general, the profiles calculated with the global mechanism by the EDC on the different grids fit quite good to the measurement data. When comparing the different graphs it is not obvious at first sight, that the finer the grid, the better it fits. Depending on which graph is considered, solutions with different grids seem to fit best. For some cases, even the solution from the coarse grid fits better, for example the CH_4 concentration profile at x/d=30 (Figure A.7(c)). Nevertheless, most of the times the fine grid solution seems to give the most accurate results. For example for the O_2 concentration profile at x/d=1 (Figure A.2(b)).

Since the best grid can not be identified with certainty by solely examining the radial and axial profiles, also the sum of squared errors (SSE) was calculated between the simulation results and the measurement data. This was done for all the radial and axial profiles available for temperature and velocity. The temperature and velocity were chosen as parameters here because they are expected to be most reliable, since the concentrations are expected to be off due to the usage of a global chemical mechanism. (Of course temperature and velocity are also influenced by the species concentrations, but this is believed to be less severe.)

Figure 4.16 shows the SSE for the different profiles and the different grids relative to the SSE of the coarsest grid. This reveals, that the finest grid, with approximately 95000 cells, gives in general the best results, although it is not the case for every radial position.

Regardless of the different grids, the simulation results show in general a reasonable agreement with the measurement data. The results from Lysenko et al. (2014b) show very similar profiles for all species concentrations presented in Figure 4.15. The profiles have kind of edges, which makes them look different than the experimental profiles. The maximum CO_2 concentration is over predicted by the simulation, which is also the case for the results presented by Lysenko et al. (2014b).

The maximum temperature is also over predicted in the simulations with the global mechanism (Figure 4.15(a)). This is not the case for the simulations presented by Lysenko et al. (2014b). The difference might be explained by the neglect of radiation in this work, which is considered by Lysenko et al. (2014b).

Although the finest grid shows the best predictions compared to the measurement data, it will not be used for the further simulations, due to the lack of computational resources. The coarsest grid, with approximately 4400 cells will be used for the simulations, since it needs less computational time. The chosen grid is shown in Figure 4.17. The results obtained by the coarse grid simulation do also match the measurement data reasonably. Furthermore, instead of simulating a few cases on a fine grid, it was decided to simulate several different cases on a coarser grid. Moreover, studies have been published, where similarly coarse grids have been used for Flame D simulation. Li et al. (2017b) used a grid with 4600 cells and Lysenko et al. (2014b) used a grid with 4400 cells (counting the cells from the

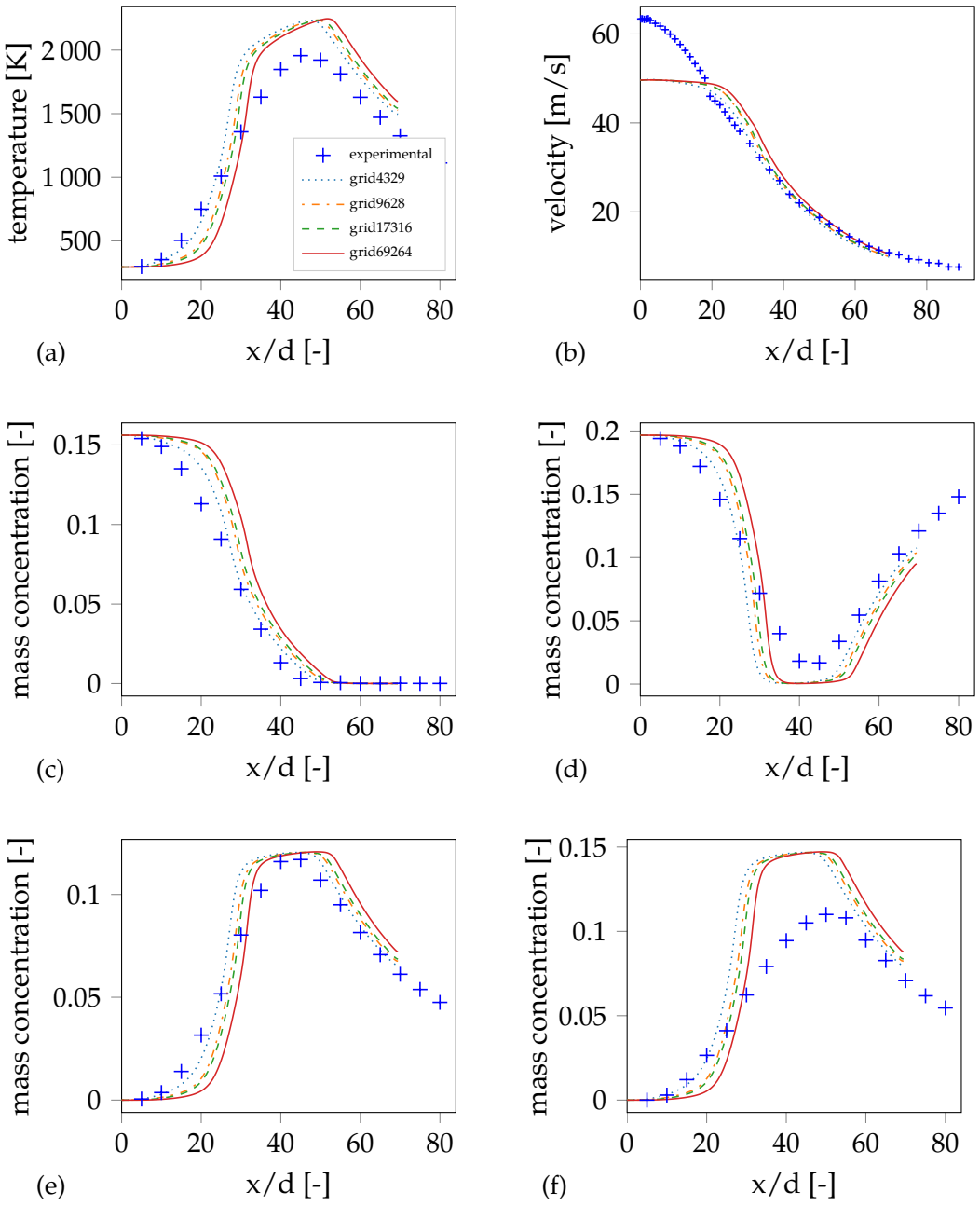

Figure 4.15: Axial profiles of the experimental data and the different grids tested in the grid convergence study for (a) temperature (b) velocity (c) CH_4 (d) O_2 (e) H_2O (f) CO_2

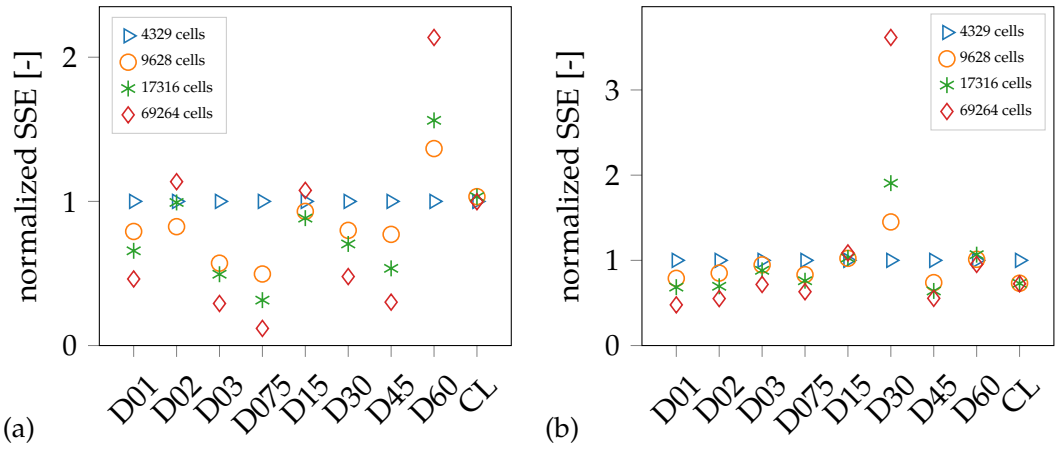

Figure 4.16: SSE normalized by the SSE of the coarsest grid for the different radial (D) and axial (CL) profiles (the number gives the radial position as x/d) for (a) temperature and (b) velocity

burner tip on).

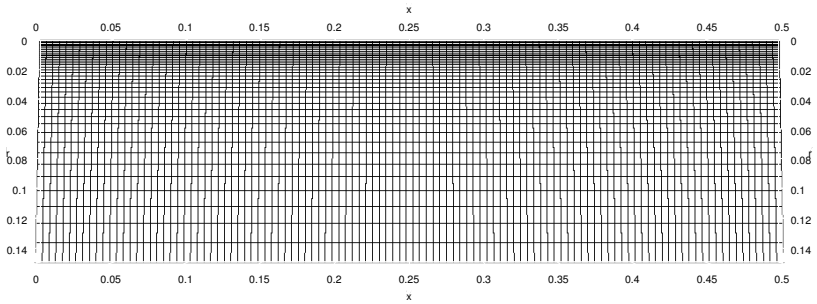

Figure 4.17: Chosen grid with 4329 cells

4.3.2 Different turbulence models

As discussed in section 3.3.2, Flame D simulations using the standard k-ϵ model, the realizable k-ϵ model and suggested constant modifications within the standard k-ϵ model are carried out using the chosen grid from the grid convergence study and a global chemical mechanism.

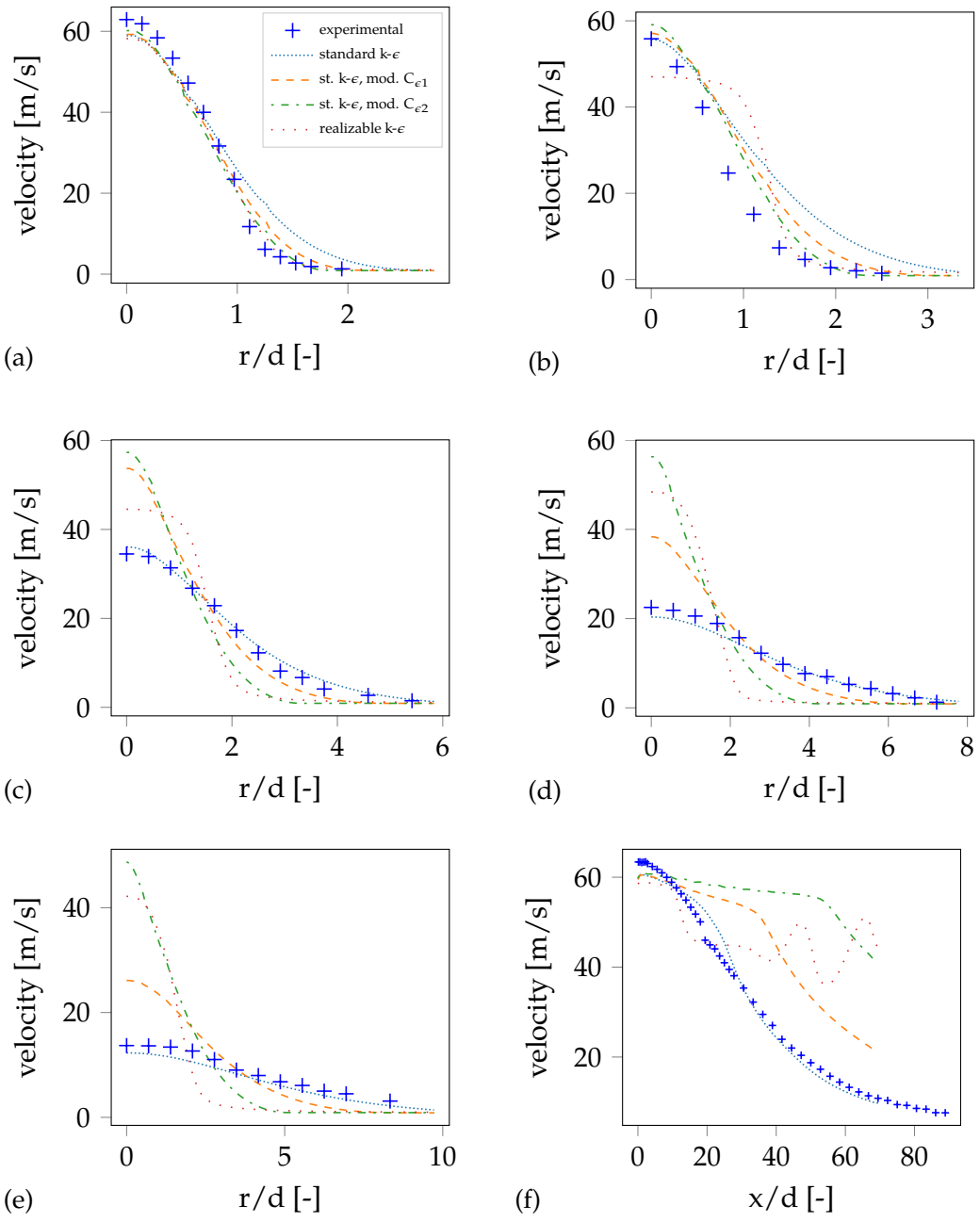

Figure 4.18: Comparison of the velocity of the different turbulence models at the radial profiles (a) x/d=7.5 (b) x/d=15, (c) x/d=30, (d) x/d=45, (e) x/d=60 and (f) at the center line

Figure 4.18 shows the velocities obtained by the simulations with the different turbulence models at selected radial and axial locations. For the radial profile at x/d=7.5 the realizable *k*-ϵ model seems to fit best to the experimental data. In contrast, for all the other profiles it gives worse predictions for the velocity than the standard *k*-ϵ model.

Zahirović et al. (2010) also tested different turbulence models for simulating Flame D and concluded that the realizable *k*-ϵ model gives the best results. They used ANSYS Fluent instead of OpenFOAM. Probably the turbulence models are implemented slightly different in the CFD codes and this leads to different results. Furthermore, ANSYS Fluent approximates the CSR by a plug flow reactor (PFR) to speed up and facilitate the simulations. This could also lead to different results.

Figure 4.18(e) shows the radial profile at x/d=60. The simulation using the realizable *k*-ϵ model gives non-reasonable results there. It seems like the velocity (and also the other quantities) calculated by the realizable *k*-ϵ model is unstable farer away from the burner tip (Figure 4.18(f)).

The proposed modifications of the model constants $C_{\epsilon 1}$ and $C_{\epsilon 2}$ also do not reach the accuracy of the standard *k*-ϵ model with standard coefficients. Only for the radial profiles at x/d=7.5 and x/d=15 (Figure 4.18(a) and Figure 4.18(b)) the predicted velocity, computed using the standard *k*-ϵ model with modified constants, fits quite well to the measured velocity. At the profiles farer away from the burner tip, the velocity is totally over predicted with the changed constants. Obviously, the jet spread rate of the flame is under estimated by the modified turbulence models. Therefore, the succeeding simulations are carried out using the standard *k*-ϵ model with the standard model constants given in Table 2.1.

4.3.3 Modifications of the EDC

Using a global chemical mechanism

In section 2.2 different modifications of the mass transfer rate formulation are presented. As discussed in section 3.3.2, the three different modifications will be used for a Flame D simulation on a coarse grid, with a global chemical mechanism, to compare their results. Figure 4.19 shows the axial profiles for temperature, velocity and the species concentrations of CH_4, O_2, H_2O and CO_2 obtained by the different simulations. There is hardly any deviation between the results obtained by the different EDC versions. The other radial profiles reveal only a slight difference between the EDC modifications for the simulation of Flame D, see Appendix Figure A.10 to Figure A.17.

The modifications were introduced to enhance the prediction of the chemical reaction. Probably Flame D is a quite basic case, where already the original EDC formulation gives reasonable predictions. The influence of the chemical mechanism, or the chosen variant of fine structure modeling could have a greater impact on

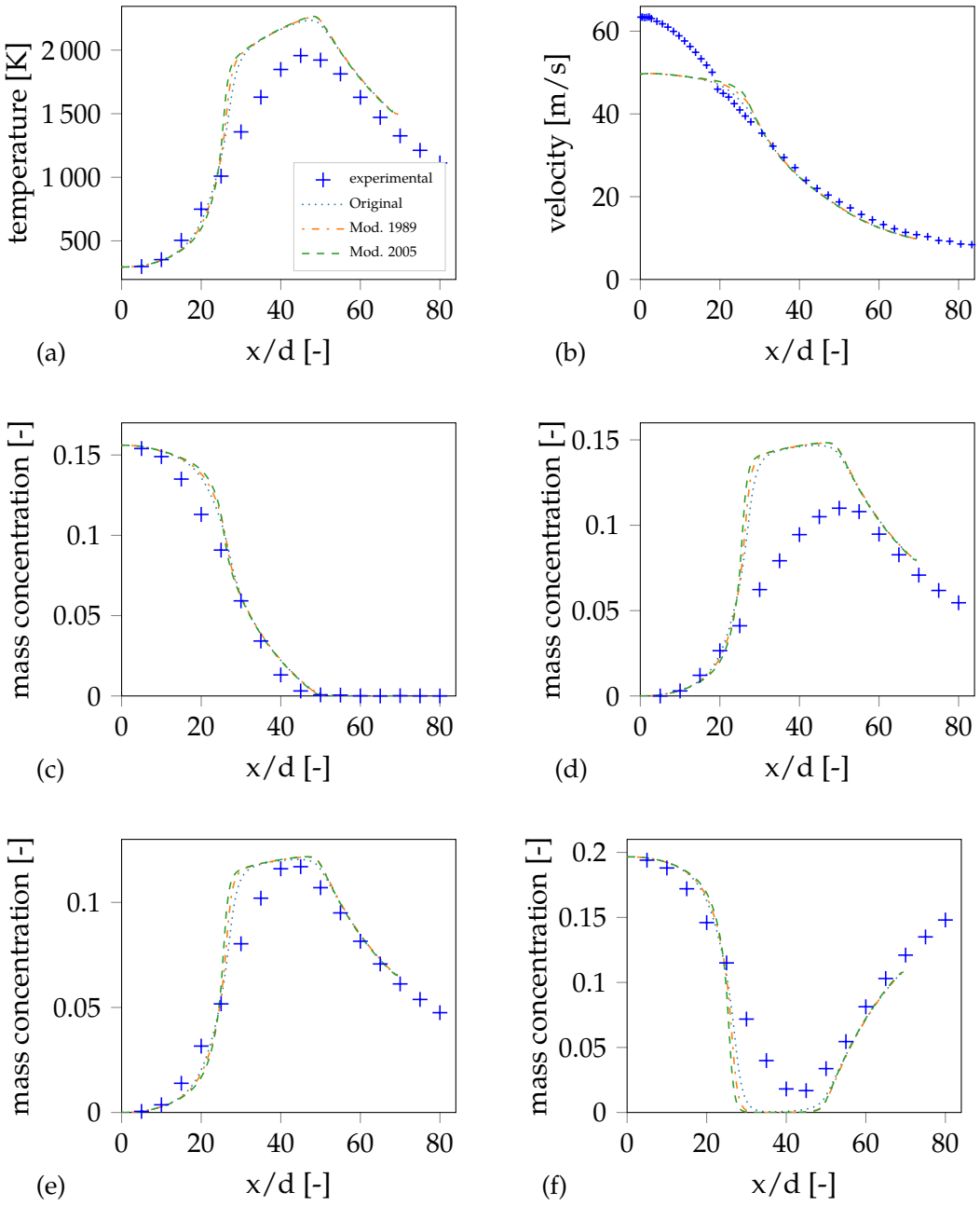

Figure 4.19: Axial profiles at centerline comparing the different EDC modifications for (a) temperature, (b) velocity, and species mass concentration (c) CH_4, (d) CO_2, (e) H_2O and (f) O_2

Flame D than the modifications of the reaction source term. To investigate the influence of the different EDC versions when using a detailed chemical mechanism, also simulations with GRI-3.0 will be carried out.

The original formulation of the EDC fits the best for the Flame D simulation here, since its profile looks a little smoother than the others. Especially the temperature and the O_2 concentration at the centerline computed using the original formulation fit slightly better to the measurement results (Figure 4.19(a) and Figure 4.19(f)).

Using a detailed chemical mechanism

The different modifications for the reaction term have also been tested with a detailed chemical mechanism, the GRI-3.0, using the standard k-ϵ model for turbulence modeling. Problems with ignition occurred clipping γ_L to 0.75 when the original EDC version and the modification from 1989 were used. γ_L is not allowed to become one, since this will lead to a division by zero in the transfer term calculation. Therefore, the value has to be forced below one. Furthermore, getting a value of close to one, might already lead to instabilities in the simulations. Therefore, the clipping value was increased for those cases to 0.9. This lead to ignition during the simulation and reasonable results compared to experimental data.

Figure 4.20 shows the axial profiles for temperature, velocity and species concentration at the centerline. Compared to the results from the different modifications with the global mechanism, all the predictions fit better to the experimental data. Comparing the results from the different modifications with each other, there is obviously more difference when using a detailed chemical mechanism than when using a global one. The original version and the version from 2005, give better predictions for the axial temperature at the centerline than the version from 1989 (Figure 4.20(a)).

Figure 4.20(d), Figure 4.20(e) and Figure 4.20(f) show the CO_2, H_2O and O_2 concentration at the centerline. For those cases the original version fits best to the experimental data, but also the others fit well.

At some radial profiles (Figure A.20(a) and Figure A.21(a)) the temperature is under predicted by the newest version of the EDC, the version from 2005. Figure A.18 to A.25 show the other radial profiles for the modifications.

The SSE has also been calculated for those simulations for the temperature and the species concentration of CH_4, CO and NO. The SSE results were normalized by the SSE of the original one. Figure 4.21 shows the results and reveals, that the original version and the modification from 2005 fit better than the modification from 1989. For the radical species, such as NO and CO (Figure 4.21(c) and Figure 4.21(d), the newest modification fits best, but for the CH_4 concentration and the temperature the original version fits better at most locations. Therefore, the original version will be used for the following simulations.

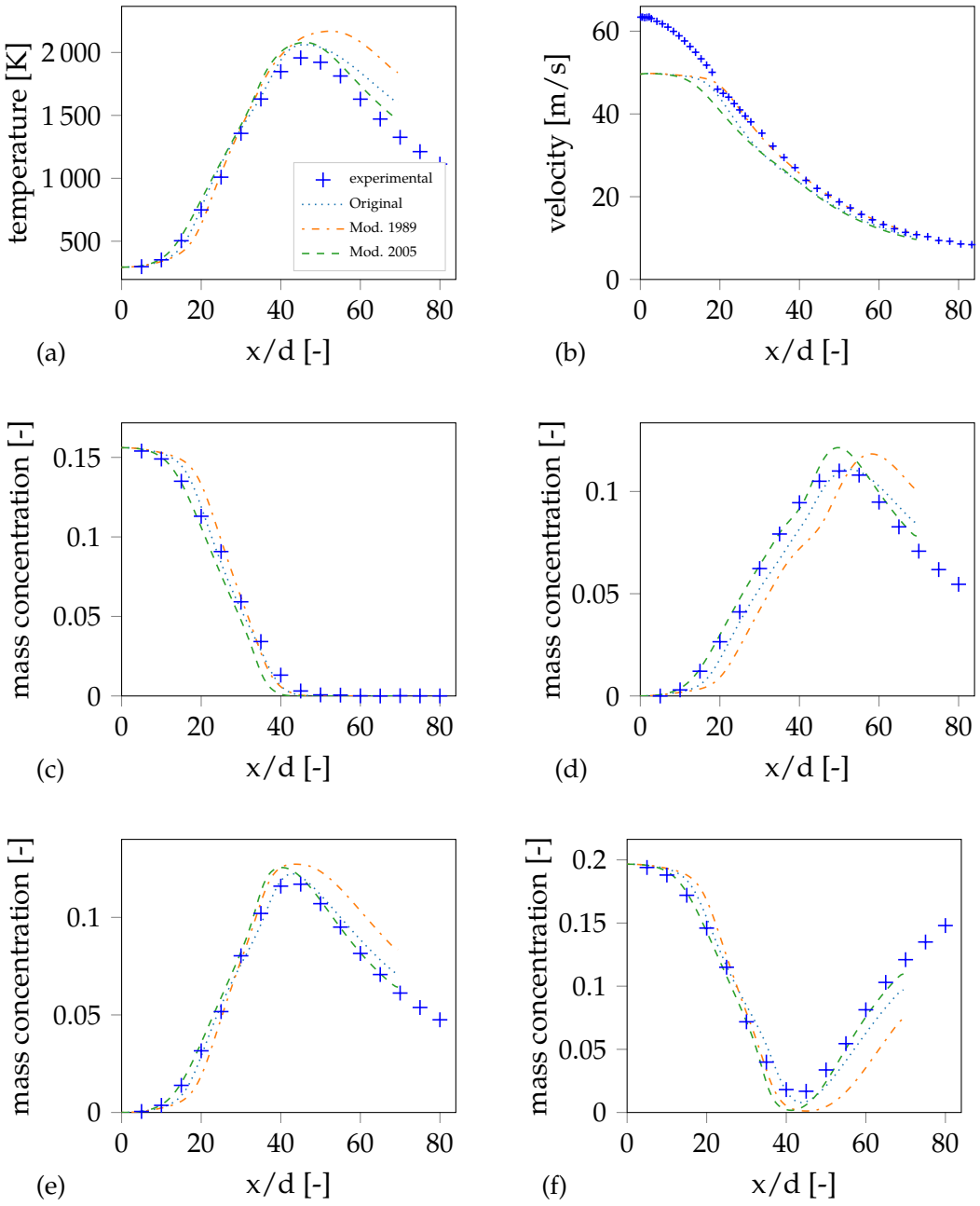

Figure 4.20: Axial profiles at centerline comparing the different EDC modifications using GRI-3.0 (a) temperature, (b) velocity, and species mass concentration (c) CH_4, (d) CO_2, (e) H_2O and (f) O_2

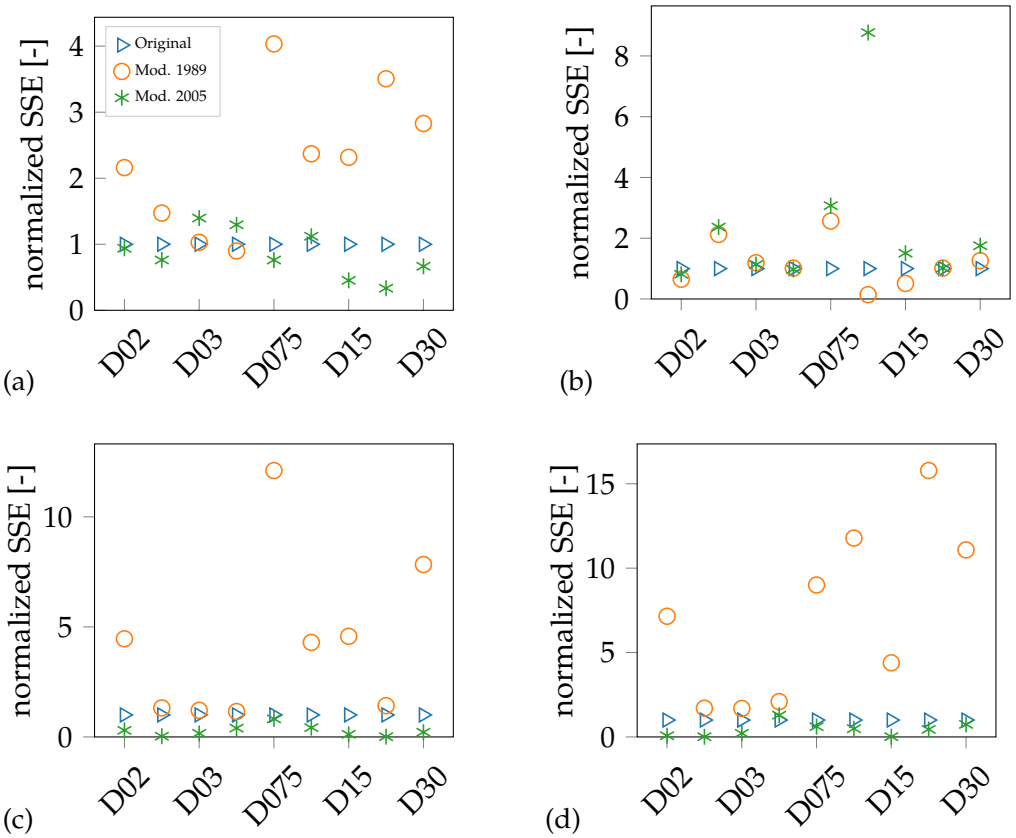

Figure 4.21: SSE of the EDC modifications using GRI-3.0 normalized by the SSE of the original version at radial and axial profiles for (a) temperature, (b) CH_4 (c) CO and (d) NO

4.3.4 Detailed chemical mechanism

Simulation results for Flame D using a detailed chemical mechanism, namely the GRI-3.0, are shown and discussed here. The simulation was conducted with the detailed chemical mechanism using direct integration for the set of ODEs describing the fine structures, compare section 2.2.8. Additionally, a simulation using Strang splitting for the ODE was carried out. This was defined the most promising operator splitting method for the EDC by the tests described in section 4.1. As a last option the simulation was conducted using operator splitting in combination with ISAT. The ISAT retrieval tolerance was set to 10^{-4} and 10^{-6}, respectively.

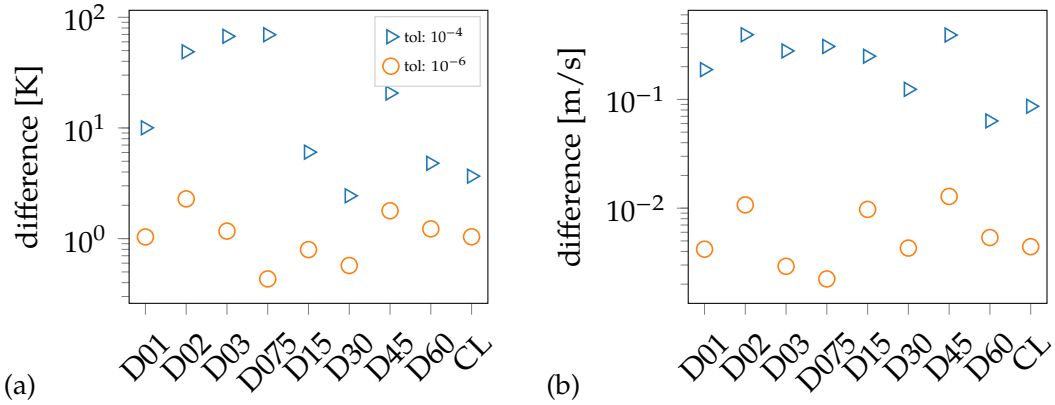

Figure 4.22: Absolute difference between Operator Splitting without and with ISAT at different profiles for a retrieval tolerance of 10^{-4} and 10^{-6} respectively for (a) temperature and (b) velocity

Figure 4.22 shows the average difference of temperature and velocity between operator splitting with ISAT and without ISAT at radial and axial profiles. The deviation between pure operator splitting and operator splitting with ISAT becomes obviously higher, when a bigger tolerance is used (here 10^{-4}). There is hardly any difference between operator splitting with ISAT using a tolerance of 10^{-6} and operator splitting without ISAT. This result ensures, that the implemented ISAT is working and approximates the solution. The computational time increases, when using a smaller tolerance, because less retrievals can be conducted and chemistry has to be integrated more often (Table 4.2). Even if ISAT is used with a tolerance of 10^{-6} the computational time can be reduced compared to operator splitting without ISAT. For this case the reduction was 26.3 hours and 58% respectively. In the following figures the results obtained by ISAT using a tolerance value of 10^{-6} are not plotted, since they are nearly identical to the operator splitting without ISAT and do not provide any additional information.

Figure 4.23 shows axial profiles of temperature, velocity and species concen-

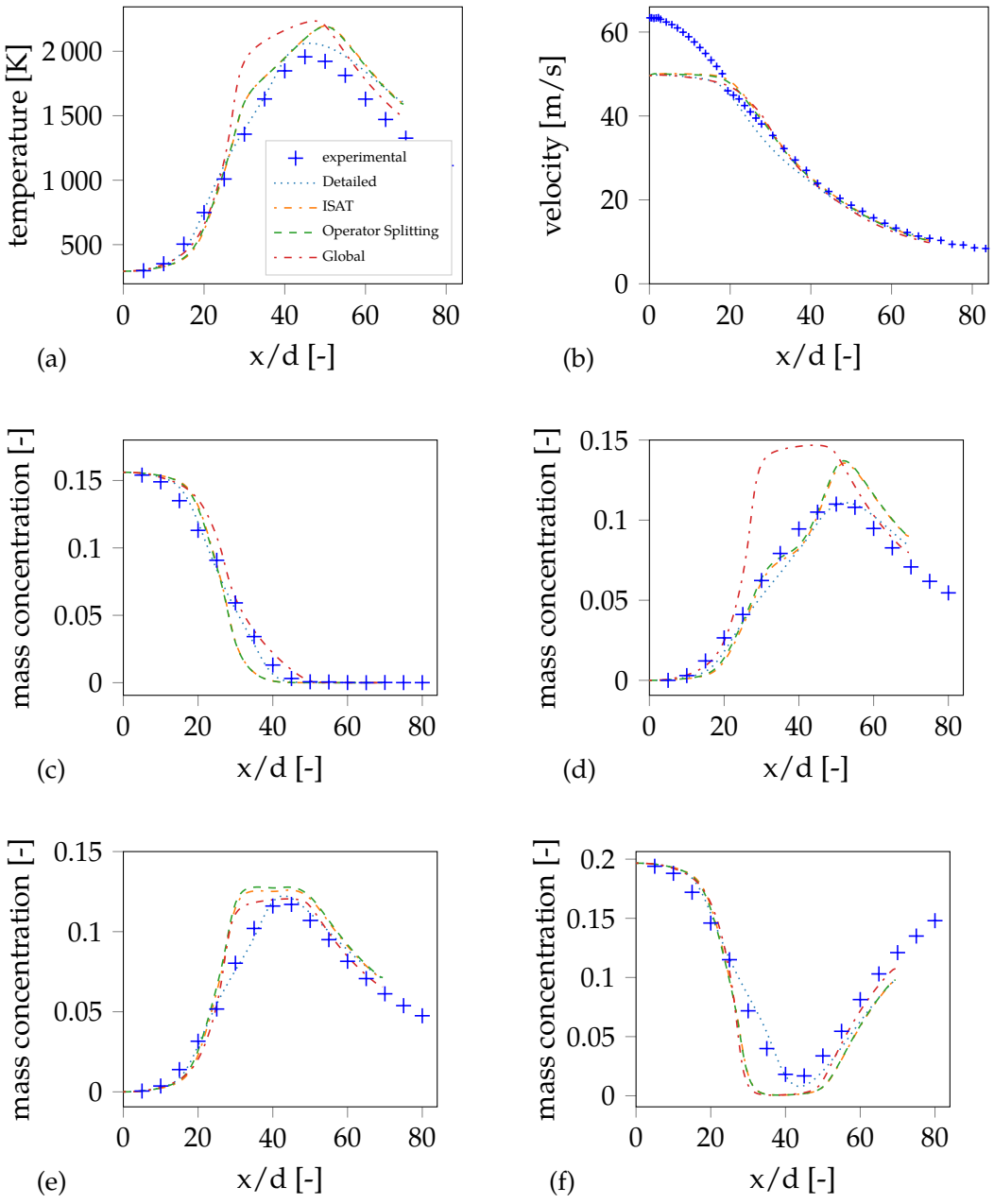

Figure 4.23: Axial profiles at the centerline comparing different methods using GRI-3.0 and a global mechanism (a) temperature, (b) velocity and species mass concentrations (c) CH_4 (d) CO_2 (e) H_2O (f) O_2

Table 4.2: Execution time for different settings for Flame D simulation with GRI-3.0 on VSC3 using 96 cores

simulation settings	execution time [h]
Direct Integration	15.3
Operator Splitting without ISAT	45.5
Operator Splitting with ISAT (tol:10^{-4})	11.8
Operator Splitting with ISAT (tol:10^{-6})	19.2

tration for CH_4, CO_2, H_2O and O_2 obtained by the simulations. The different simulation settings using GRI-3.0 are compared with the results from the global mechanism and measurement data. The computations employing direct integration and the GRI-3.0 show the best agreement with the measurement data for the axial profiles. The concentration and temperature profiles are smoother, compared to the simulation with the global mechanism, when calculated with operator splitting, more like the experimental data. The temperature curve is smooth and the maximum temperature at the centerline is only slightly over predicted. The other axial profiles obtained from the simulation using GRI-3.0 with direct integration fit best to the measurement data (Figure A.26 to Figure A.33 in the appendix).

Unfortunately, using operator splitting and ISAT does not give the same, or as good results, as using direct integration. However, there is an improvement compared to the simulation using the global mechanism. The temperature profile fits better and also the maximum temperature approximates the experiment slightly better. The CO_2 concentration is depicted way better at the centerline by operator splitting or operator splitting with ISAT than by the global mechanism.

The GRI-3.0 mechanism consists of 53 species and 325 reactions. These include also radical species , such as CO, OH, or NO. The concentration of CO is predicted very well by the detailed mechanism (Figure 4.24(d) and Figure A.37(a)). The simulation with operator splitting (with and without ISAT) over estimates the CO concentration at these positions in the flame. The NO concentration is over predicted by all the methods, but less when using direct integration. It has to be stated though, that the concentrations are very low here and therefore the absolute differences in the predictions are not high. At least the profile, the position of the peak of the concentration respectively, can be predicted. It seems that the OH concentration is depicted even better by the simulation with operator splitting than by direct integration. Figures A.34 to A.37 show the radial profiles, which have a similar trend as the once at the centerline.

To substantiate the conclusions drawn from the temperature, velocity and concentration profiles, the SSE was calculated for temperature, velocity, CH_4 and NO concentration. Figure 4.25 shows the results and confirms that using the detailed mechanism, GRI-3.0, with direct integration gives the best results under all inves-

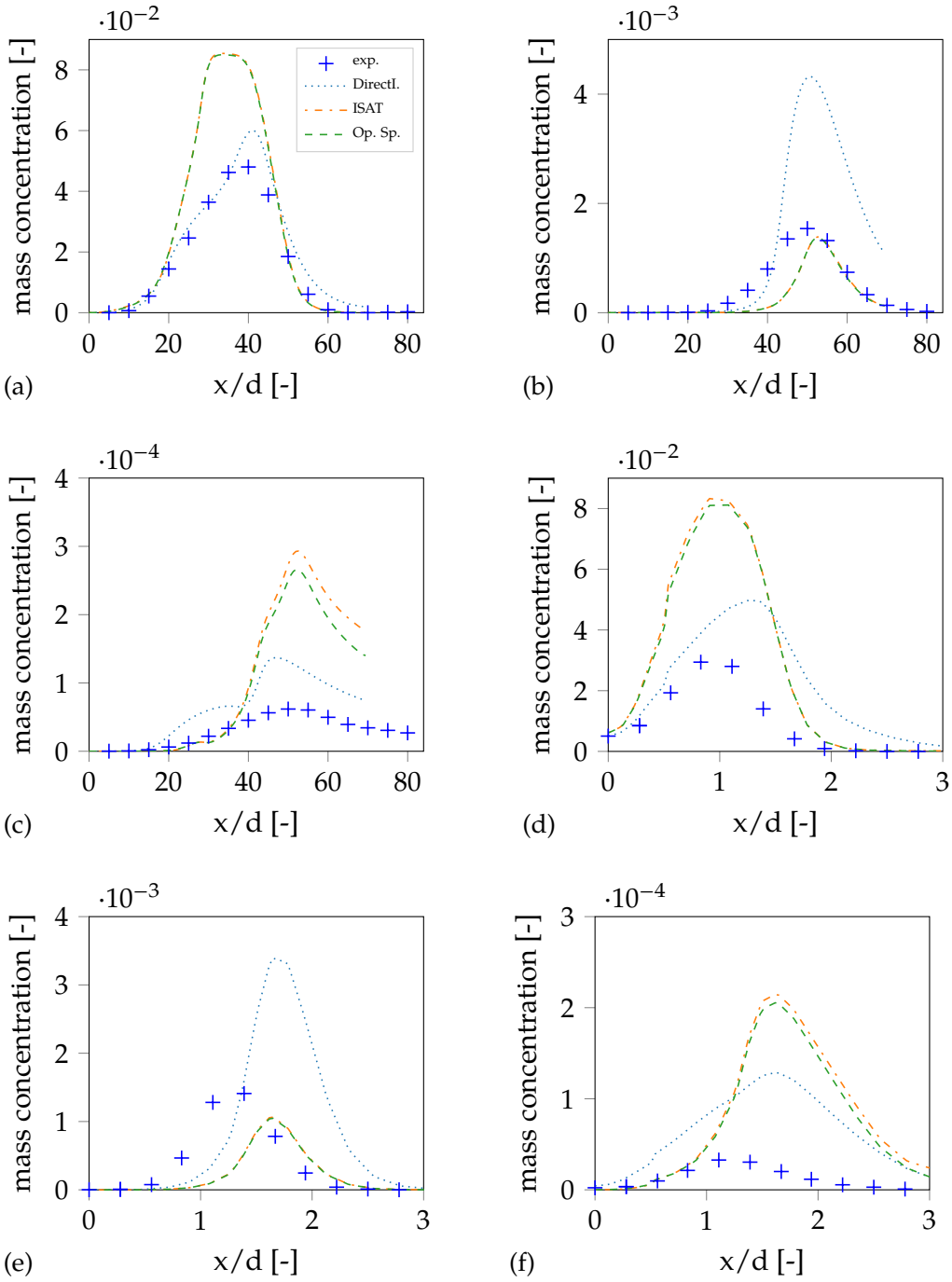

Figure 4.24: Radical species calculated using different methods with GRI- 3.0: axial profiles at the centerline for (a) CO, (b) OH and (c) NO and radial profiles at x/d=15 (d) CO, (e) OH and (f) NO

tigated possibilities. Furthermore, the figure shows that operator splitting with or without ISAT generally gives better results than the global mechanism, not even considering that with a global mechanism radical species can not be predicted.

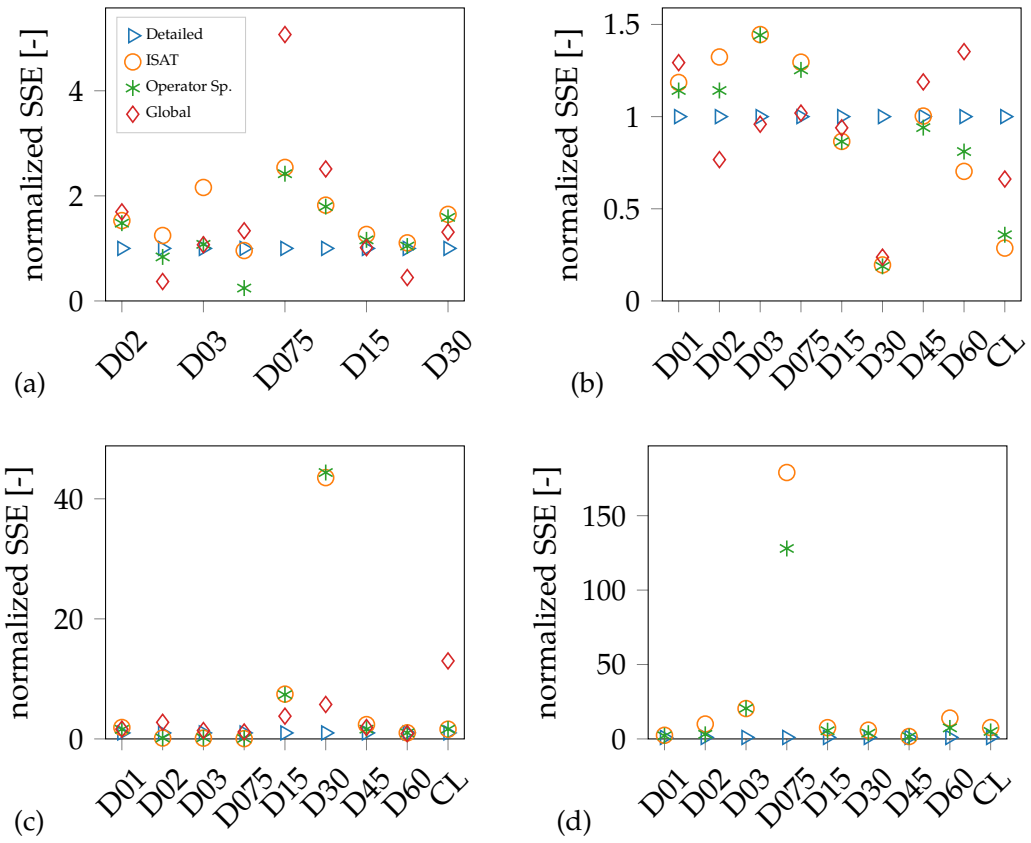

Figure 4.25: SSE between experimental data and different simulations carried out at radial and axial profiles for (a) temperature, (b) velocity, (c) CH_4 and (d) NO

The execution time of the different simulations were already discussed shortly at the beginning in conjunction with the ISAT-tolerance. Table 4.2 shows the execution time for the conducted simulations and reveals that the speed up of the different approaches compared to direct integration is not very promising. Only the simulation with operator splitting and ISAT with the big tolerance is faster than the direct integration. When using ISAT with the smaller tolerance, the simulation time is quite close to direct integration, but operator splitting without ISAT takes nearly three times longer than the direct integration.

One benefit, which could not be quantified yet and has not been studied extensively enough is that the usage of operator splitting shows an improvement for the stability of the simulations. Problems occurred with the simulations using direct

integration: sometimes no proper ignition took place, depending on the used grid. Temperatures overshot in the beginning, but approached a steady-state afterwards. Finally, there might be more benefits with the usage of operator splitting than can be presented here. The computational time might still be improved by further investigations.

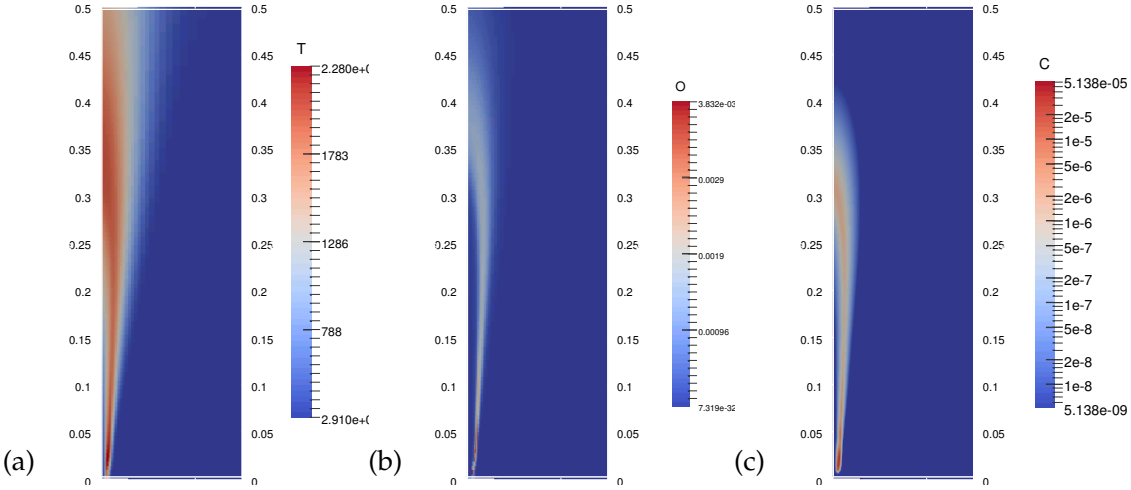

Figure 4.26: Flame D simulated with GRI-3.0 and direct integration (a) temperature (b) O radical mass concentration and (c) C radical mass concentration

Figure 4.26 shows the whole flame simulated with a detailed chemical mechanism. The temperature, the O and C radical concentrations are shown there as representative quantities. The visible flame length of Flame D is approximately 48 cm (67 d), (Barlow and Frank 2007). The C and O radicals are substances which are responsible for the visibility of the flame. Figure 4.26 shows, that the concentration profiles agree approximately with the given flame length reported by Barlow and Frank (2007).

4.3.5 Chemical time scales

The chemical time scales presented in section 2.4, or more concrete the promising ones revealed by the tests from section 4.2, are here used to calculate the chemical time scale and the turbulent Damköhler number for Flame D. As already mentioned in section 3.2, the chemical time scales were implemented as a post processing tool in OpenFOAM. This tool was used to calculate the time scales for the flame simulated with the global mechanism and with the detailed mechanism at steady state, i.e. here at the end of the simulation at 0.5 seconds.

Figure 4.27 shows the chemical time scales on the grid. The grey areas depict the places where the time scale is above or below the range shown. This was

done, because the chemical time scale was set to a default value of 10^{15}, when the calculation was not possible. This was often the case outside of the reaction zone.

Overall, the profiles of the chemical time scale look reasonable, but it is hard to say if the prediction is correct, since a chemical time scale can not be measured. Figure 4.27 shows, that the same methods for the chemical time scale calculation do not give the same results when they are applied to the simulation conducted with the global or the detailed chemical mechanism, respectively. It is evident that the results are different, since radical species play an important role. Therefore, they also contribute to the chemical time scale calculations.

For IJTS and IJTSsimple the results are at least in the same range or order of magnitude. This is definitely not the case for Ren's and Ren's product method. When applying them to the simulation with GRI-3.0 the highest and smallest calculated time scales vary by several orders of magnitude. The LOI and the SPTS method also show quite different results for the different simulations.

Since the chemical time scales can not be compared with measurement data, the turbulent Damköhler number was calculated. Its values can be checked for plausibility. The turbulent Damköhler number is defined as the relation of a mixing time scale to a chemical time scale (equation 3.10). Therefore, the turbulent Damköhler number shows if the reaction is controlled by mixing or by chemical reactions. Sandia Flame D is a turbulent flame, having a jet Reynolds number of approximately 22400. This means that the reaction process is mainly mixing controlled. In low oxygen regions, e.g. in between the two reaction zones, the chemical time scale increases due to a lack of reactants and Damköhler decreases since the mixing time scale is not affected by oxygen.

Figure 4.28 shows the turbulent Damköhler numbers obtained by the different chemical time scale definitions for the simulations employing the global and the detailed chemical mechanism, respectively. Apparently, IJTSsimple does not give valid results for either simulation - the Damköhler values are significantly too low. Ren's product time scale fails to predict a reasonable Damköhler number for the global mechanism. The LOI method fails to predict a plausible time scale for the detailed mechanism. Ren's definition gives a good profile with slightly too low values when using a global mechanism.

The best predictions for the simulation with GRI-3.0 are obtained when using SPTS, Ren's or Ren's product method. The maximum turbulent Damköhler number is for all in the range of 10^5 and, therefore, obviously strongly mixing controlled. For the region lacking of oxygen, and consequently slower reactions, the Damköhler number approaches lower values when using these three methods. SPTS gives even for the simulation with the global mechanism similar results. Concluding, those three methods are the most promising for calculating the modified constants for the EDC as suggested by Bao (2017) and Parente et al. (2015), see sections 2.2.6 and 2.2.7.

To support the argumentation for the values of the turbulent Damköhler number,

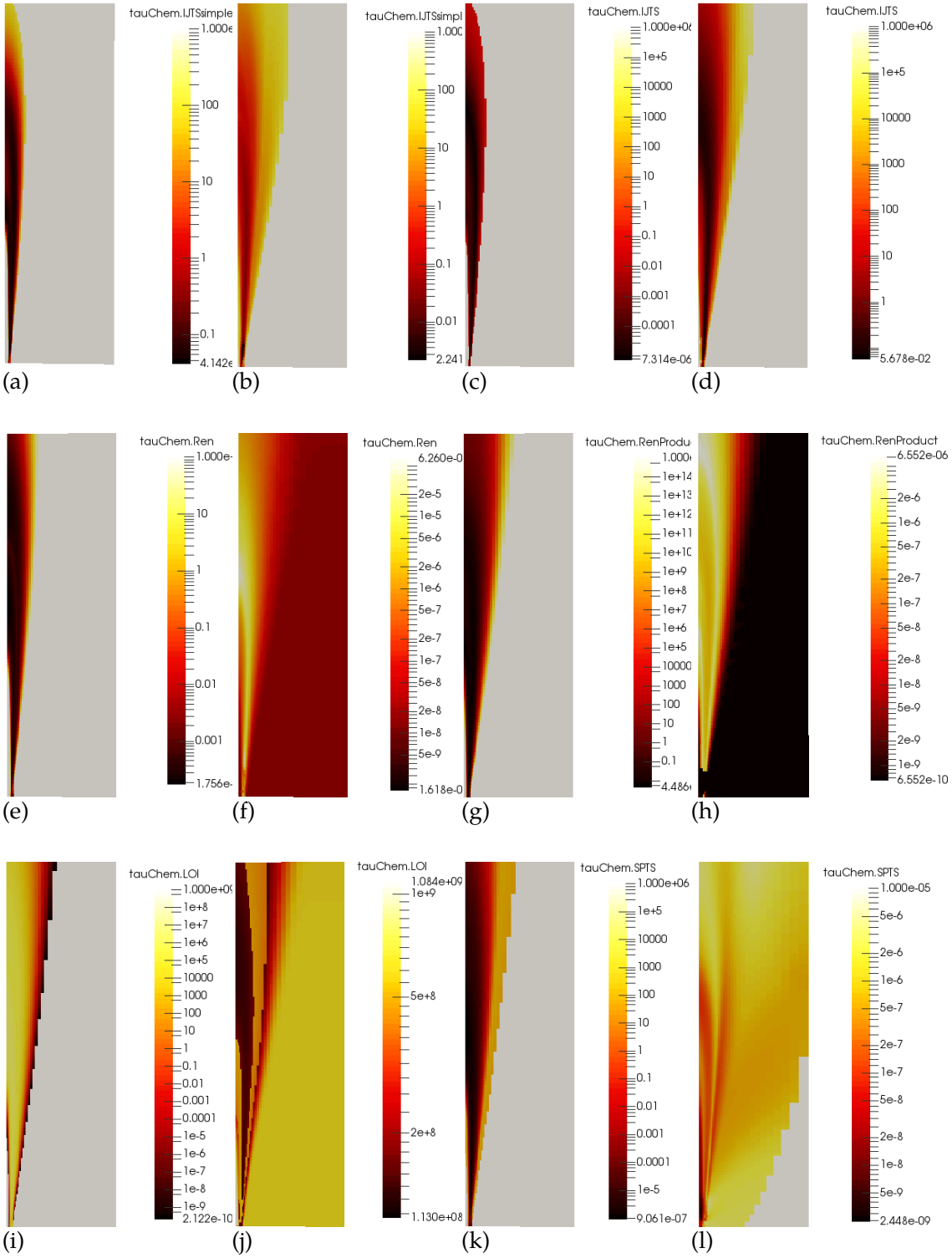

Figure 4.27: Chemical time scales for Flame D simulated with global and detailed mechanism respectively: (a) (b) IJTSsimple, (c) (d) IJTS,(e) (f) Ren, (g) (h) RenProduct, (i) (j) LOI, (k) (l) SPTS

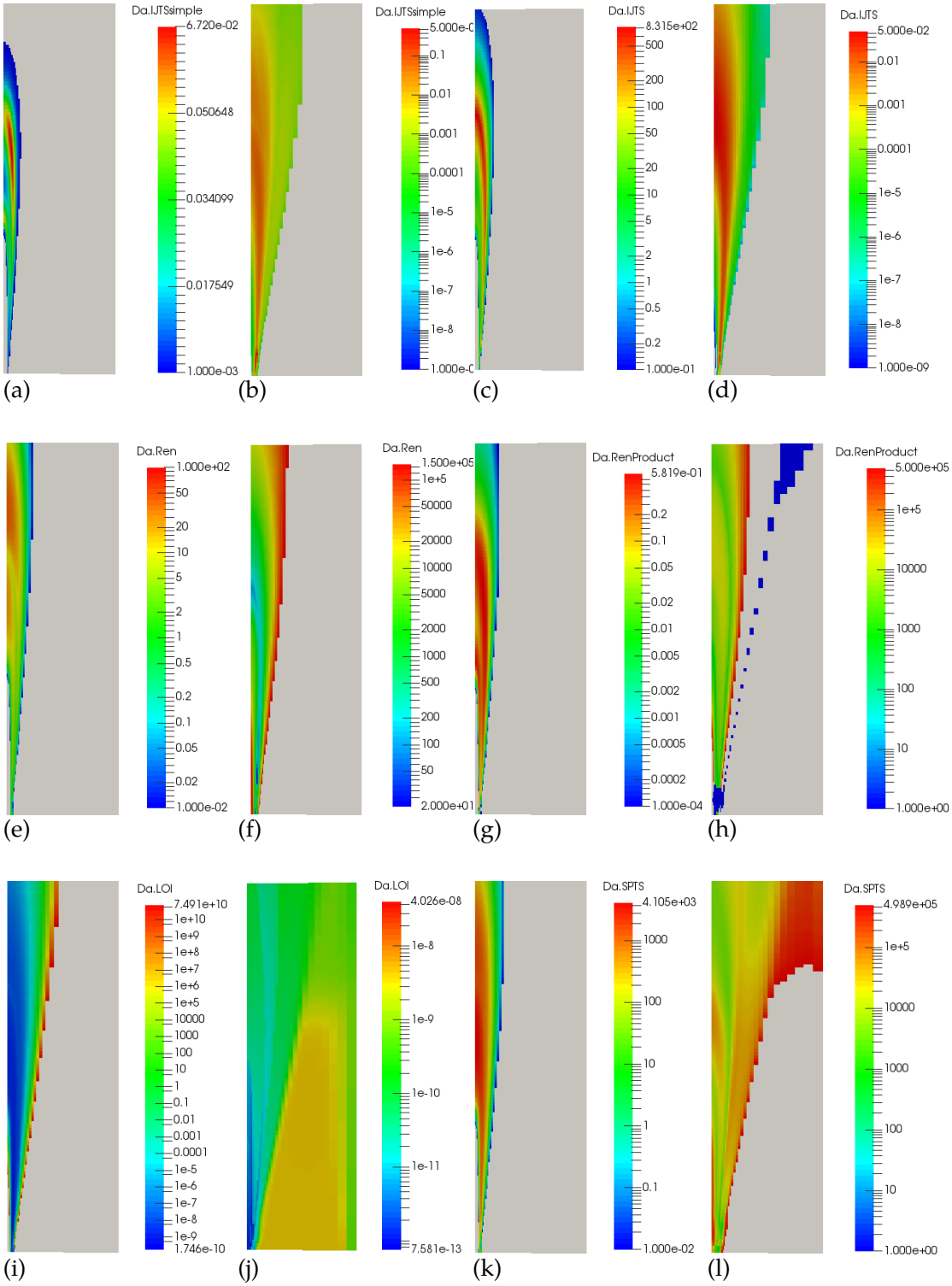

Figure 4.28: Turbulent Damköhler number for Flame D simulated with global and detailed mechanism respectively: (a) (b) IJTSsimple, (c) (d) IJTS,(e) (f) Ren, (g) (h) RenProduct, (i) (j) LOI, (k) (l) SPTS

the Damköhler number computed by Ren's Product time scale and SPTS was plotted at the axial positions x/d=15 and x/d=30. The oxygen concentration and the OH concentration were added to support the above findings. As discussed in section 4.2.3, the Damköhler number should have an "W"-like profile at those positions in the flame. Figure 4.29 shows this profile as expected. This supports the finding, that Ren's product method and SPTS are suitable methods to compute the chemical time scale.

Furthermore, Figure 4.29 shows that the Damköhler number decreases, with a decreasing oxygen concentration and increases, when the concentration increases again. The higher Damköhler number at approximately r/d=2 might be explained by a higher concentration of OH or other radical species there and, therefore, higher reactivity leading to a decrease of the chemical time scale. The prediction of the turbulent Damköhler number calculated with SPTS at x/d=30 differs a bit from the expected profile.

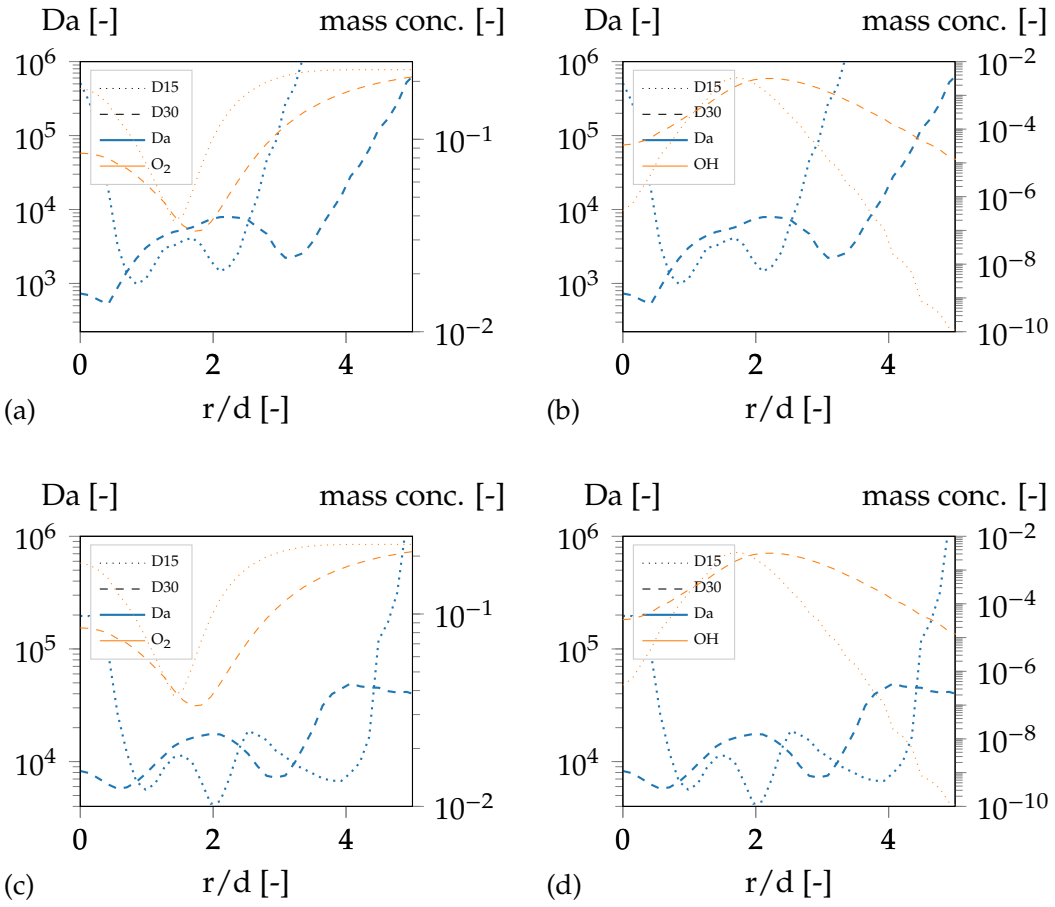

Figure 4.29: Radial profile of the Damköhler number at x/d=15 and x/d=30 plot with the oxygen and OH mass concentration by (a) (b) RenProduct and (c) (d) SPTS

5 Conclusion and Outlook

The presented work shows, that the used EDC-solver can predict the behavior of turbulent premixed flames well. The tests on different turbulence models reveal the best fit for Sandia Flame D to be the standard k-ϵ model with its standard coefficients. As a consequence, the standard k-ϵ model should be used in conjunction with this EDC solver - at least for similar cases. It should be tested if this turbulence model also fits best for other test cases. Others have also decided to use LES, e.g. Zahirović et al. (2010) or Lysenko et al. (2014a), in combination with the EDC. Further investigations could be carried out, using LES in OpenFOAM. Although it is believed that the increased computational demand is not worth the higher resolution.

It has been shown that the influence of the EDC formulation, i.e. the different versions used, does hardly have an influence when using a global chemical mechanism for Flame D. In contrast, when a detailed chemical mechanism is used, the different versions deliver quite different predictions for temperature, velocity and species concentrations. It was decided to use the original EDC formulation for the final simulations, since it fitted best for most cases under investigation. The formulation from Magnussen (1989a) gave the biggest deviations compared to the experimental data when using the GRI-3.0 mechanism. The original formulation of the EDC is based on physical observations and the modifications have been suggested to overcome inaccurate predictions, e.g. in the tail of the flame. Apparently, the original EDC version fits quite well here and, therefore, the way to go should be to use modifications based on physical relations. The EDC constant modifications from Parente et al. (2015) or Bao (2017) might be used, when applying the EDC to different combustion regimes.

The temperature is over predicted using the global mechanism by more than 100 K. Moreover, the predictions of radical species or other intermediate species are not considered in a global mechanism, but they can provide a lot of additional information. Sometimes, the knowledge of NO_x concentration can be the main objective. Then it is inevitable to use a detailed mechanism, since a global mechanism can not predict this. Although, using a detailed chemical mechanism, here the GRI-3.0, requires more computational power and consequently increases simulation time, it brings major improvements in the accuracy of the predictions.

One major goal, finding a proper operator splitting method for the application with the EDC was achieved. The Strang splitting is working stable within the OpenFOAM solver and gives proper predictions, although loosing some accuracy compared to direct integration. Unfortunately, using operator splitting only, is

not giving any speed up right now. Further improvements might reduce the computational cost.

Additionally, the usage of operator splitting enabled the application of ISAT. This gives some speed-up compared to direct integration, if the look-up tolerance is chosen properly. The computational time could also be reduced, when already existing tables are used for similar simulations instead of building up the ISAT table new for each run. The simulations with operator splitting and ISAT showed similar results as the ones without ISAT, i.e. a bit less accurate than from direct integration. However, radical species can be predicted and the predictions of the main components fit better than those from the global mechanism.

Furthermore, it was observed that the simulations with operator splitting are more stable than the ones with direct integration. Sometimes no ignition took place when using direct integration and certain settings. This effect could not be quantified within this thesis, but it reveals that there might be more benefit when using operator splitting than just possible calculation speed-up.

Finally, the other major goal of this thesis was to find a suitable and applicable chemical time scale definition for the calculation of modified EDC constants. Ren's, Ren's product and the SPTS have been identified as the most promising time scale definitions and can be applied for the modification of the EDC model constants (C_γ and C_τ). The next step is to apply those modifications to simulations. The groundwork has been laid in this thesis with the revelation of a quite simple and proper chemical time scale definition. In future simulations comparing those modifications with MILD combustion flames should show the applicability of the concept and hopefully an improvement compared to the standard EDC.

List of Figures

List of Tables

List of Symbols

Symbol	Unit	Description
C_η	–	constant in turbulence modeling
k_t	$W\,K^{-1}\,m$	thermal diffusivity
c_p	$J\,kg^{-1}\,K^{-1}$	specific heat at constant pressure
Pr	–	Prandtl number
x	–	coordinate in x-direction
y	–	coordinate in y-direction
z	–	coordinate in z-direction
μ	Pa s	dynamic viscosity
S_{ij}	–	mean strain tensor
δ_{ij}	–	kronecker delta
$C_{\varepsilon 1}$	–	constant
$C_{\varepsilon 2}$	–	constant
$C_{\varepsilon 3}$	–	constant
C_1	–	constant
w	–	transfer of energy
ω	s^{-1}	vorticity or strain rate
ξ	–	numerical constant
u	$m\,s^{-1}$	characteristic velocity
L	m	characteristic length
ν	$m^2\,s^{-1}$	kinematic viscosity
ϵ	$m^2 s^{-3}$	rate of dissipation
$\hat{q}$	$m^2 s^{-3}$	energy dissipation
η	m	Kolmogorov length scale
γ	–	mass fraction
k	$m^2\,s^{-2}$	turbulent kinetic energy
$\dot{m}$	s^{-1}	transfer of mass
τ	s	residence time
C_γ	–	EDC model constant
C_τ	–	EDC model constant
C_{D1}	–	EDC model constant
C_{D2}	–	EDC model constant
Re	–	Reynolds number

Symbol	Unit	Description
Da	–	Damköhler number
R	$kg/m^3/s$	mass transfer rate
χ	–	fraction of reacting fine structures
c	kg/m^3	concentration
ρ	kg/m^3	density
κ	–	stoichiometric oxygen requirement
S	m/s	flame speed
q	$kg/m^3/s$	heat transfer
h	J/kg	enthalpy
p	Pa	pressure
a	–	stoichiometric coefficient
T	K	Temperature
U	–	function
A	–	matrix
B	–	matrix
Y	–	mass fraction
t	s	time
$\dot{\omega}$	–	function
λ	–	eigenvalue
$\mathcal{J}$	–	Jacobian matrix
V	–	matrix of eigenvectors
Λ	–	matrix with eigenvalues in diagonal
E	–	solution of the ODE
X	–	mass fraction
n_s	–	number of species
ε	–	boundary value
$\hat{\gamma}$	–	weight factor
P	–	number of real eigenvalues
l	–	number of complex eigenvalues
r	$kmol/m^3/s$	reaction rate
v	–	stoichiometric coefficient
e_i	–	canonical basis vector
S^c	–	sensitivity parameter
LOI	–	level of importance factor
c_{che}	–	constant
W	g/mol	molecular mass
s	mol/cm^3	source term
A_{Arr}	–	pre-exponential factor
E_{Arr}	J/mol	activation energy
R_{gas}	J/mol/K	ideal gas constant

Symbol	Unit	Description
Q	K	heat of reaction
Error	–	error
GCI	–	grid convergence index
ζ	–	difference between grid solutions
Ψ	–	refinement ratio
N	–	order
m	–	length of cell
θ	–	solution
f	–	function
S_ϵ	kgms^{-3}	source term
$U^{(\star)}$	$\mathrm{rad\,s}^{-1}$	
Ω_{ij}	$\mathrm{rad\,s}^{-1}$	mean rotation rate
A_0	–	constant
A_s	–	constant
ω_k	$\mathrm{rad\,s}^{-1}$	angular velocity
K	–	safety factor for grid convergence index

Sub-/Superscript	Description
$*$	fine structures
$\circ$	surroundings
$'$	level in energy cascade
$\bar{}$	mean cell value
fu	fuel
pr	product
ox	oxidant
turb	turbulent
lam	laminar
che	chemical
flow	flow
i	species
j	species
J	relevant species
$\tilde{}$	new basis
a	sorted values
d	reaction
e	value at $t_0 + dt$
0	value at t_0
min	minimum value
R	Reaction
ext	extinction

Sub-/Superscript	Description
end	value at the end
α	part of function
β	part of function
I	time
mix	mixing
max	maximum
DI	direct integration
OS	operator splitting
n	time level
L	fine structure region

List of Acronyms

CFD computational fluid dynamics

CPU central processing unit

CSP computational singular perturbation

CSR continously stirred reactor

CTS-ID characteristics time scale identification

DNS direct numerical simulation

EDC eddy dissipation concept

EVTS eigenvalue time scale

GCI grid convergence index

HR homogenous reactor

IJTS inverse jacobian time scale

ISAT in-situ adaptive tabulation

LES large eddy simulation

LOI level of importance

MDID main direction identification

MILD moderate or intense low-oxygen dilution

ODE ordinary differential equation

PDE partial differential equation

PFR plug flow reactor

PISO pressure implicit with splitting of operator

POX partial oxidation

PVA principal variable analysis

PVTS progress variable time scale

RANS reynolds averaged navier-stokes equations

SIMPLE semi implicit method for pressure-linked equations

SPTS system progress time scale

SSE sum of squared errors

SWSS symmetrically weighted sequential splitting

References

Anderson, E. et al. (1999). *LAPACK Users' Guide*. third. Philadelphie, PA: Society for Industrial and Applied Mathematics.

Bao, H. (2017). "Development and Validation of a New Eddy Dissipation Concept (EDC) Model for MILD Combustion". PhD thesis. Delft University of Technology.

Barlow, R. S. and Frank, J. H. (1998). "Effects of turbulence on specific mass fractions in methane/air jet flames". In: *Twenty-Seventh Symposium (International) on Combustion* 27, pp. 1087–1095.

Barlow, R. S. et al. (2005). "Piloted methane/air jet flames: Transport effects and aspects of scalar structure". In: *Combustion and Flame* 143.4, pp. 433–449. DOI: 10.1016/j.combustflame.2005.08.017.

Barlow, R. and Frank, J. (2007). "Piloted CH4/Air Flames C, D, E, and F - Release 2.1". In: June, pp. 1–12.

Boussinesq, J. (1877). "Essai Sur La Théorie Des Eaux Courantes". In: *Mem. Présentés Acad. Sci.* 23.

Brodtkorb, P. A. (2017). *numdifftools 0.9.20*.

Buffoni, M. and Willcox, K. (2010). "Projection-based model reduction for reacting flows". In: *40th Fluid Dynamics Conference and Exhibit* July, pp. 1–14. DOI: 10.2514/6.2010-5008.

Byggstoyl, S. and Magnussen, B. (1983). "A model for flame extinction in turbulent flow". In: *Fourth Symposium on Turbulent Shear Flows* 4, pp. 32–38. DOI: 10.1007/978-3-642-69996-2_31.

Caudal, J. et al. (2013). "Characteristic chemical time scales identification in reactive flows". In: *Proceedings of the Combustion Institute* 34.1, pp. 1357–1364. DOI: 10.1016/j.proci.2012.06.178.

Celik, I. B. et al. (2008). "Procedure for Estimation and Reporting of Uncertainty Due to Discretization in CFD Applications". In: *Journal of Fluids Engineering* 130.7, p. 78001. DOI: 10.1115/1.2960953.

Chen, J. Y. et al. (1999). "Joint Scalar PDF Simulation of Turbulent Reacting Flows with Detailed Chemistry on a Parallel Cluster". In: *Proceedings of the Fourth International Workshop on Measurement and Computation of Turbulent Nonpremixed Flames*.

Christo, F. C. and Dally, B. B. (2005). "Modeling turbulent reacting jets issuing into a hot and diluted coflow". In: *Combustion and Flame* 142.1-2, pp. 117–129. DOI: 10.1016/j.combustflame.2005.03.002.

Damköhler, G. (1940). "Der Einfluss der Turbulenz auf die Flammengeschwindigkeit in Gasgemschen". In: *Zeitschrift für Elektrochemie und angewandte physikalische Chemie* 46.11, pp. 601–652. DOI: 10.1002/bbpc.19400461102.

D'Errico, J. (2006). *Adaptive Robust Numerical Differentiation*.

Duarte, M. and Massot, M. (2015). "Operator splitting methods with error estimator and adaptive time-stepping . Application to the simulation of combustion phenomena". In: *operator splitting and alternating direction methods*, pp. 1–13.

Evans, M. J. et al. (2015). "Modeling Lifted Jet Flames in a Heated Coflow using an Optimized Eddy Dissipation Concept Model". In: *Combustion Science and Technology* 187.7, pp. 1093–1109. DOI: 10.1080/00102202.2014.1002836.

Geiser, J. and Gedicke, J. (2008). "Iterative operator-splitting methods with higher-order time integration methods and applications for parabolic partial differential equations". In: *J. Comput. Appl. Math.* 217, pp. 227–242.

Goodwin, D. G. and Speth, R. L. (2017). *Cantera: An Object-oriented Software Toolkit for Chemical Kinetics, Thermodynamics, and Transport Processes Version 2.3.0*. DOI: 10.5281/zenodo.170284.

Gran, I. R. and Magnussen, B. F. (1996b). "A Numerical Study of a Bluff-Body Stabilized Diffusion Flame . Part 2 . Influence of Combustion Modeling And Finite-Rate Chemistry". In: *Combustion Science and Technology* 119, pp. 191–217. DOI: 10.1080/00102209608951999.

Isaac, B. b. et al. (2013). "A novel methodology for chemical time scale evaluation with detailed chemical reaction kinetics". In: *Energy and Fuels* 27.4, pp. 2255–2265. DOI: 10.1021/ef301961x.

Issa, R. (1986). "Solution of the implicitly discretised fluid flow equations by operator-splitting". In: *Journal of Computational Physics* 1. DOI: 10.1016/0021-9991(86)90099-9.

Jones, E. et al. (2001). *SciPy: Open source scientific tools for Python*.

Jones, W. P. and Launder, B. E. (1972). "The prediction of laminarization with a two-equation model of turbulence". In: *Int. J. Heat Mass Transfer* 15, pp. 301–314.

Kazakov, A. and Frenklach, M. (2017). *Reduced Reaction Sets based on GRI-Mech 1.2*.

Kolmogorov, A. N. (1890). "The local structure of turbulence in incompressible viscous fluid for very large Reynolds numbers". In: *Proceedings: Mathematical and Physical Sciences* 434.

Lam, S. H. and Goussis, D. A. (1991). "conventional asymptotics and computational singular perturbation for simplified kinetics modelling". In: *Reduced Kinetic Mechanisms and Asymptotic Approximations for Methane-Air Flames*. Springer Verlag.

Launder, B. E. and Spalding, D. B. (1974). "The numerical computation of turbulent flows". In: 3, pp. 269–289. DOI: https://doi.org/10.1016/0045-7825(74)90029-2.

Li, X. et al. (2017a). "Characteristic chemical time scale analysis of a partial oxidation flame in hot syngas coflow". In: *Energy Fuels* 31, pp. 4382–4390. DOI: 10.1021/acs.energyfuels.6b02490.

Li, Z. et al. (2017b). "Edcsmoke: A new combustion solver for stiff chemistry based on OpenFOAM®". In: *AIP Conference Proceedings* 1863, pp. 17–21. DOI: 10.1063/1.4992364.

Lilleberg, B. et al. (2013). "Numerical simulation with an extinction database for use with the eddy dissipation concept for turbulent combustion". In: *Flow, Turbulence and Combustion* 91.2, pp. 319–346. DOI: 10.1007/s10494-013-9463-y.

Løvås, T. et al. (2002). "Development of adaptive kinetics for application in combustion systems". In: *Proceedings of the Combustion Institute* 29, pp. 1403–1410.

Lysenko, D. A. et al. (2014a). "Numerical simulation of non-premixed turbulent combustion using the eddy dissipation concept and comparing with the steady laminar flamelet model". In: *Flow, Turbulence and Combustion* 93.4, pp. 577–605. DOI: 10.1007/s10494-014-9551-7.

Lysenko, D. A. et al. (2014b). "Numerical simulations of the Sandia Flame D using the eddy dissipation concept". In: *Flow, Turbulence and Combustion* 93.4, pp. 665–687. DOI: 10.1007/s10494-014-9561-5.

MacNamara, S. and Strang, G. (2009). *Operator Splitting*, pp. 1–21.

Magnussen, B. F. (1975). "An Investigation into the behavior of soot in a turbulent free jet C2H2-Flame". In: *Syposium (International) on Combustion* 15, pp. 1415–1425. DOI: https://doi.org/10.1016/S0082-0784(75)80400-0.

Magnussen, B. (1981). "On the structure of turbulence and a generalized eddy dissipation concept for chemical reaction in turbulent flow". In: p. 6.

Magnussen, B. (1989a). "Modeling of NOx and Soot Formation by the Eddy Dissipation Concept". In: *Internationl Flame Research Foundation*.

Magnussen, B. (2005). "The Eddy Dissipation Concept a Bridge between science and technology". In: *ECCOMAS Thematic Conference on Computational Combustion*.

Mardani, A. (2017). "Optimization of the Eddy Dissipation Concept (EDC) model for turbulence-chemistry interactions under hot diluted combustion of CH4/H2". In: *Fuel* 191, pp. 114–129. DOI: 10.1016/j.fuel.2016.11.056.

Masri, A. R. et al. (1996). "The Structure of turbulent nonpremixed Flames revealed by Raman-Rayleigh-LIF Measurements". In: 22, pp. 307–362. DOI: https://doi.org/10.1016/S0360-1285(96)00009-3.

Parente, A. et al. (2015). "Extension of the Eddy Dissipation Concept for turbulence / chemistry interactions to MILD combustion". In: *FUEL* 163, pp. 98–111. DOI: 10.1016/j.fuel.2015.09.020.

Patankar, S. and Spalding, D. B. (1972). "A calculation procedure for heat, mass and momentum transfer in three-dimensional parabolic flows". In: *International Journal of Heat and Mass Transfer* 15.10, pp. 1787–1806.

Pope, S. B. (1997). "Computationally efficient implementation of combustion chemistry using in situ adaptive tabulation". In: *Combustion Theory and Modelling* 7830.1, pp. 41–63. DOI: 10.1088/1364-7830/1/1/006.

Pope, S. B. (2000). *Turbulent Flows*. Cambridge: Cambridge University Press.

Prüfert, U. et al. (2014). "The analysis of chemical time scales in a partial oxidation flame". In: *Combustion and Flame* 161.2, pp. 416–426. DOI: 10.1016/j.combustflame.2013.09.001.

Rehm, M. (2010). "Numerische Strömungssimulation der Hochdruckvergasung unter Berücksichtigung detaillierter Reaktionsmechanismen". PhD thesis.

Ren, Z. and Goldin, G. M. (2011). "An efficient time scale model with tabulation of chemical equilibrium". In: *Combustion and Flame* 158.10, pp. 1977–1979. DOI: 10.1016/j.combustflame.2011.02.018.

Ren, Z. and Pope, S. B. (2008). "Second-order splitting schemes for a class of reactive systems". In: *Journal of Computational Physics* 227.17, pp. 8165–8176. DOI: 10.1016/j.jcp.2008.05.019.

Roache, P. J. (1994). *Perspective: A Method for Uniform Reporting of Grid Refinement Studies*. DOI: 10.1115/1.2910291.

Roekaerts, D. et al. (2000). "Note in preparation of a discussion on the role of turbulence model and inlet profiles in computations of piloted jet flame D". In: *Proceedings of the Fifth International Workshop on Measurement and Computation of Turbulent Nonpremixed Flames*.

Rossum, G. van (1995). *Python tutorial, Technical Report CS-R9526*.

Schneider, C. et al. (2003). "Flow field measurements of stable and locally extinguishing hydrocarbon-fuelled jet flames". In: *Combustion and Flame* 135.1-2, pp. 185–190. DOI: 10.1016/S0010-2180(03)00150-0.

Shih, T. H. et al. (1995a). "A new Reynolds stress algebraic equation model". In: *Computer Methods in Applied Mechanics and Engineering* 125.1-4, pp. 287–302. DOI: 10.1016/0045-7825(95)00796-4.

Shih, T.-H. et al. (1995b). "A new k-ϵ eddy viscosity model for high reynolds number turbulent flows". In: *Computers and Fluids* 24.3, pp. 227–238. DOI: 10.1016/0045-7930(94)00032-T.

Smith, G. P. et al. (2017). *GRI-MECH 3.0*.

Stefanidis, G. D. et al. (2006). "CFD simulations of steam cracking furnaces using detailed combustion mechanisms". In: *Computers and Chemical Engineering* 30.4, pp. 635–649. DOI: 10.1016/j.compchemeng.2005.11.010.

Strang, G. (1963). "Accurate partial difference methods I: Linear cauchy problems". In: *Archive for Rational Mechanics and Analysis* 12.1, pp. 392–402. DOI: 10.1007/BF00281235.

Strang, G. (1968). "On the Construction and Comparison of Difference Schemes". In: *SIAM Journal on Numerical Analysis* 5.3, pp. 506–517.

Tannehill, J. C. et al. (1984). *Computational Fluid Mechanics and Heat Transfer - Second Edition*.

Trotter, H. (1959). "On the Product of Semi-Groups of Operators". In: *Proceedings of the American Mathematical Society* 10.4, pp. 545–551.

Van der Walt, S. et al. (2011). "The NumPy Array: A Structure for Efficient Numerical Computation". In: *Computing in Science and Engineering* 13, pp. 22–30. DOI: DOI: 10.1109/MCSE.2011.37.

Wilcox, D. (1993). *Turbulence Modeling for CFD*. La Canada: DCW Industries.

Zahirović, S. et al. (2010). "Validation of flow simulation and gas combustion sub-models for the CFD-based prediction of NO x formation in biomass grate furnaces". In: *Combustion Theory and Modelling* 15.June 2013, pp. 61–87. DOI: 10.1080/13647830.2010.524312.

Appendix A

Additional results

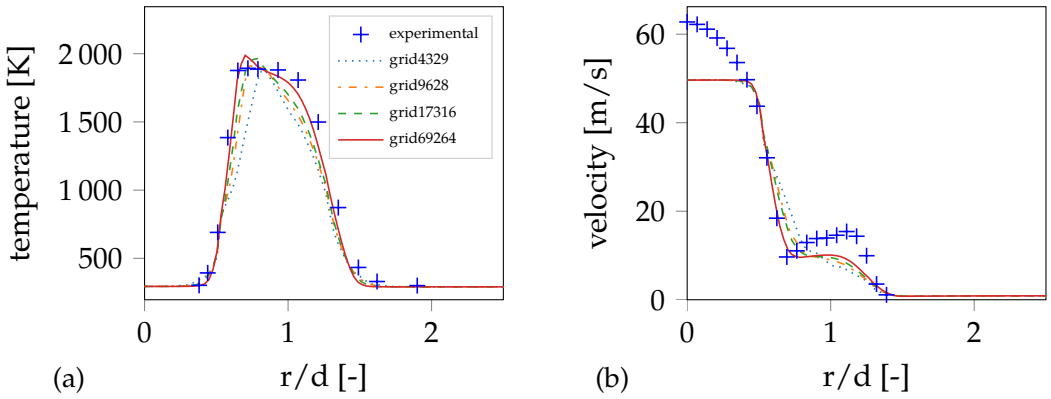

Figure A.1: Radial profiles at x/d=1 of the experimental data and the different grids tested in the grid convergence study for (a) temperature (b) velocity

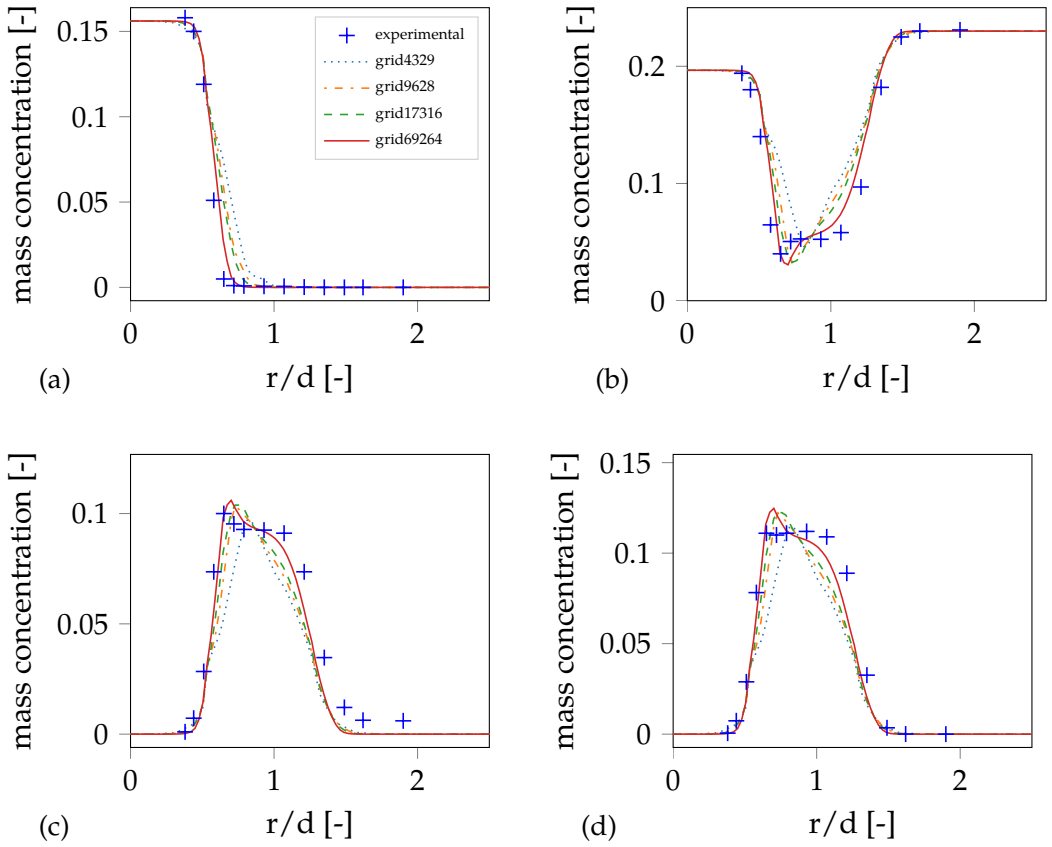

Figure A.2: Radial profiles at x/d=1 of the experimental data and the different grids tested in the grid convergence study for (a) CH_4 (b) O_2 (c) H_2O (d) CO_2

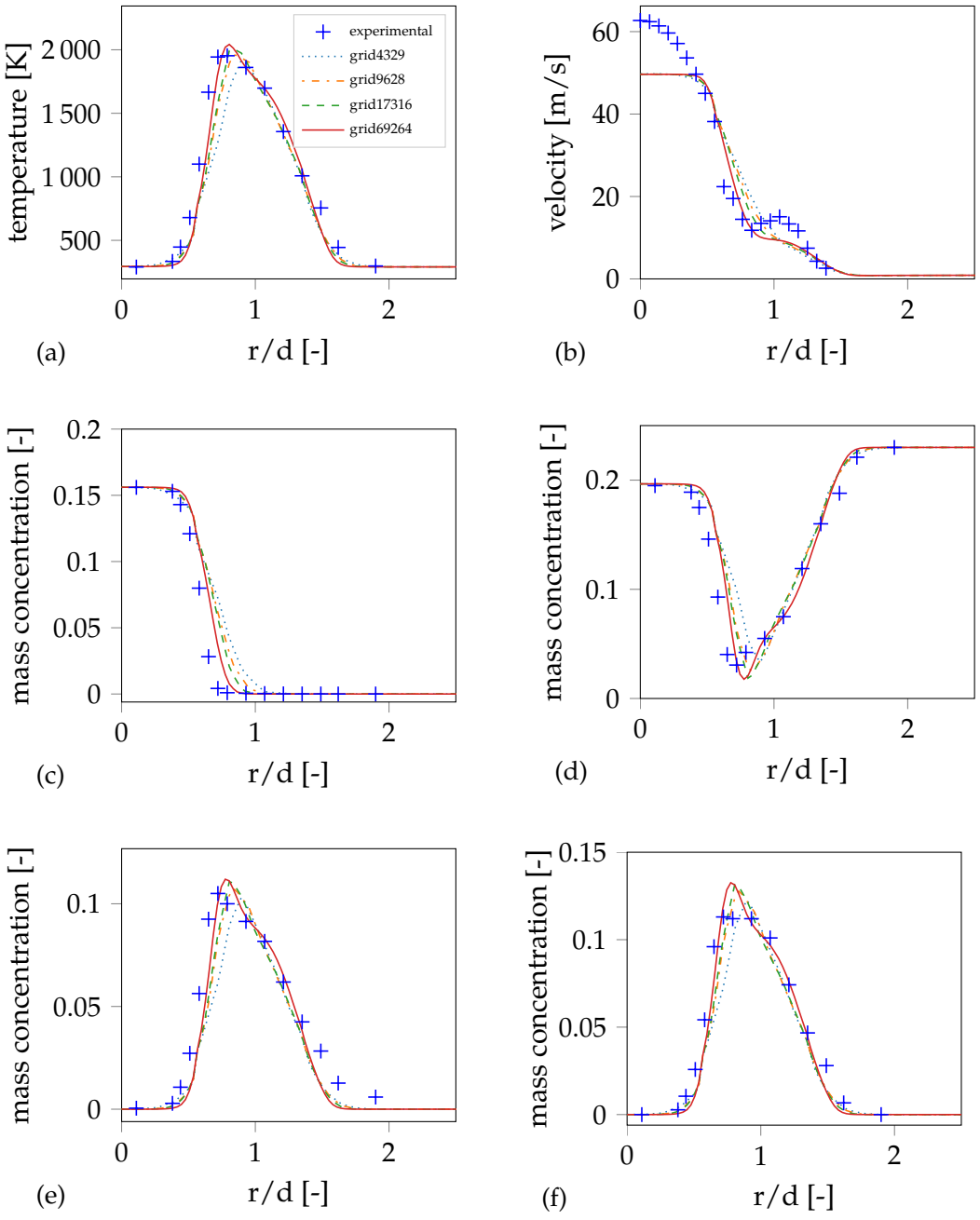

Figure A.3: Radial profiles at x/d=2 of the experimental data and the different grids tested in the grid convergence study for (a) temperature (b) velocity (c) CH_4 (d) O_2 (e) H_2O (f) CO_2

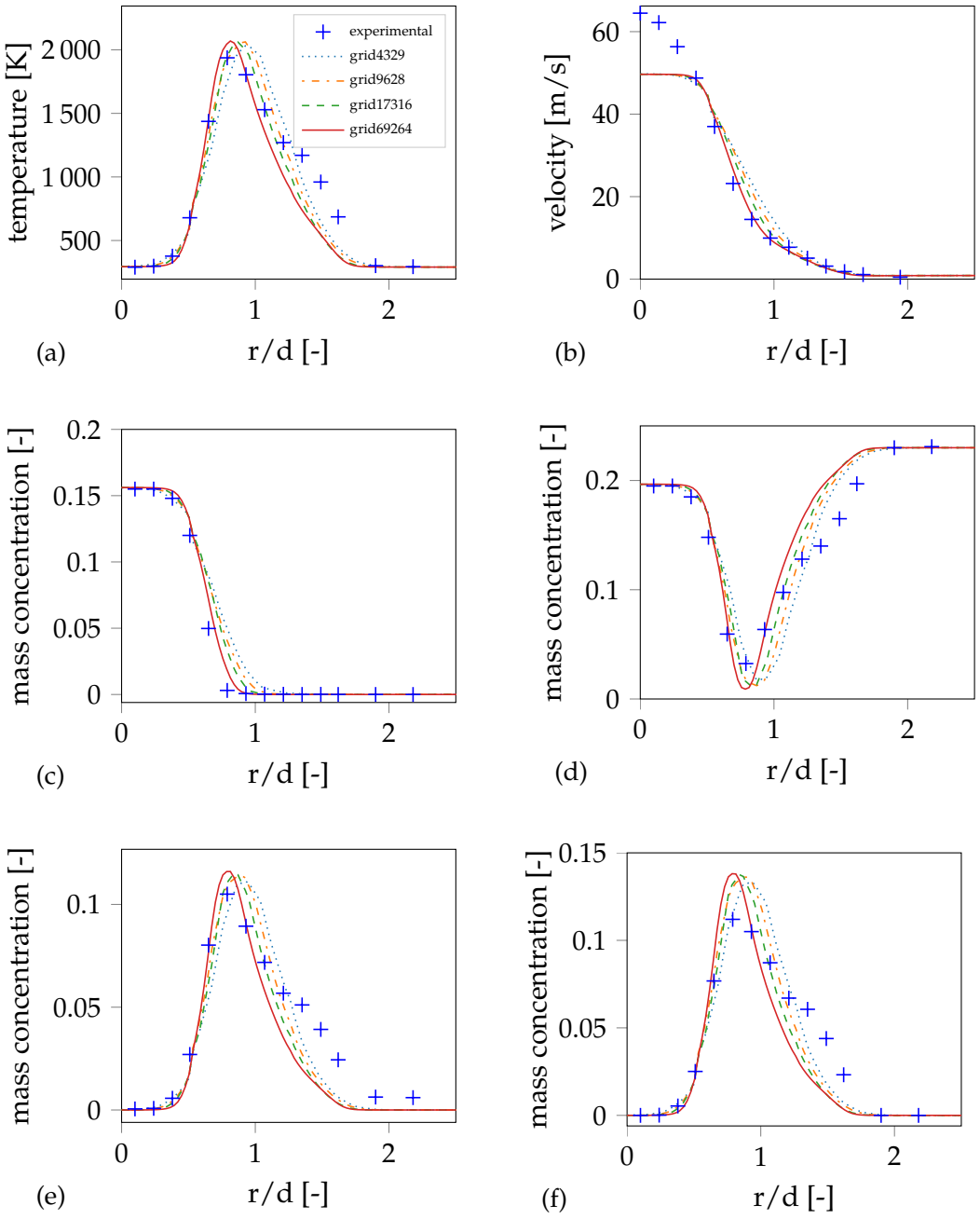

Figure A.4: Radial profiles at x/d=3 of the experimental data and the different grids tested in the grid convergence study for (a) temperature (b) velocity (c) CH_4 (d) O_2 (e) H_2O (f) CO_2

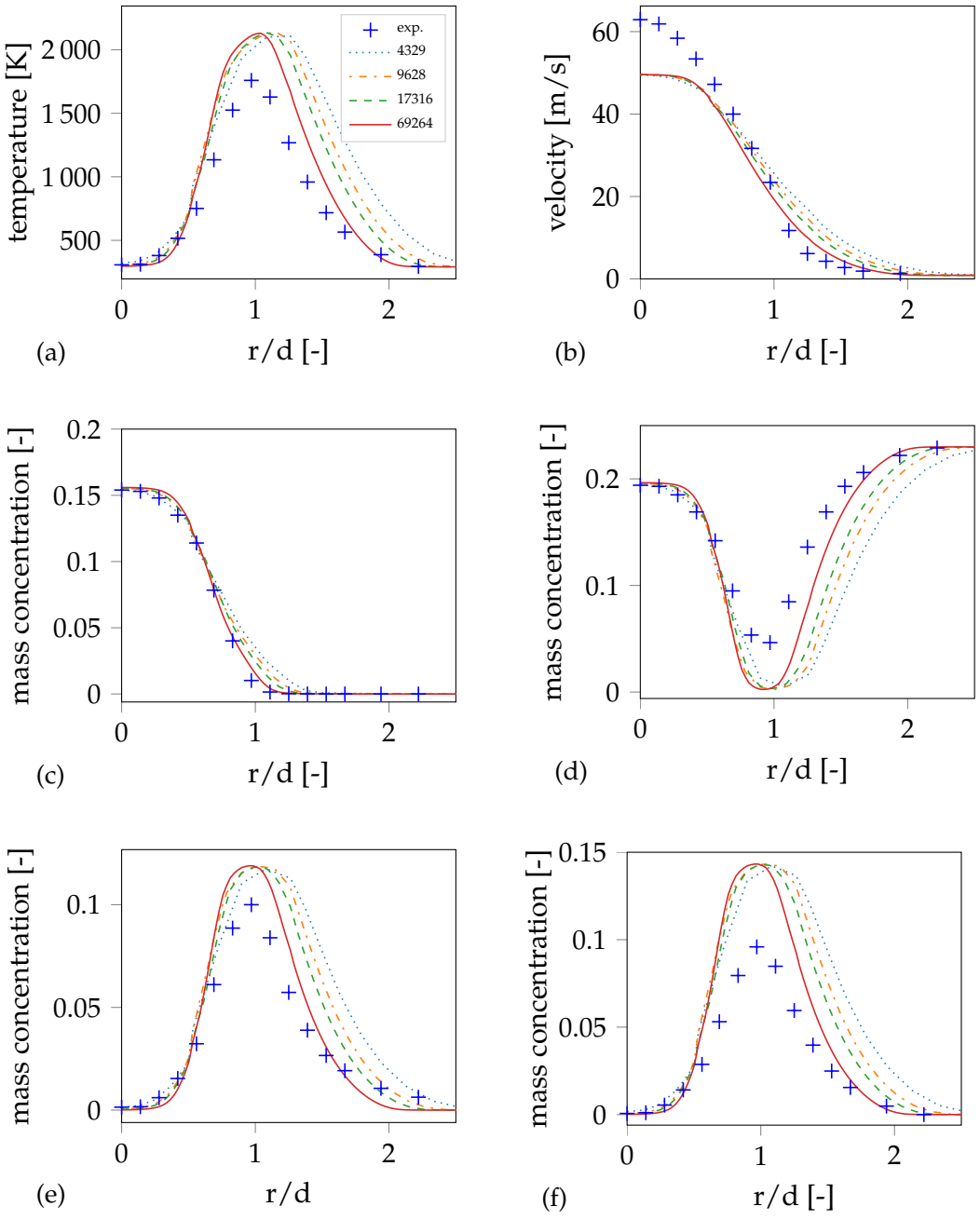

Figure A.5: Radial profiles at x/d=7.5 of the experimental data and the different grids tested in the grid convergence study for (a) temperature (b) velocity (c) CH_4 (d) O_2 (e) H_2O (f) CO_2

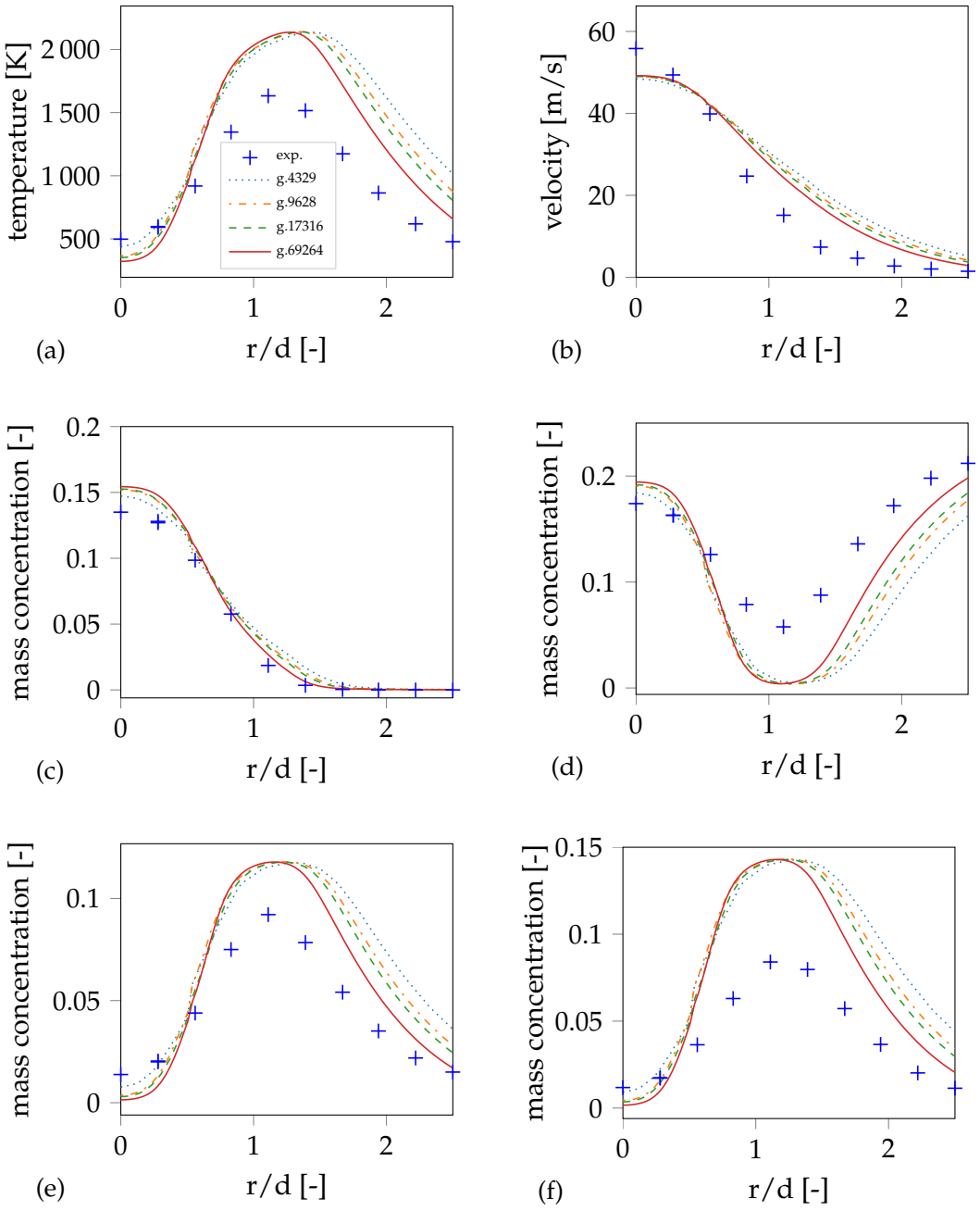

Figure A.6: Radial profiles at x/d=15 of the experimental data and the different grids tested in the grid convergence study for (a) temperature (b) velocity (c) CH_4 (d) O_2 (e) H_2O (f) CO_2

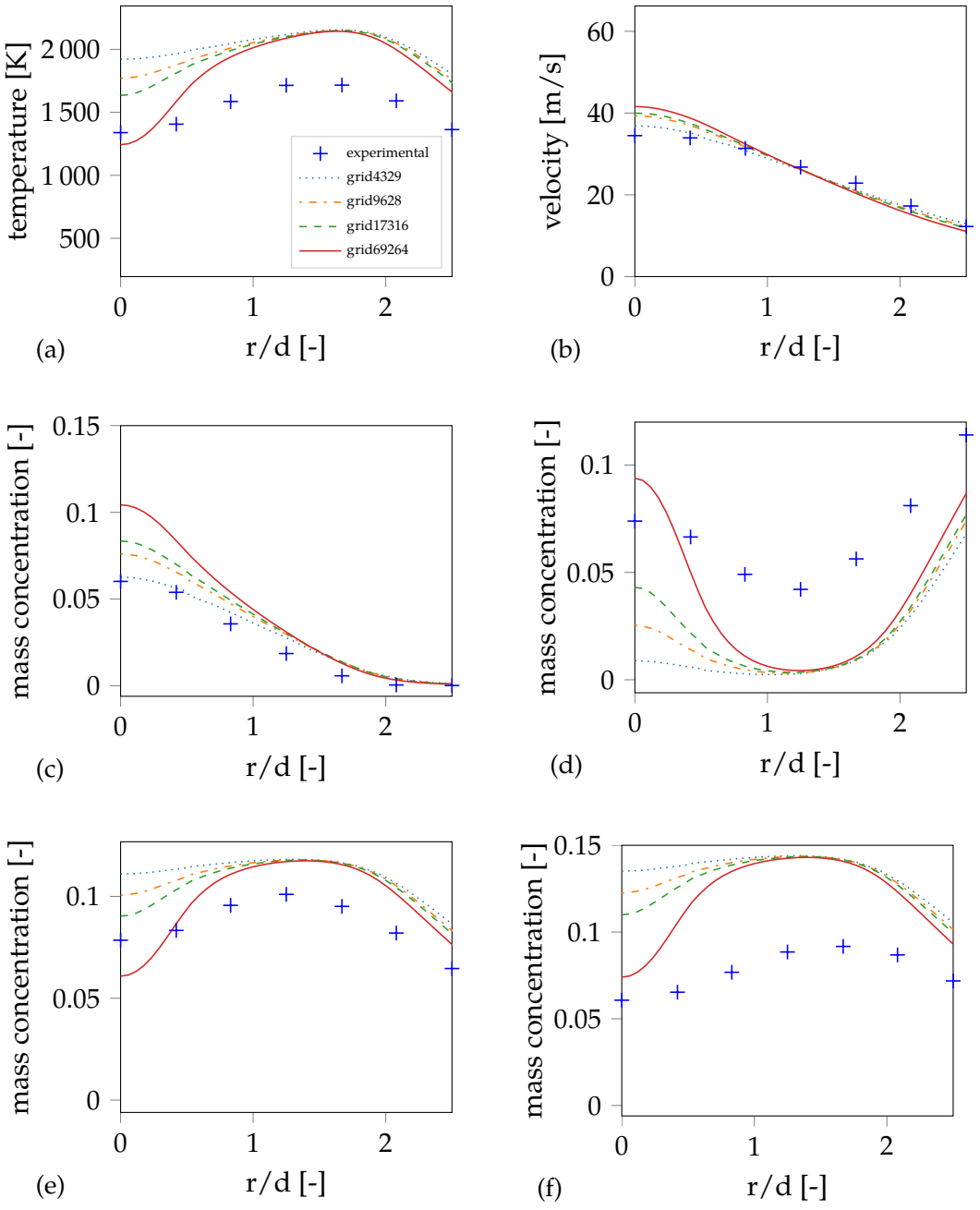

Figure A.7: Radial profiles at x/d=30 of the experimental data and the different grids tested in the grid convergence study for (a) temperature (b) velocity (c) CH_4 (d) O_2 (e) H_2O (f) CO_2

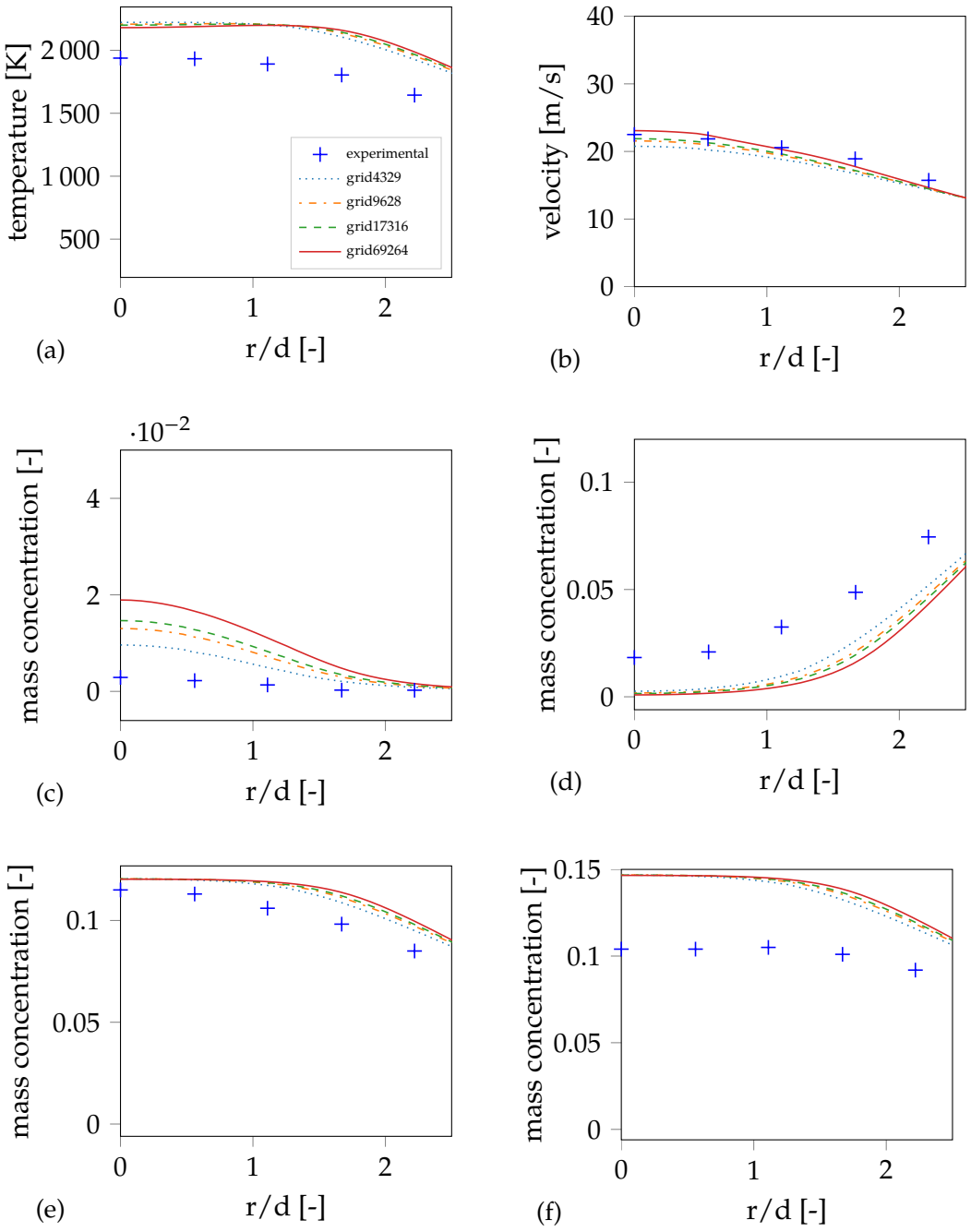

Figure A.8: Radial profiles at x/d=45 of the experimental data and the different grids tested in the grid convergence study for (a) temperature (b) velocity (c) CH_4 (d) O_2 (e) H_2O (f) CO_2

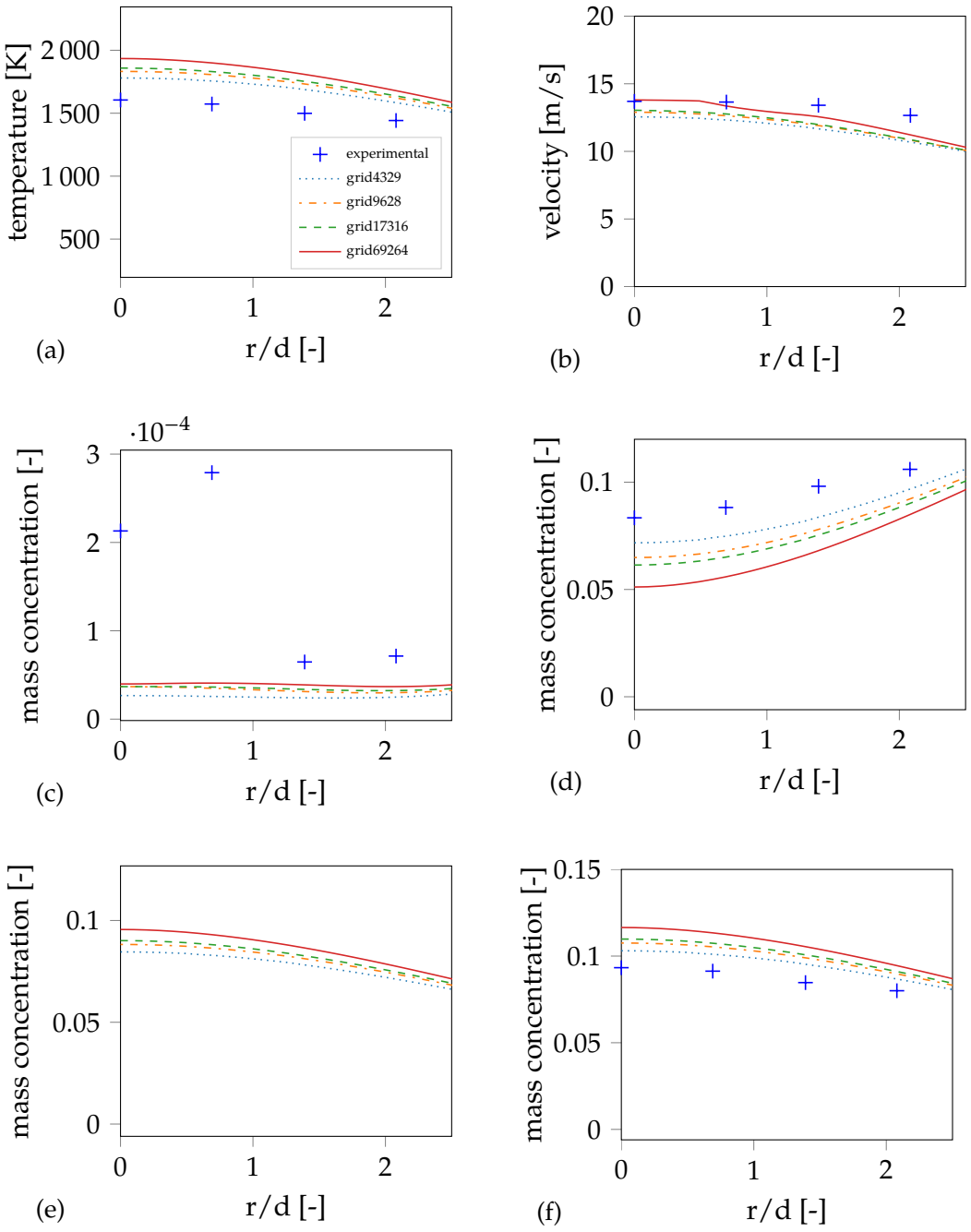

Figure A.9: Radial profiles at x/d=60 of the experimental data and the different grids tested in the grid convergence study for (a) temperature (b) velocity (c) CH_4 (d) O_2 (e) H_2O (f) CO_2

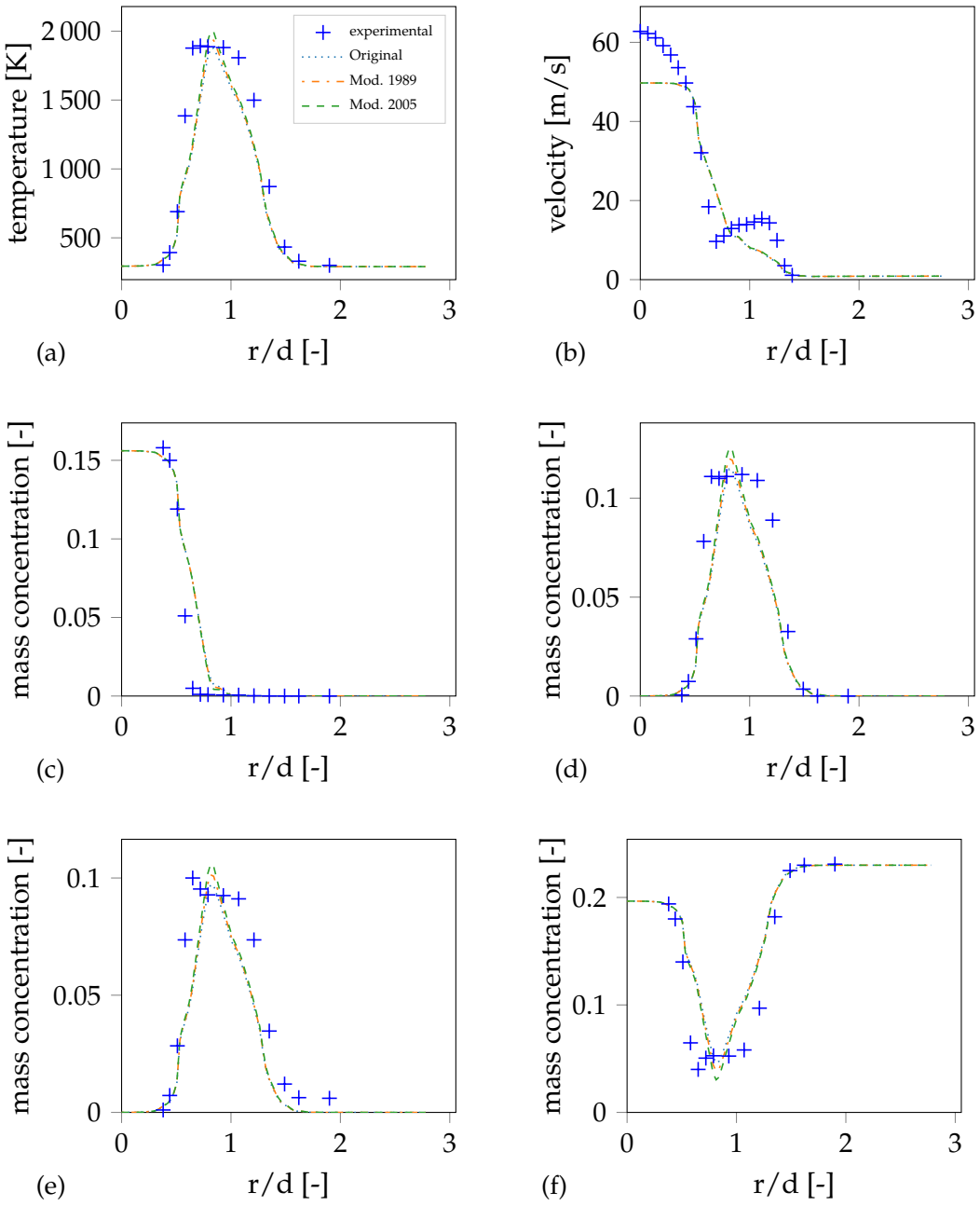

Figure A.10: Radial profiles at x/d=1 comparing the different EDC modifications using a global mechanism for (a) temperature, (b) velocity, and species concentration (c) CH_4, (d) CO_2, (e) H_2O and (f) O_2

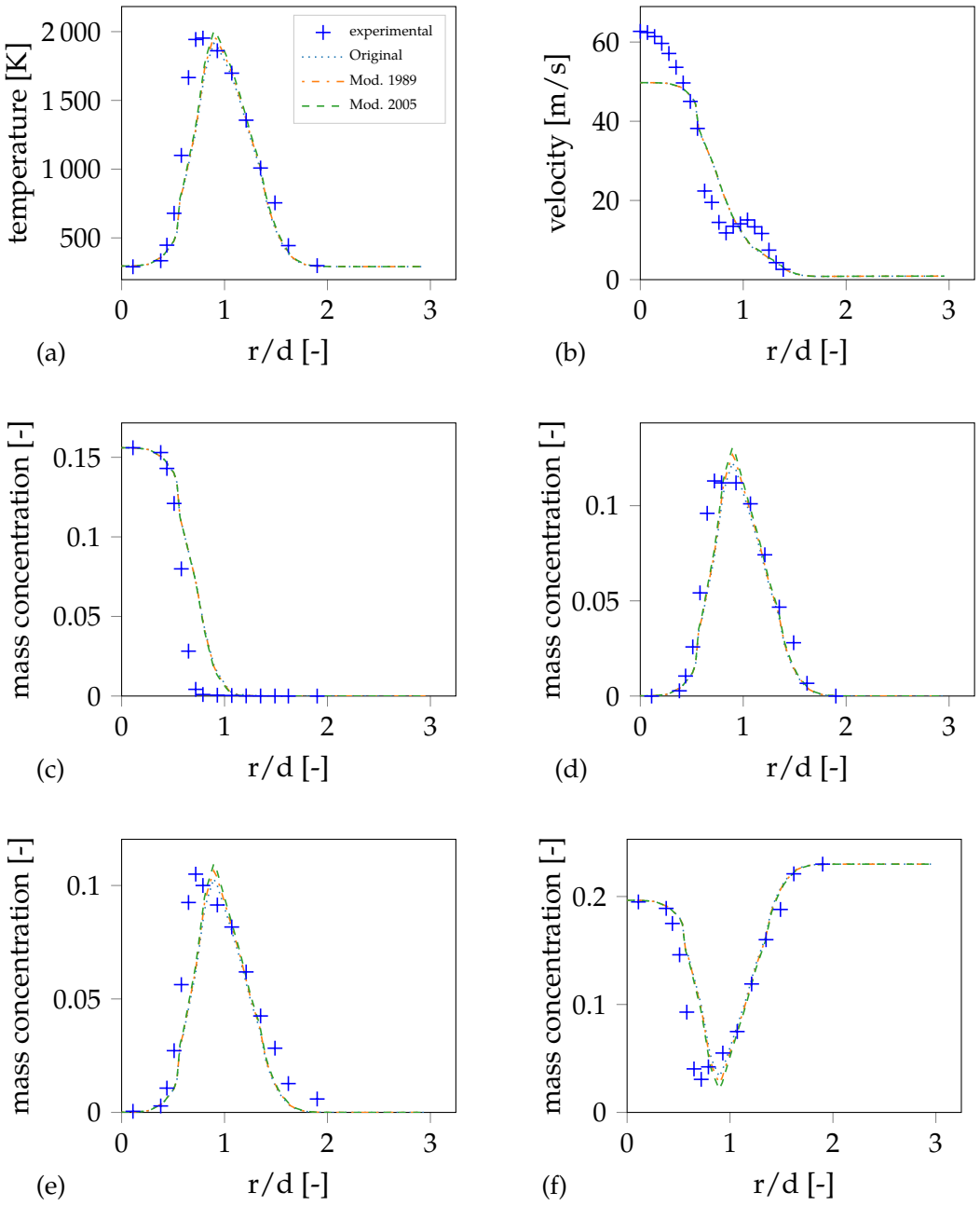

Figure A.11: Radial profiles at x/d=2 comparing the different EDC modifications using a global mechanism for (a) temperature, (b) velocity, and species concentration (c) CH_4, (d) CO_2, (e) H_2O and (f) O_2

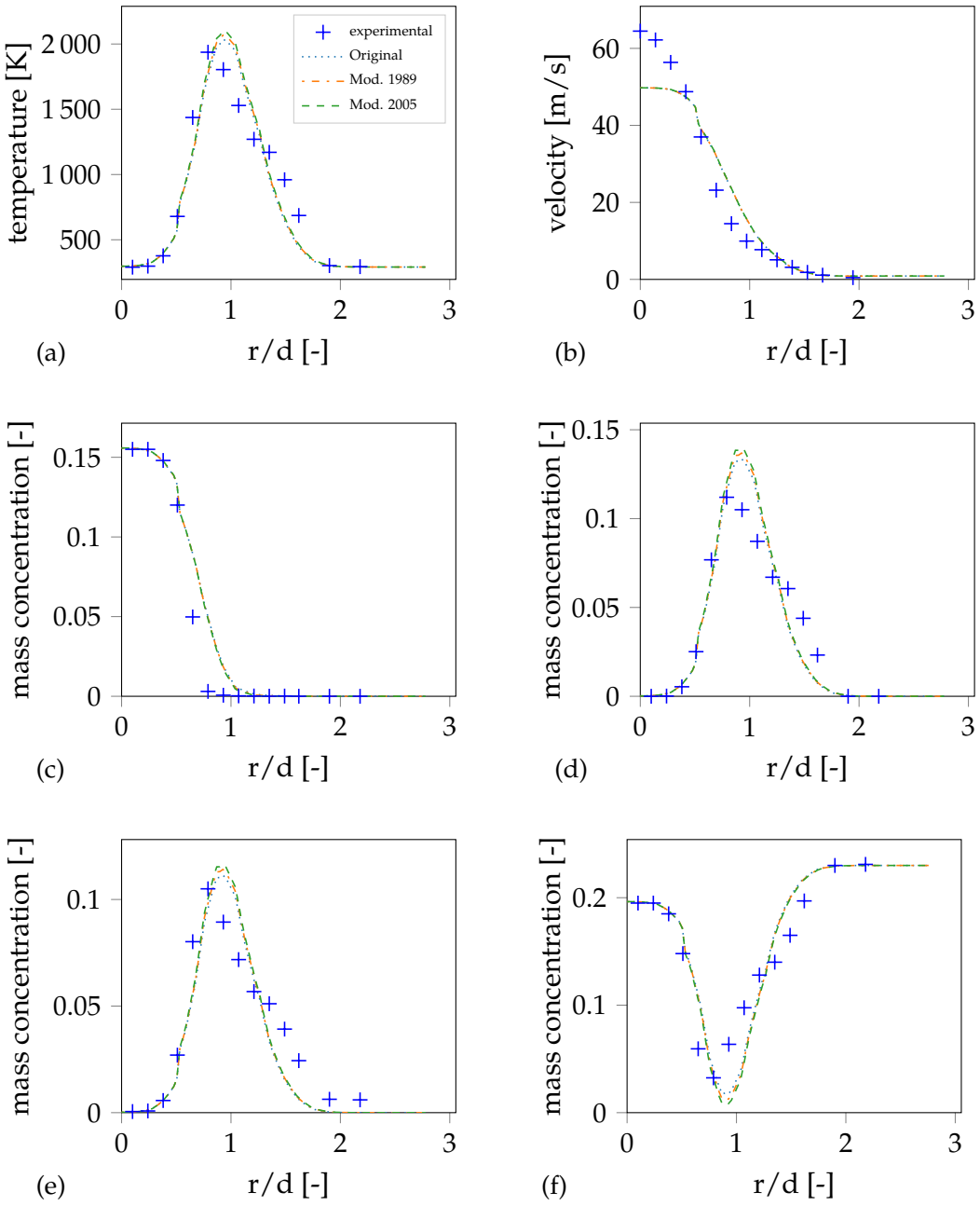

Figure A.12: Radial profiles at x/d=3 comparing the different EDC modifications using a global mechanism for (a) temperature, (b) velocity, and species concentration (c) CH_4, (d) CO_2, (e) H_2O and (f) O_2

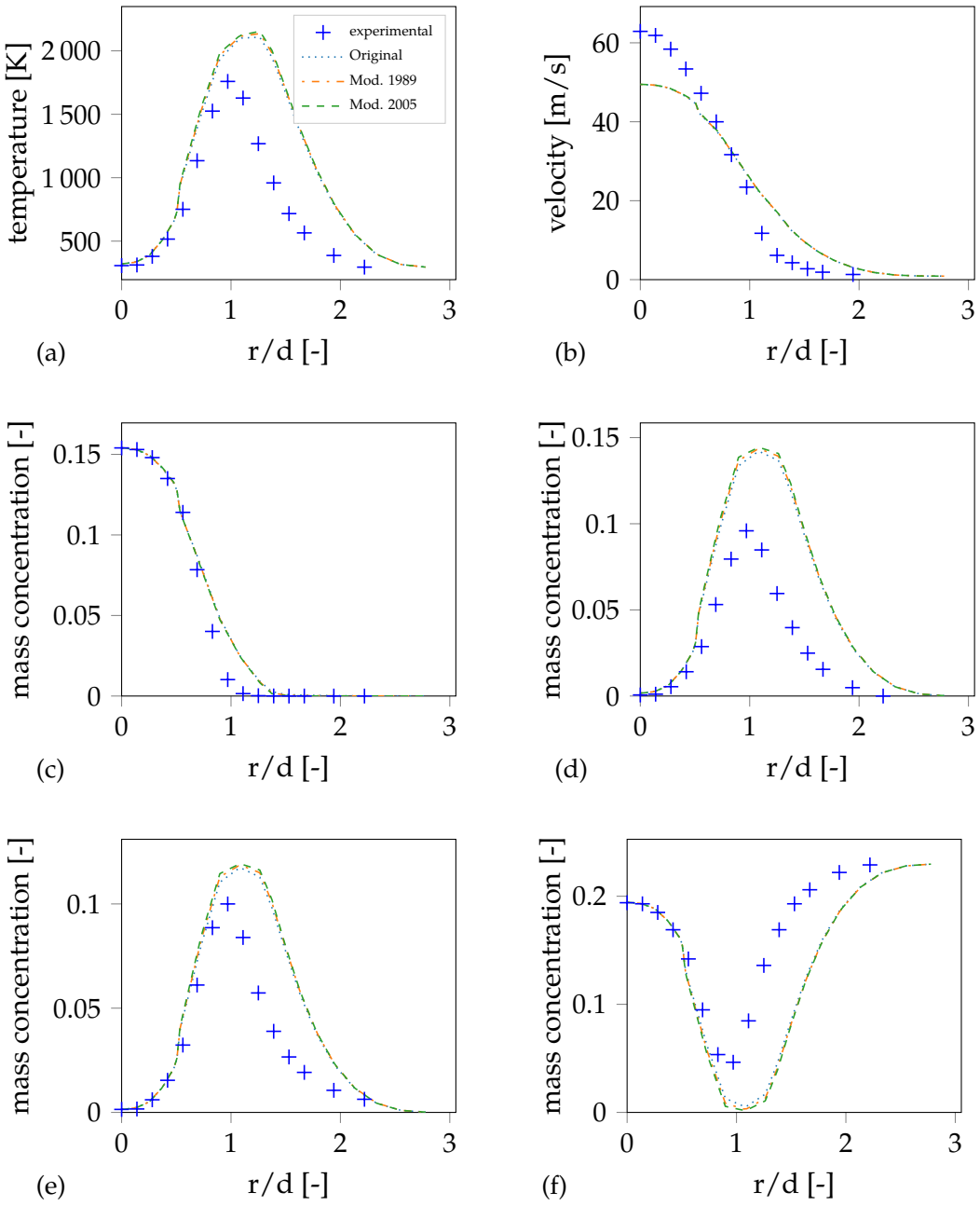

Figure A.13: Radial profiles at x/d=7.5 comparing the different EDC modifications using a global mechanism for (a) temperature, (b) velocity, and species concentration (c) CH_4, (d) CO_2, (e) H_2O and (f) O_2

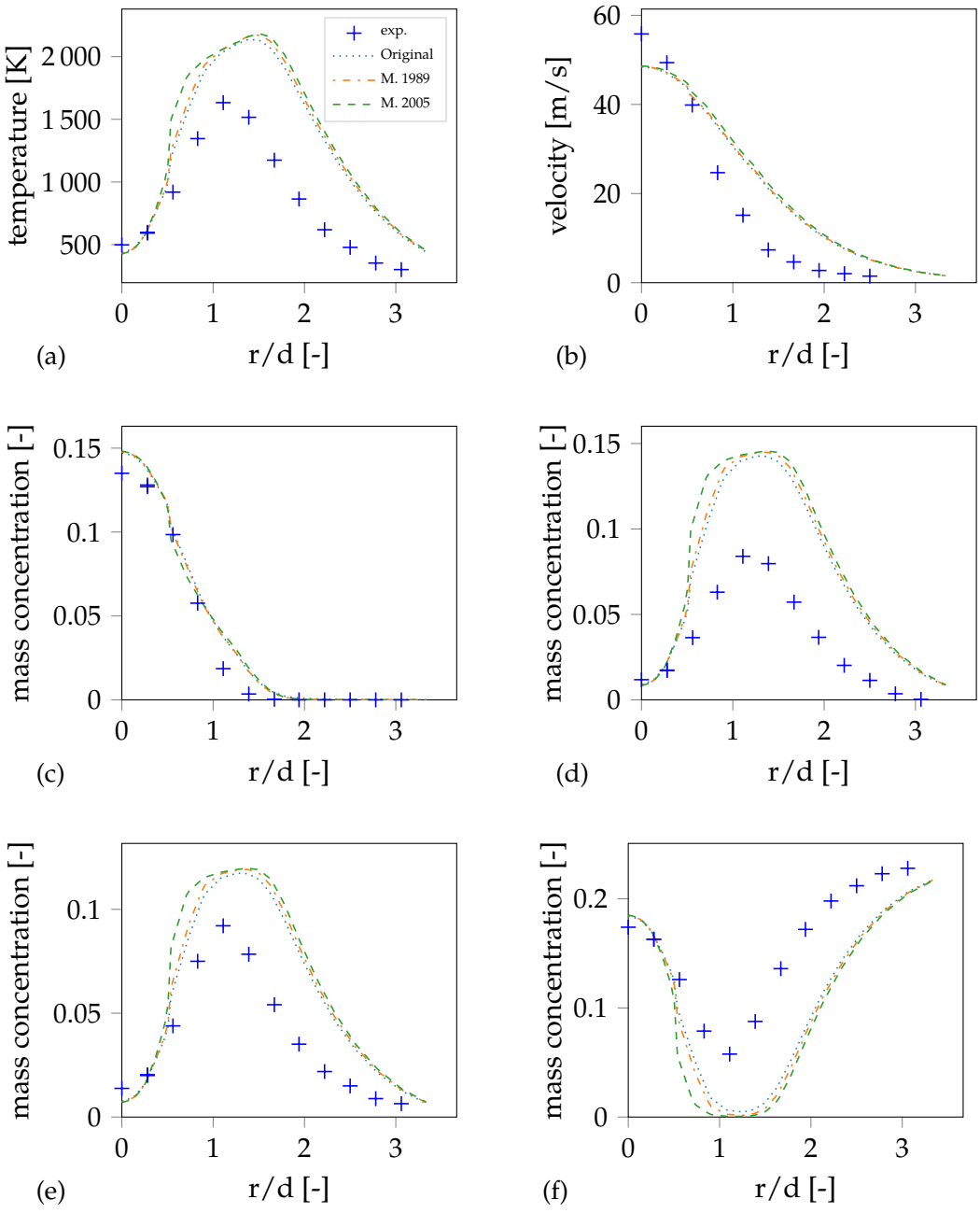

Figure A.14: Radial profiles at x/d=15 comparing the different EDC modifications using a global mechanism for (a) temperature, (b) velocity, and species concentration (c) CH_4, (d) CO_2, (e) H_2O and (f) O_2

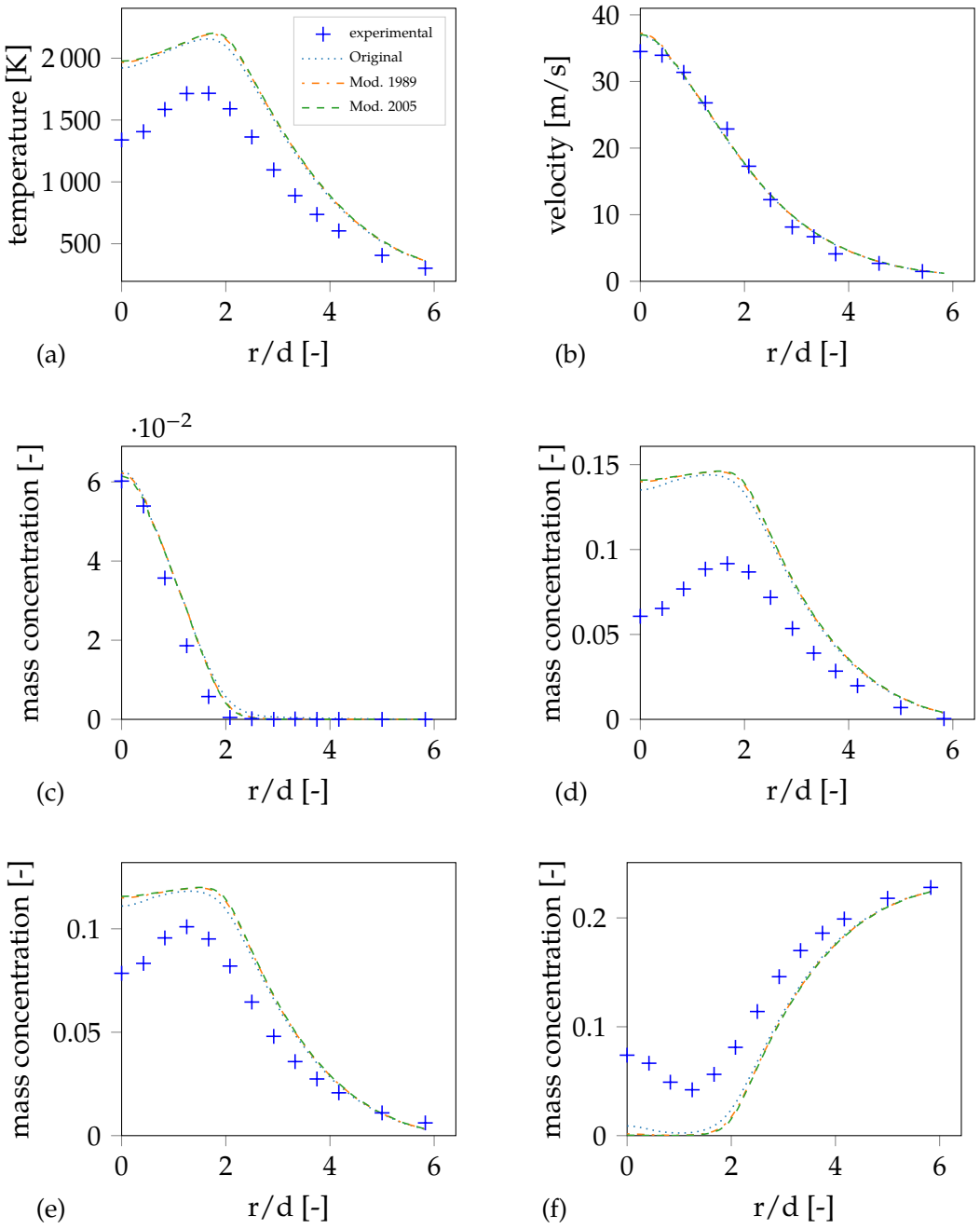

Figure A.15: Radial profiles at x/d=30 comparing the different EDC modifications using a global mechanism for (a) temperature, (b) velocity, and species concentration (c) CH_4, (d) CO_2, (e) H_2O and (f) O_2

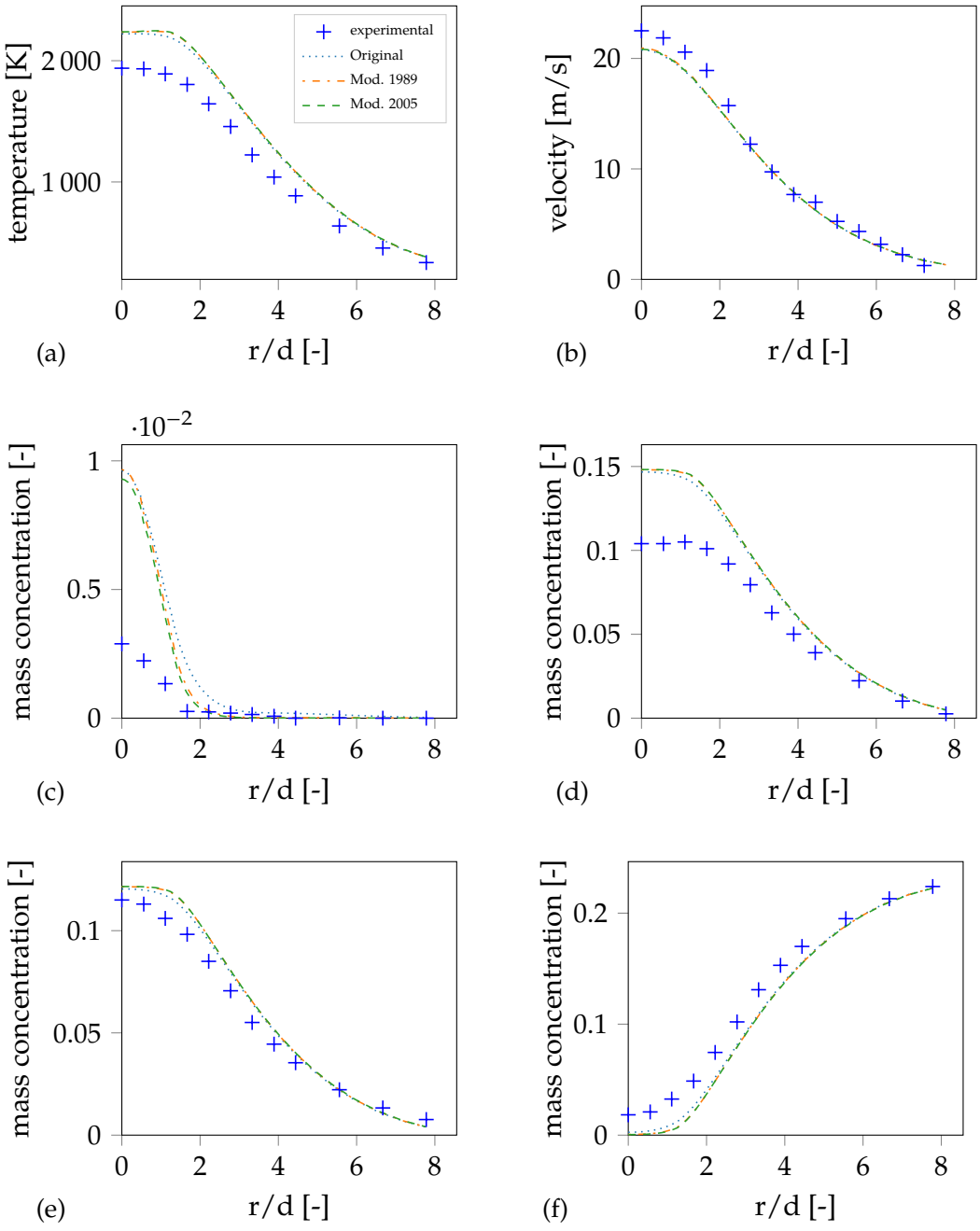

Figure A.16: Radial profiles at x/d=45 comparing the different EDC modifications using a global mechanism for (a) temperature, (b) velocity, and species concentration (c) CH_4, (d) CO_2, (e) H_2O and (f) O_2

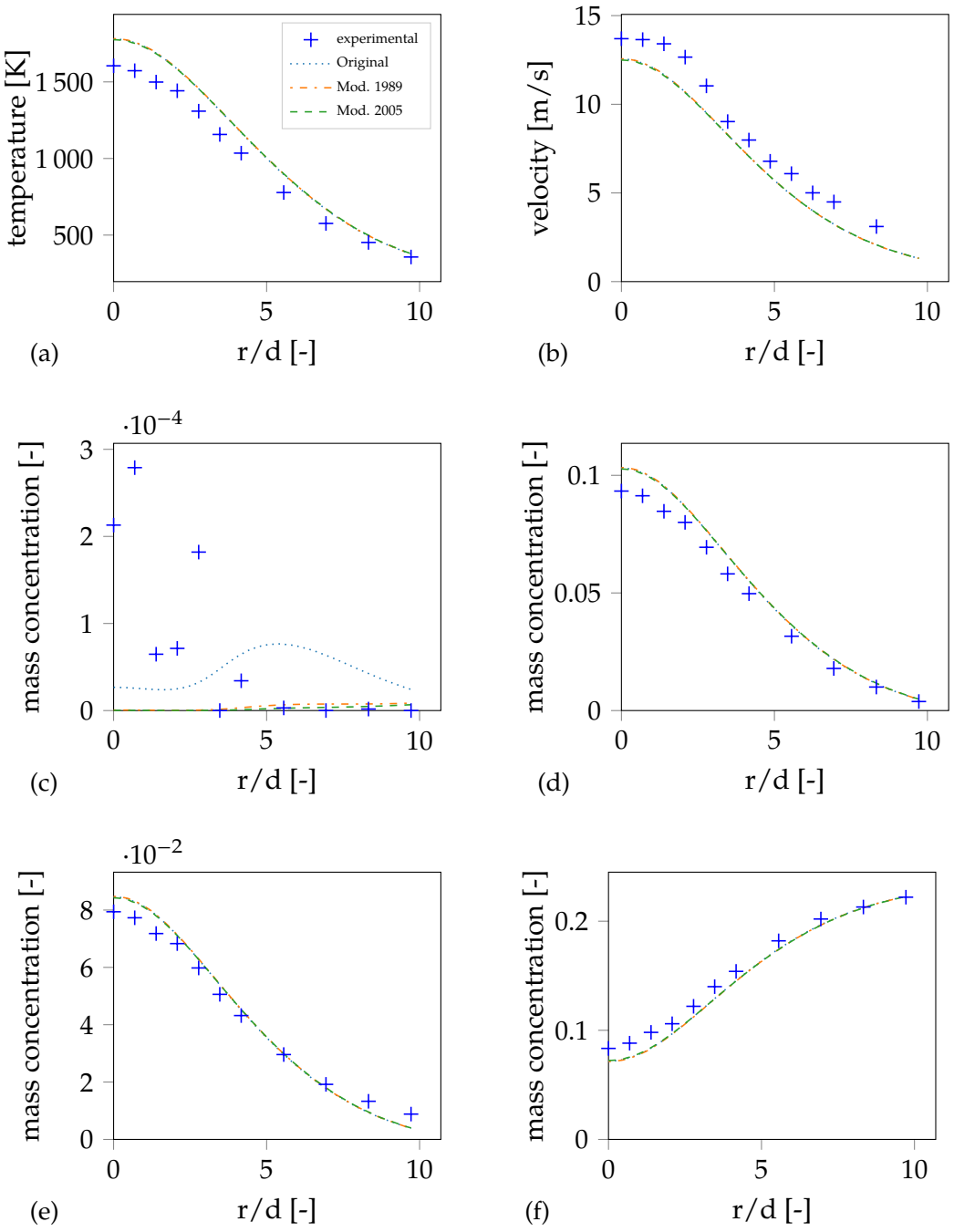

Figure A.17: Radial profiles at x/d=60 comparing the different EDC modifications using a global mechanism for (a) temperature, (b) velocity, and species concentration (c) CH_4, (d) CO_2, (e) H_2O and (f) O_2

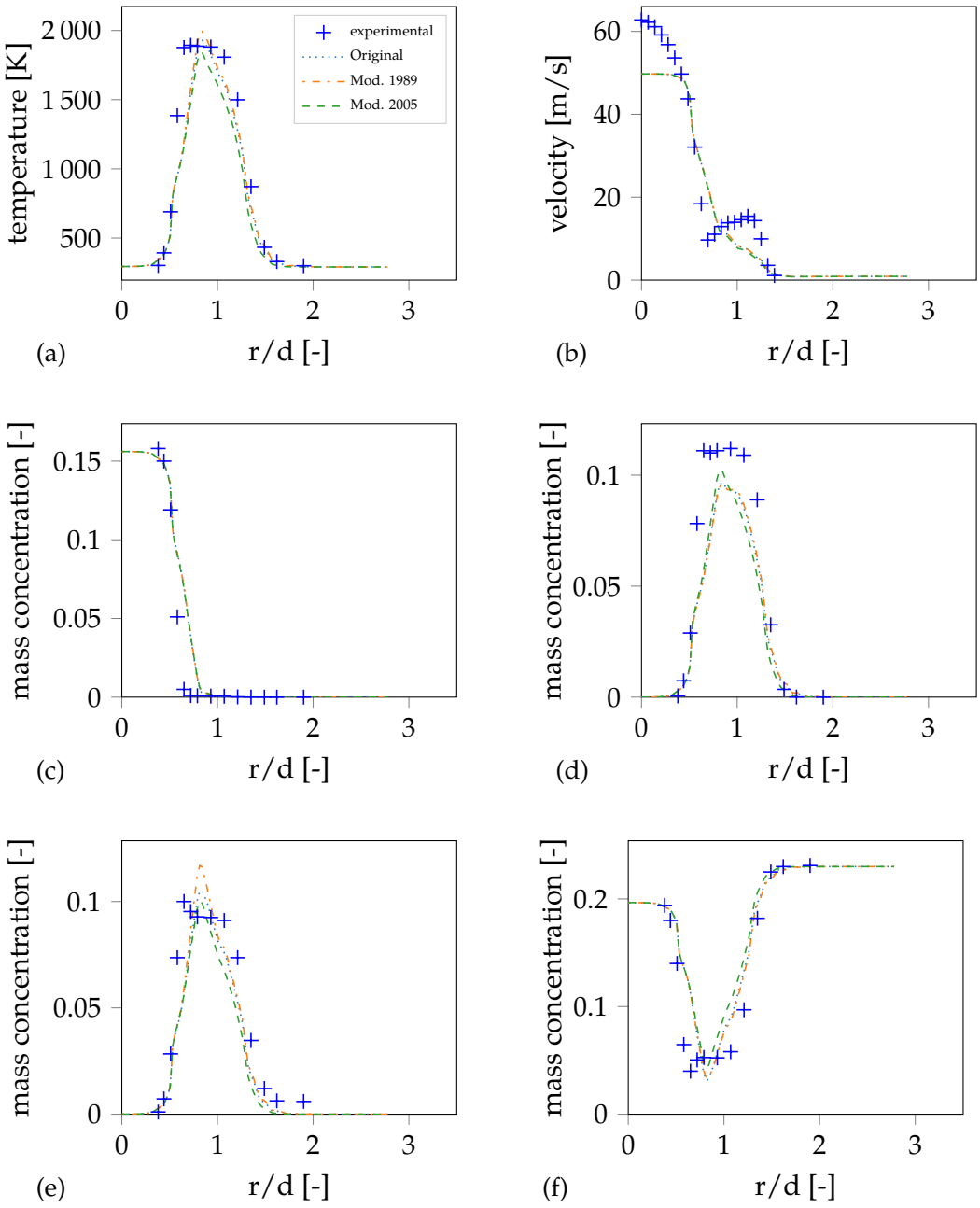

Figure A.18: Radial profiles at x/d=1 comparing the different EDC modifications using GRI-3.0 (a) temperature, (b) velocity, and species concentration (c) CH_4, (d) CO_2, (e) H_2O and (f) O_2

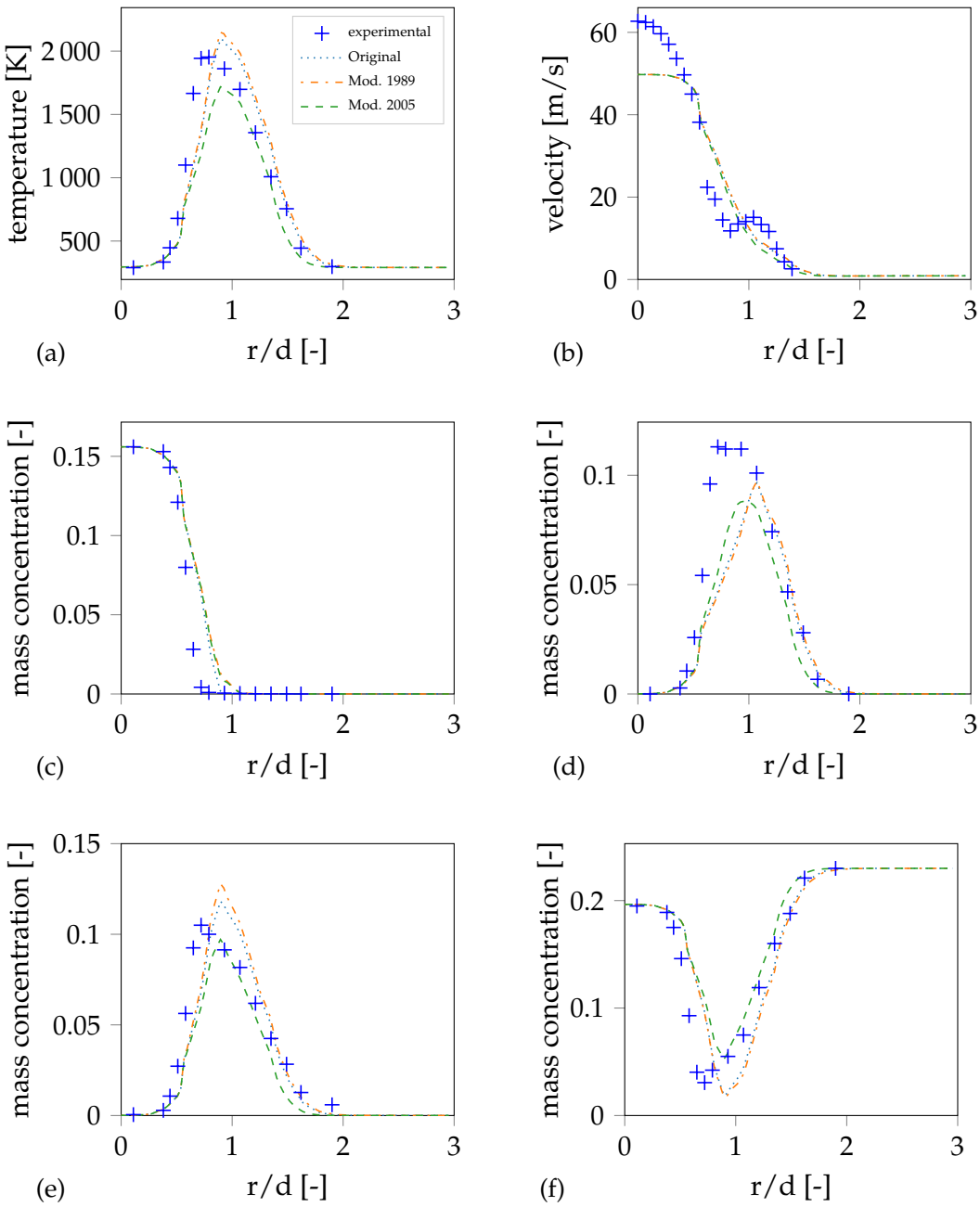

Figure A.19: Radial profiles at x/d=2 comparing the different EDC modifications using GRI-3.0 (a) temperature, (b) velocity, and species concentration (c) CH_4, (d) CO_2, (e) H_2O and (f) O_2

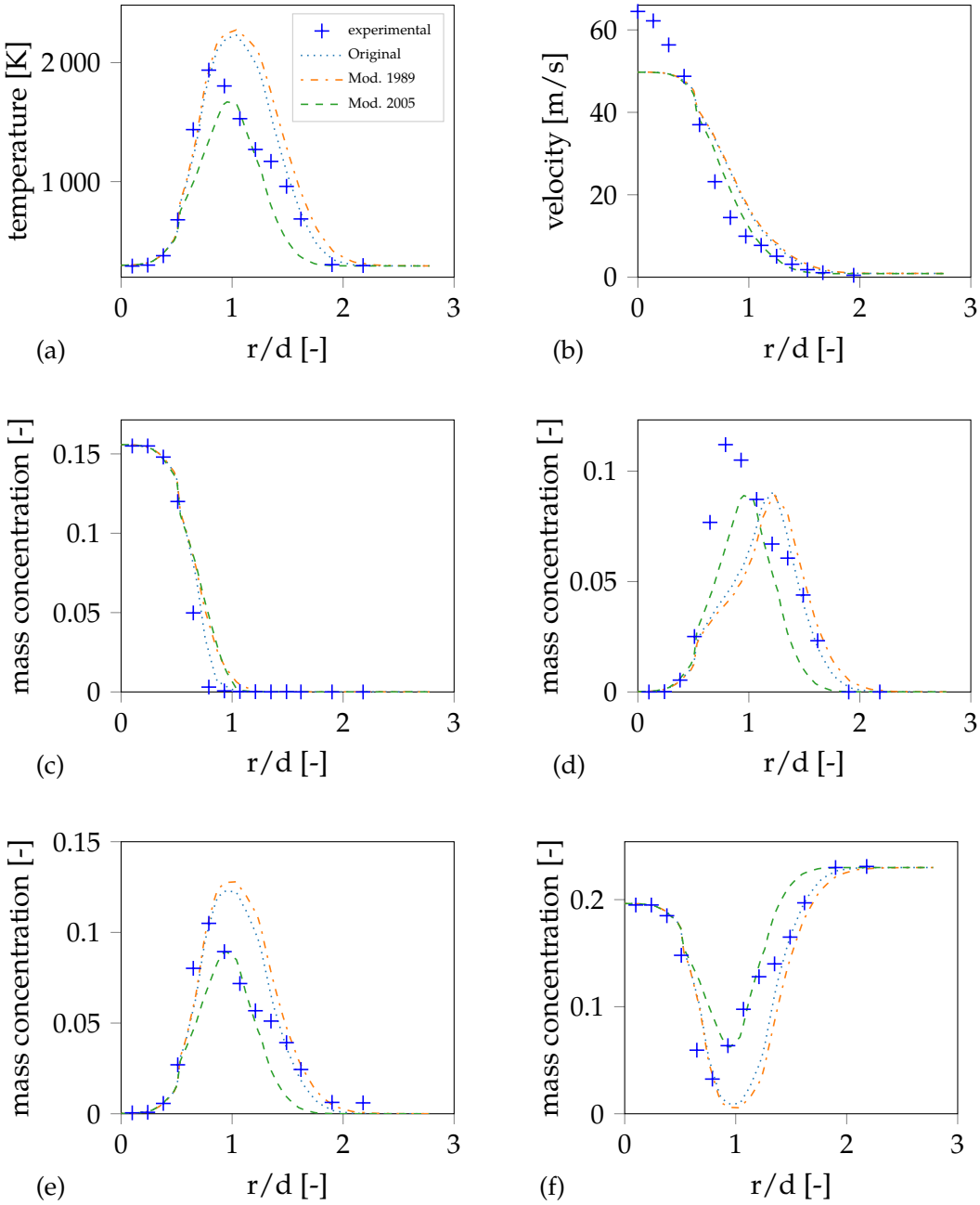

Figure A.20: Radial profiles at x/d=3 comparing the different EDC modifications using GRI-3.0 (a) temperature, (b) velocity, and species concentration (c) CH_4, (d) CO_2, (e) H_2O and (f) O_2

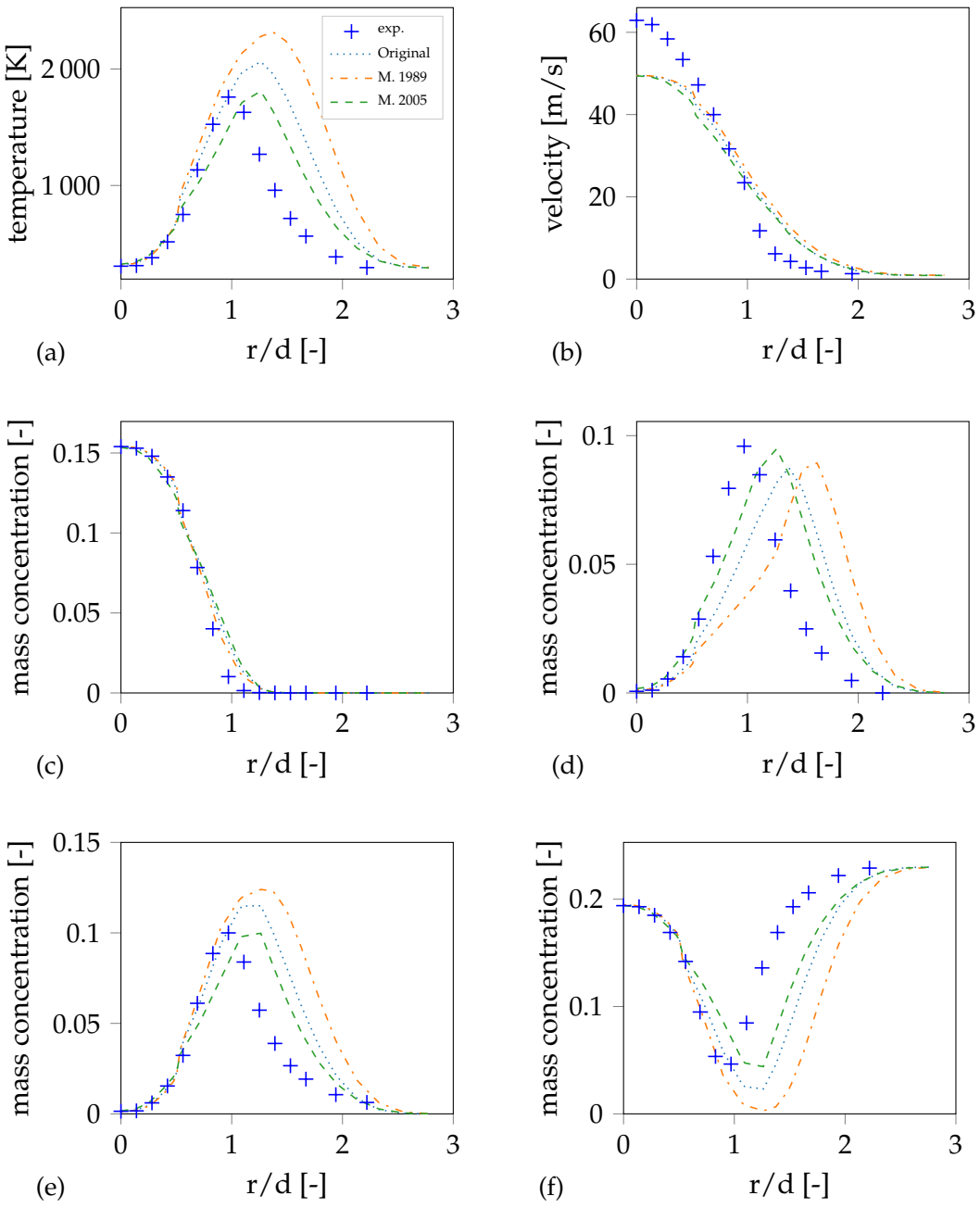

Figure A.21: Radial profiles at x/d=7.5 comparing the different EDC modifications using GRI-3.0 (a) temperature, (b) velocity, and species concentration (c) CH_4, (d) CO_2, (e) H_2O and (f) O_2

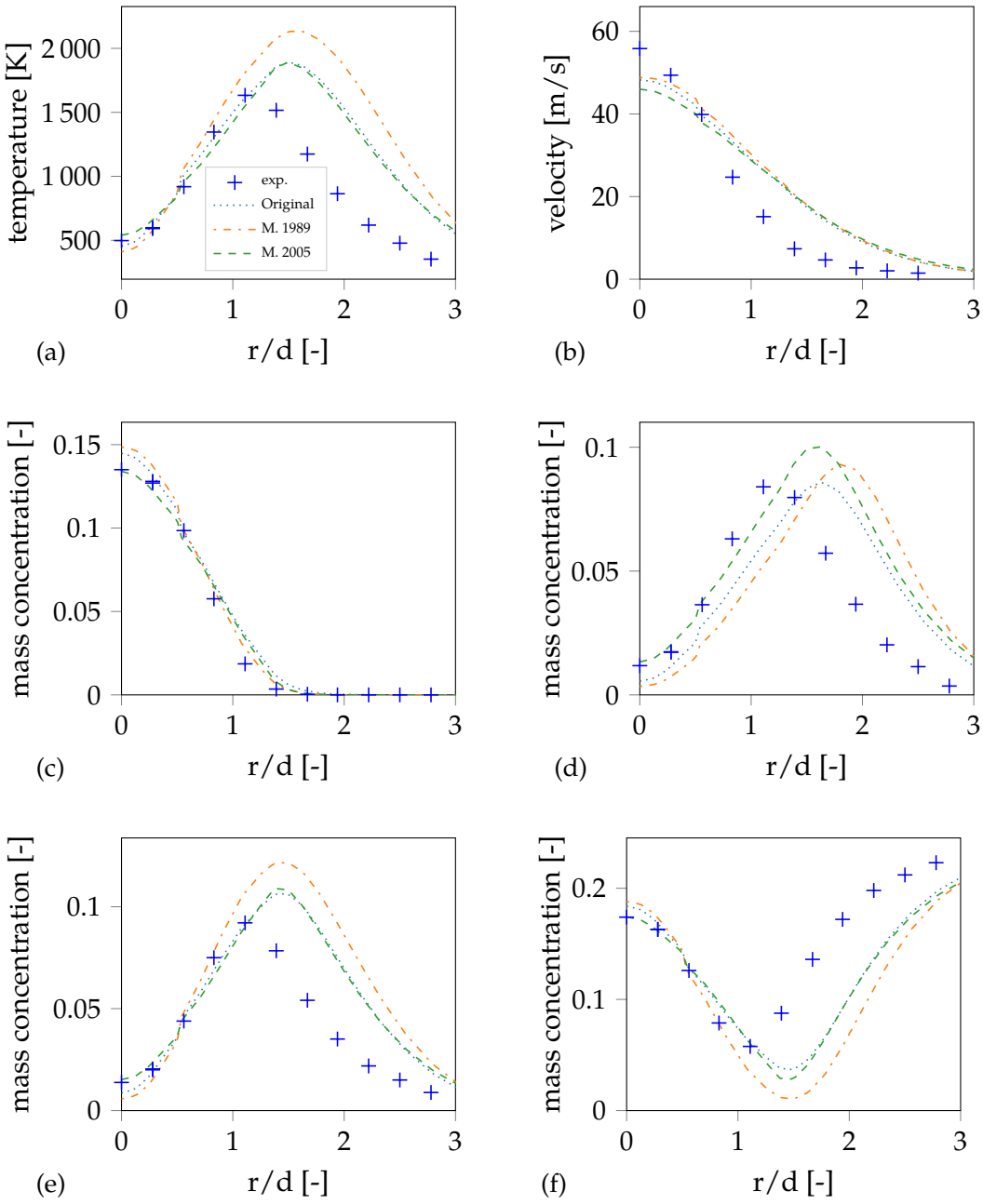

Figure A.22: Radial profiles at x/d=15 comparing the different EDC modifications using GRI-3.0 (a) temperature, (b) velocity, and species concentration (c) CH_4, (d) CO_2, (e) H_2O and (f) O_2

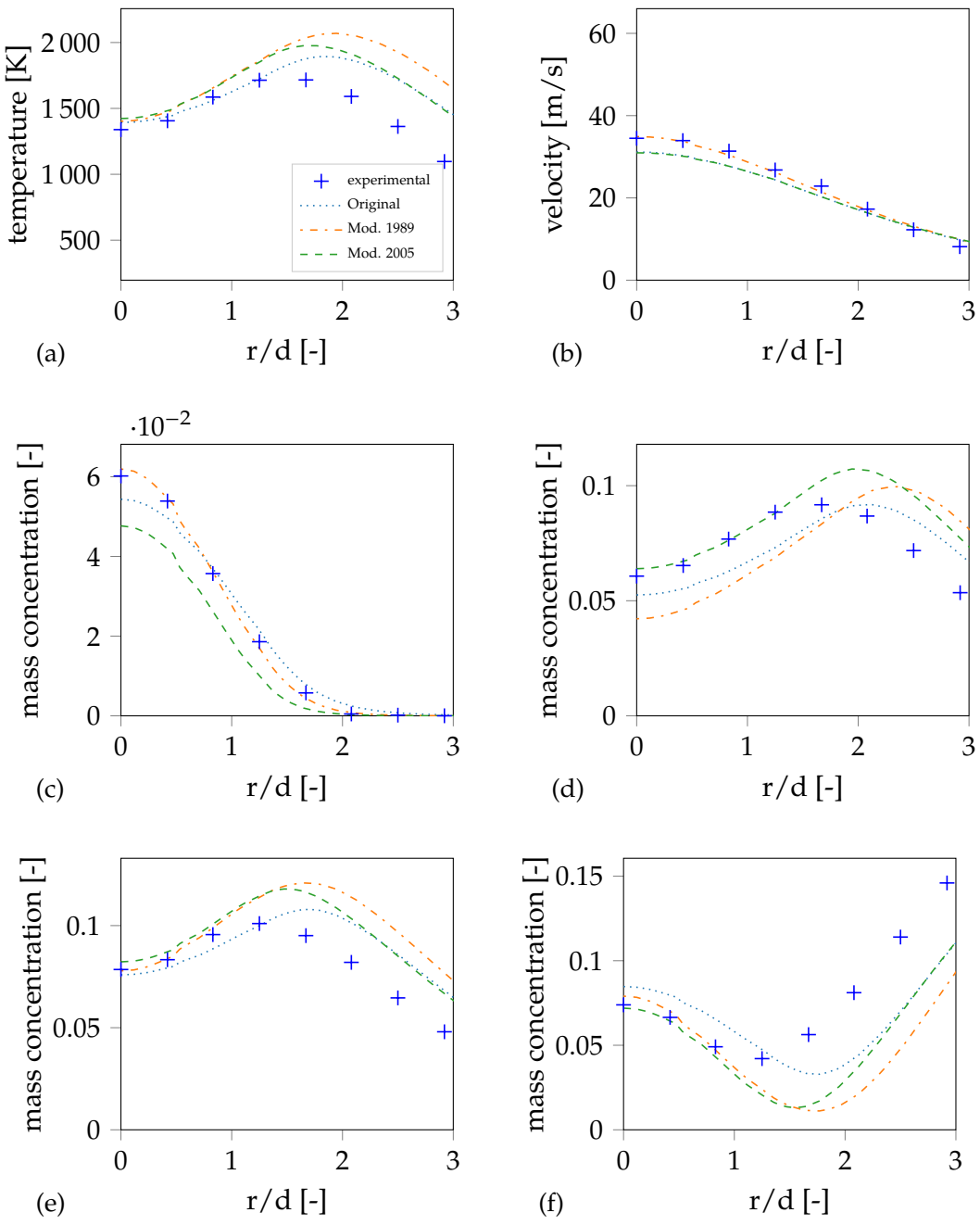

Figure A.23: Radial profiles at x/d=30 comparing the different EDC modifications using GRI-3.0 (a) temperature, (b) velocity, and species concentration (c) CH_4, (d) CO_2, (e) H_2O and (f) O_2

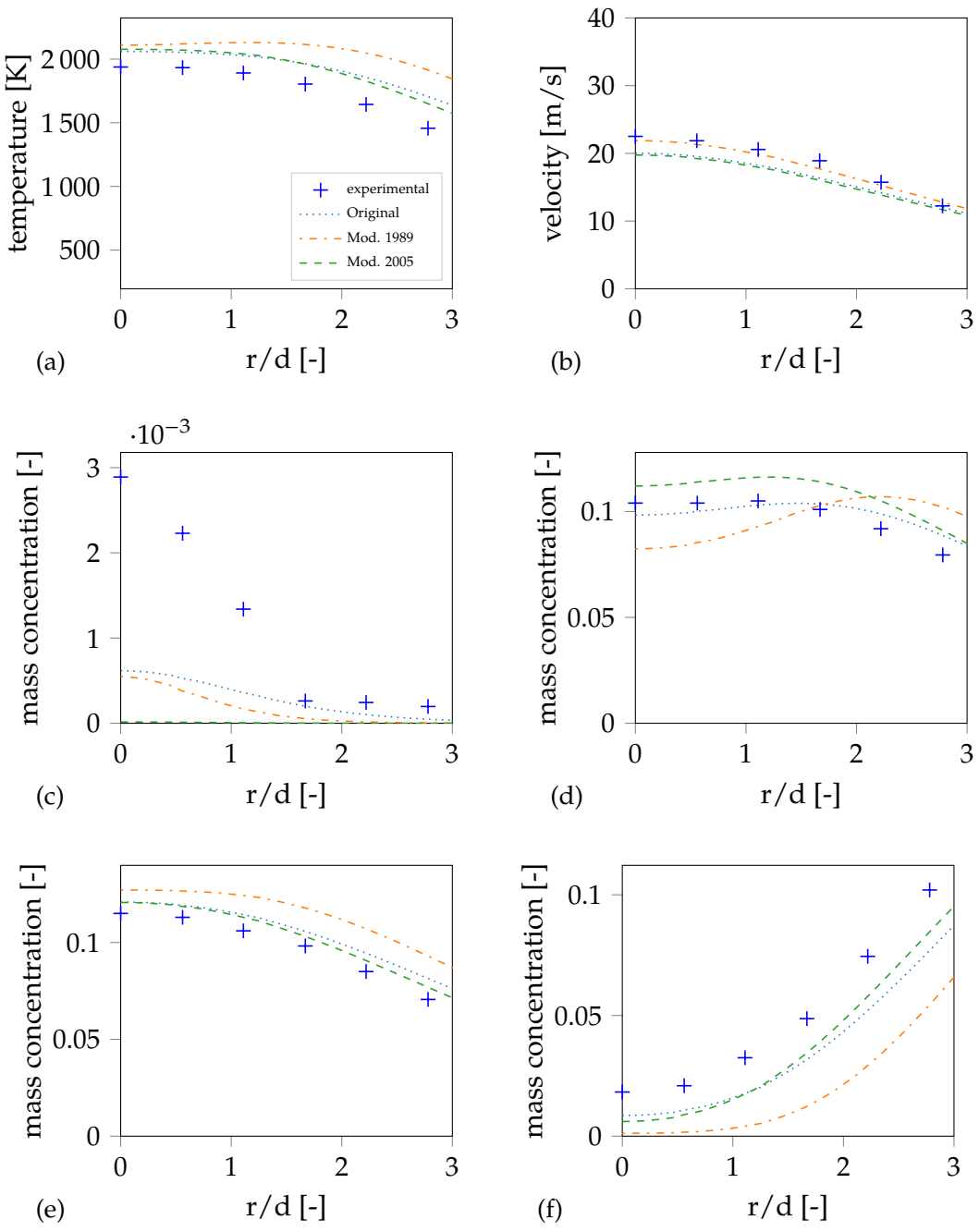

Figure A.24: Radial profiles at x/d=45 comparing the different EDC modifications using GRI-3.0 (a) temperature, (b) velocity, and species concentration (c) CH_4, (d) CO_2, (e) H_2O and (f) O_2

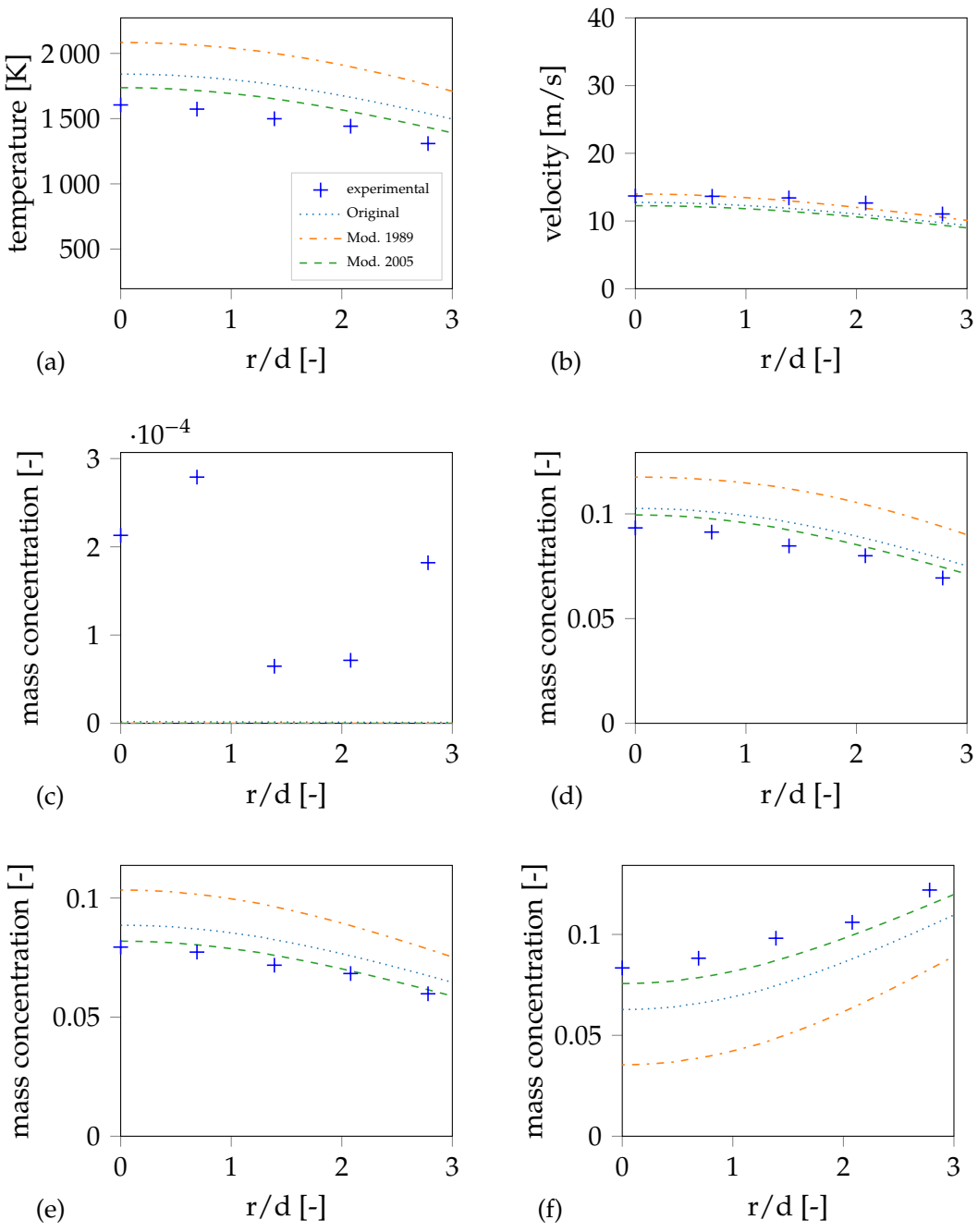

Figure A.25: Radial profiles at x/d=60 comparing the different EDC modifications using GRI-3.0 (a) temperature, (b) velocity, and species concentration (c) CH_4, (d) CO_2, (e) H_2O and (f) O_2

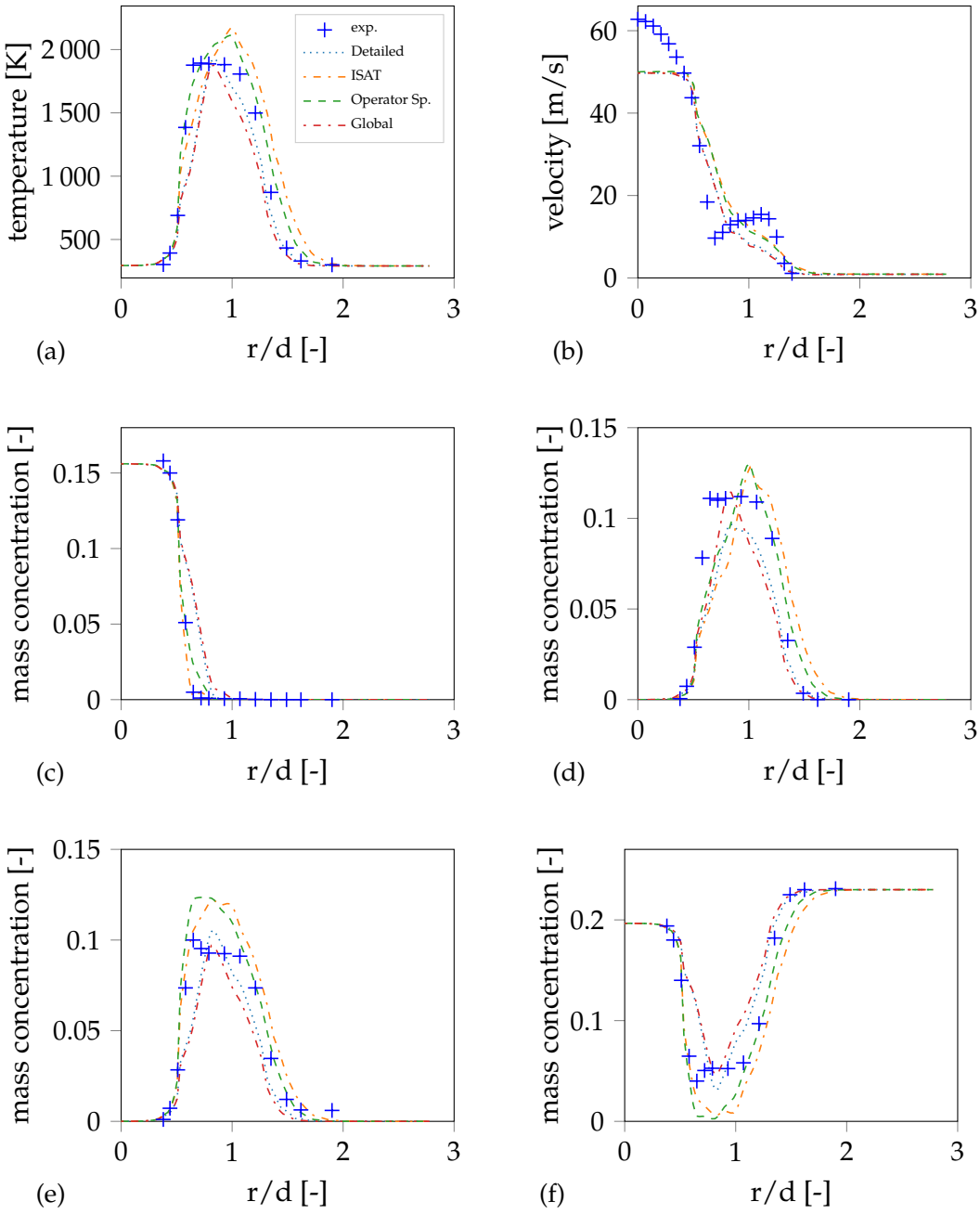

Figure A.26: Radial profiles comparing settings for simulations using GRI-3.0 at x/d=1 for (a) temperature, (b) velocity and species concentrations (c) CH_4 (d) CO_2 (e) H_2O (f) O_2

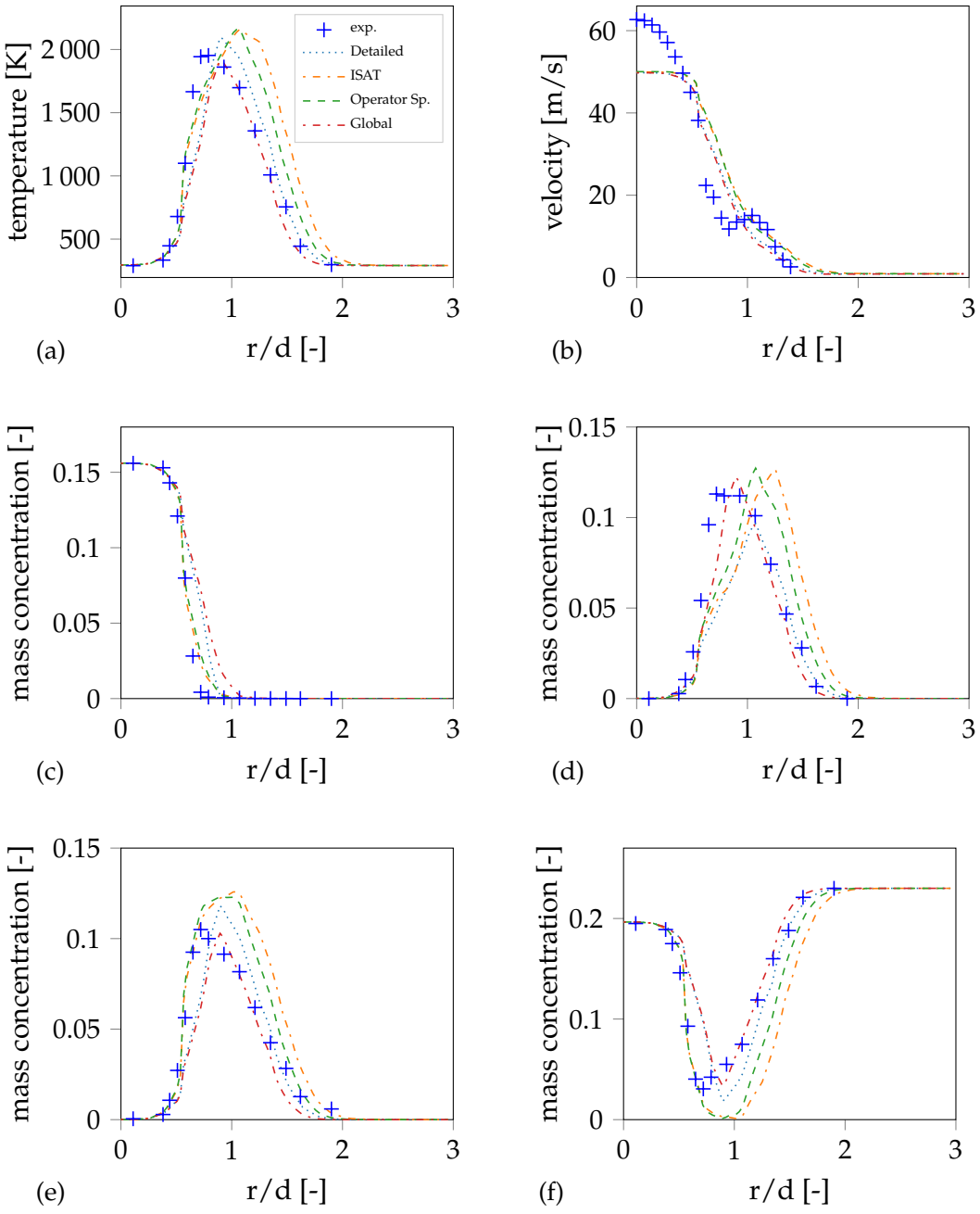

Figure A.27: Radial profiles at x/d=2 comparing settings for simulations using GRI-3.0 for (a) temperature, (b) velocity and species concentrations (c) CH_4 (d) CO_2 (e) H_2O (f) O_2

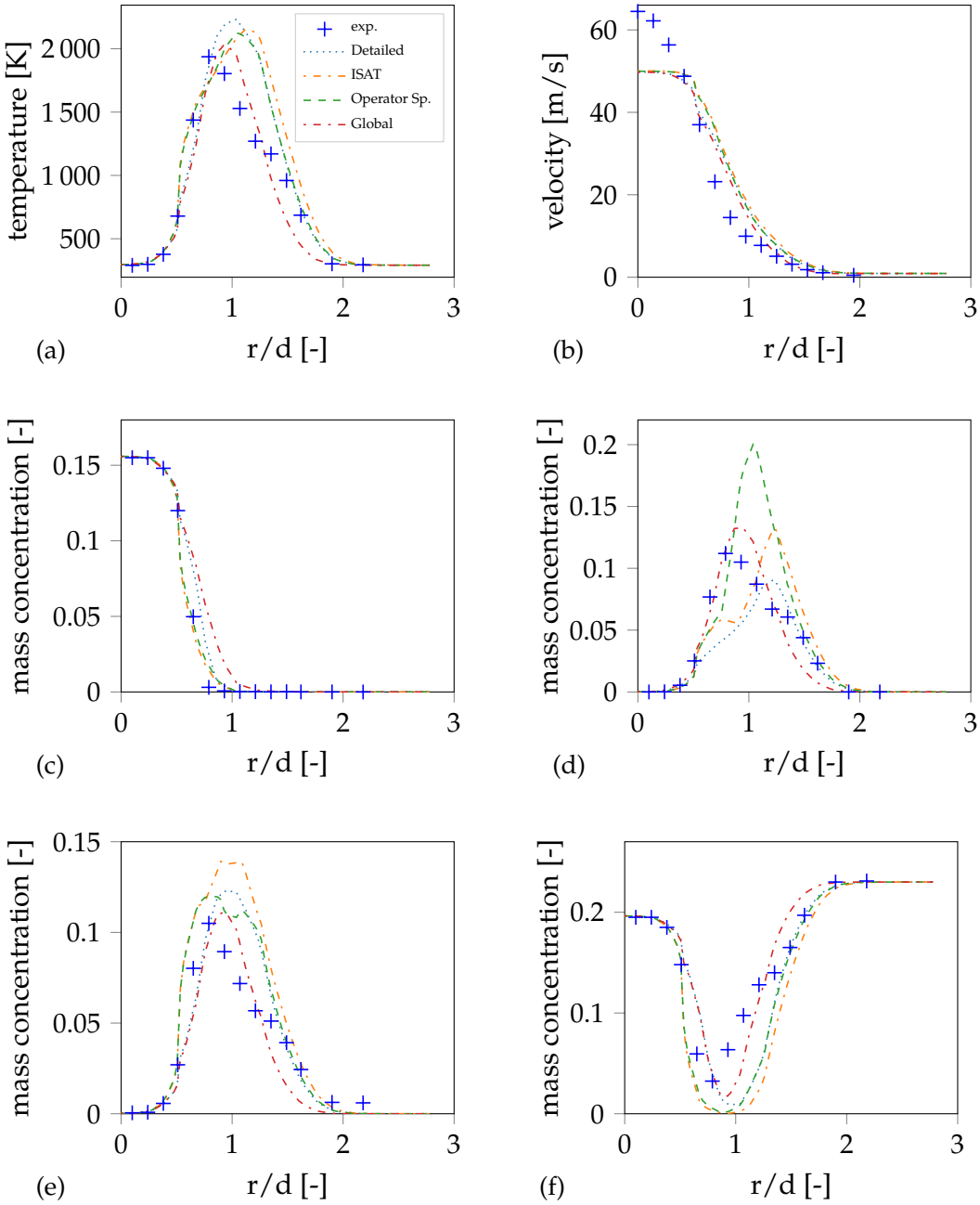

Figure A.28: Radial profiles at x/d=3 comparing settings for simulations using GRI-3.0 for (a) temperature, (b) velocity and species concentrations (c) CH_4 (d) CO_2 (e) H_2O (f) O_2

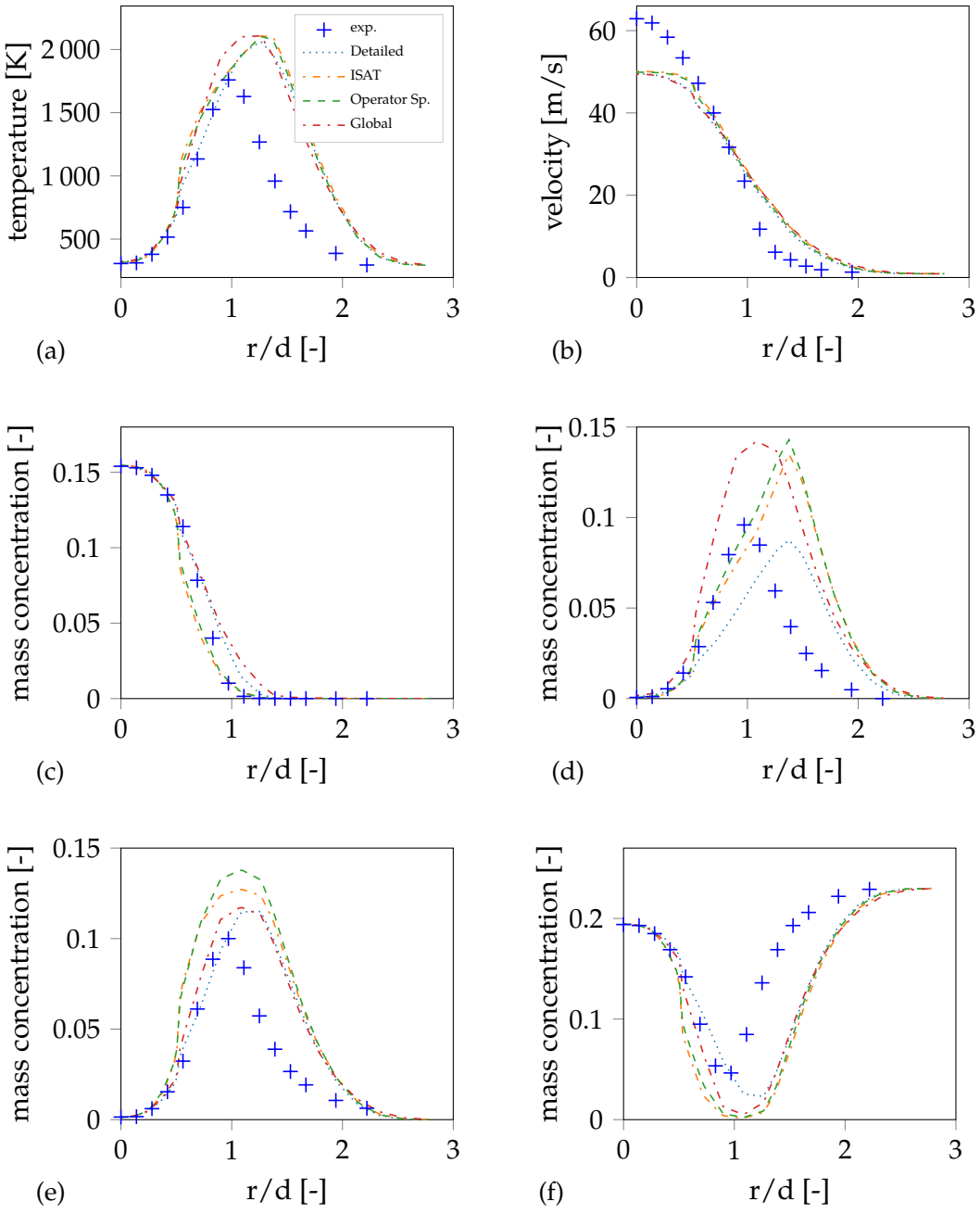

Figure A.29: Radial profiles at x/d=7.5 comparing settings for simulations using GRI-3.0 for (a) temperature, (b) velocity and species concentrations (c) CH_4 (d) CO_2 (e) H_2O (f) O_2

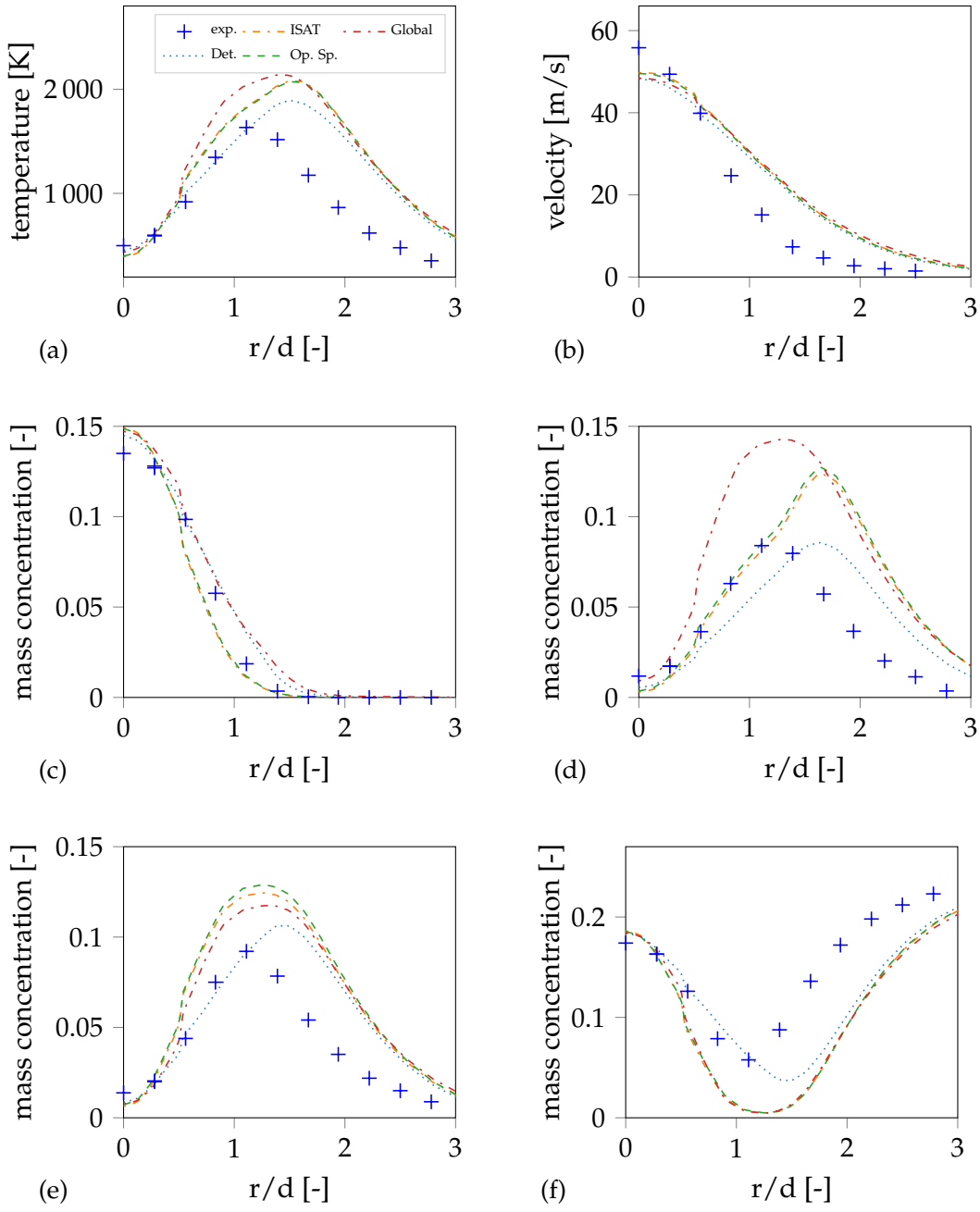

Figure A.30: Radial profiles at x/d=15 comparing settings for simulations using GRI-3.0 for (a) temperature, (b) velocity and species concentrations (c) CH_4 (d) CO_2 (e) H_2O (f) O_2

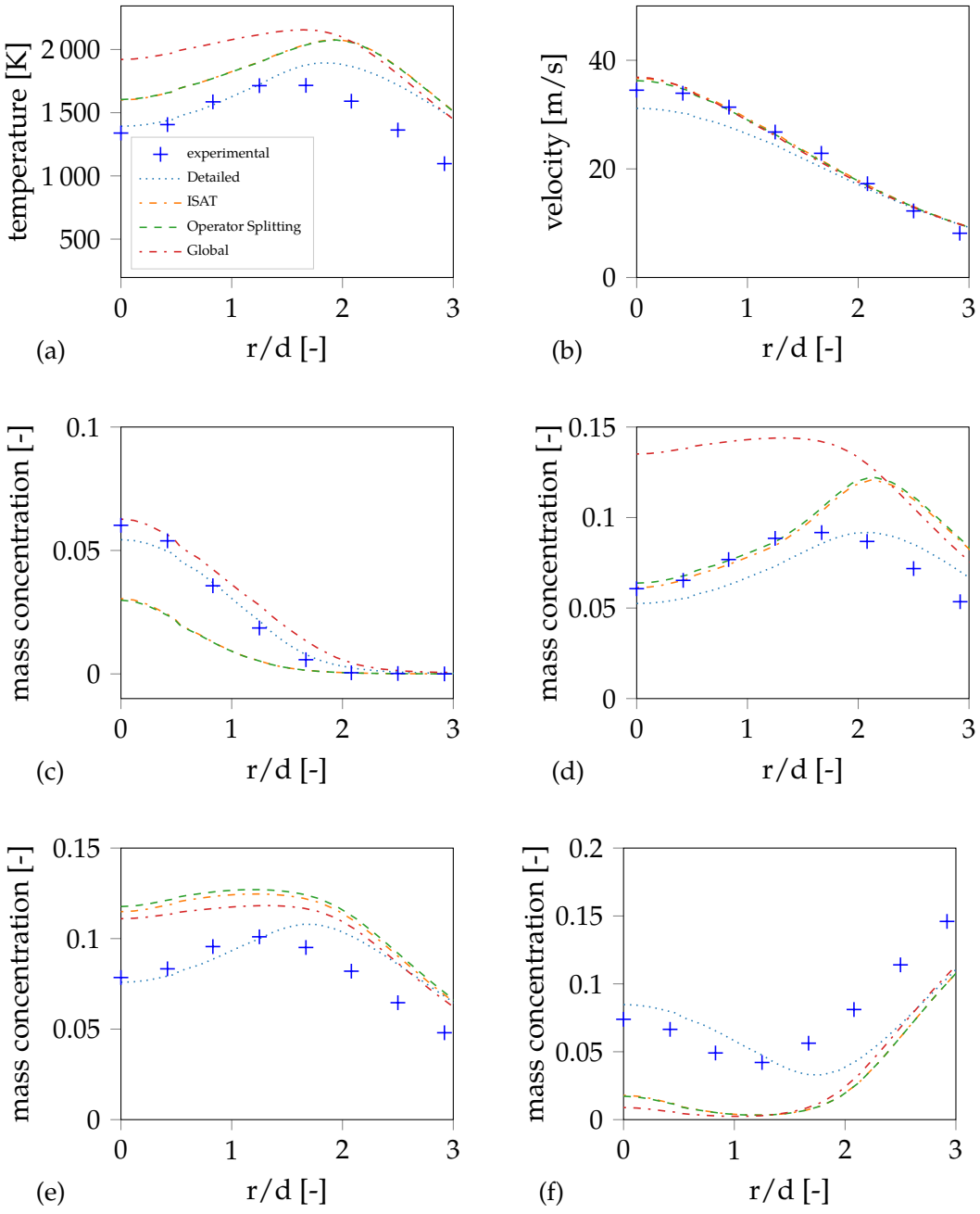

Figure A.31: Radial profiles at x/d=30 comparing settings for simulations using GRI-3.0 for (a) temperature, (b) velocity and species concentrations (c) CH_4 (d) CO_2 (e) H_2O (f) O_2

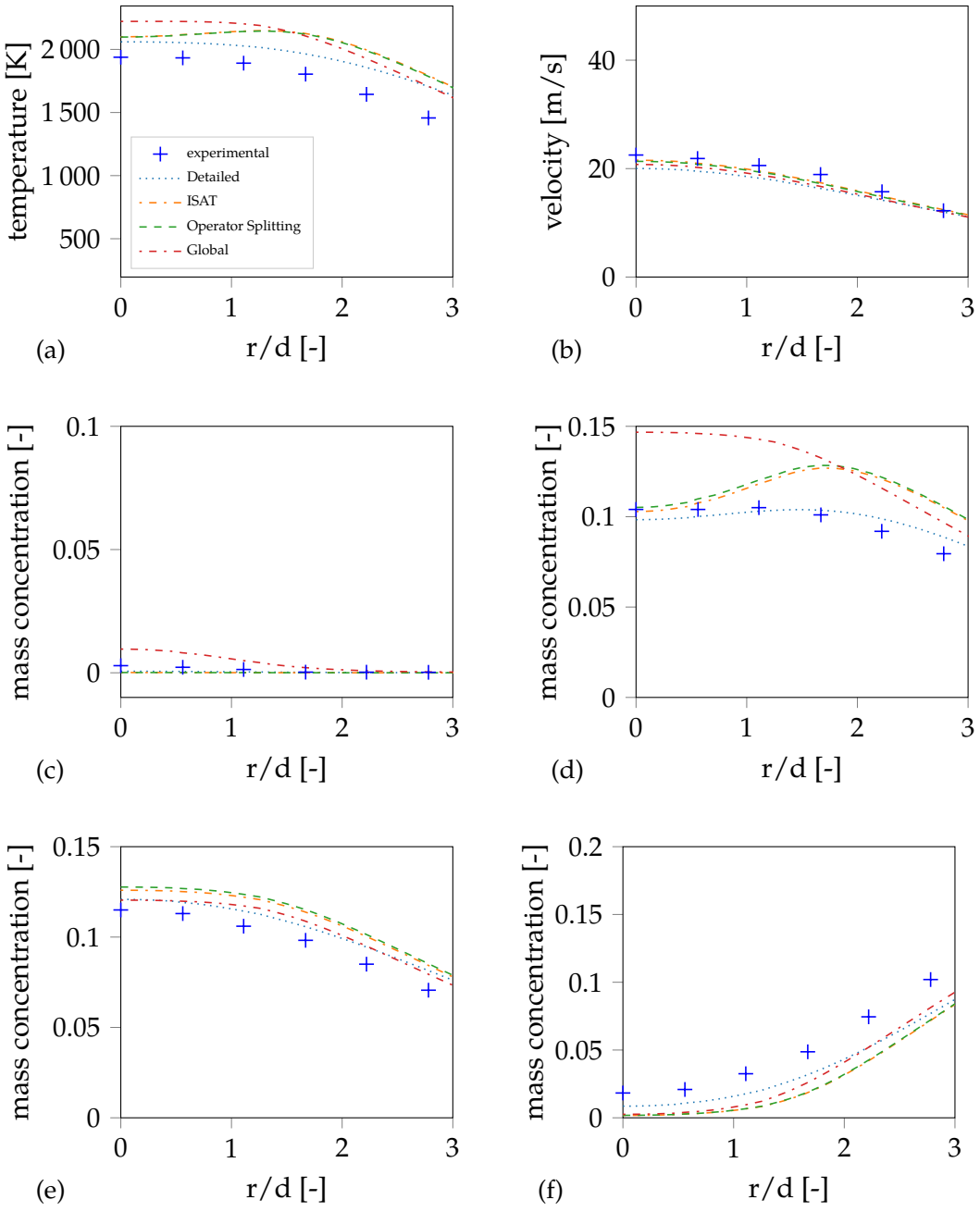

Figure A.32: Radial profiles at x/d=45 comparing settings for simulations using GRI-3.0 for (a) temperature, (b) velocity and species concentrations (c) CH_4 (d) CO_2 (e) H_2O (f) O_2

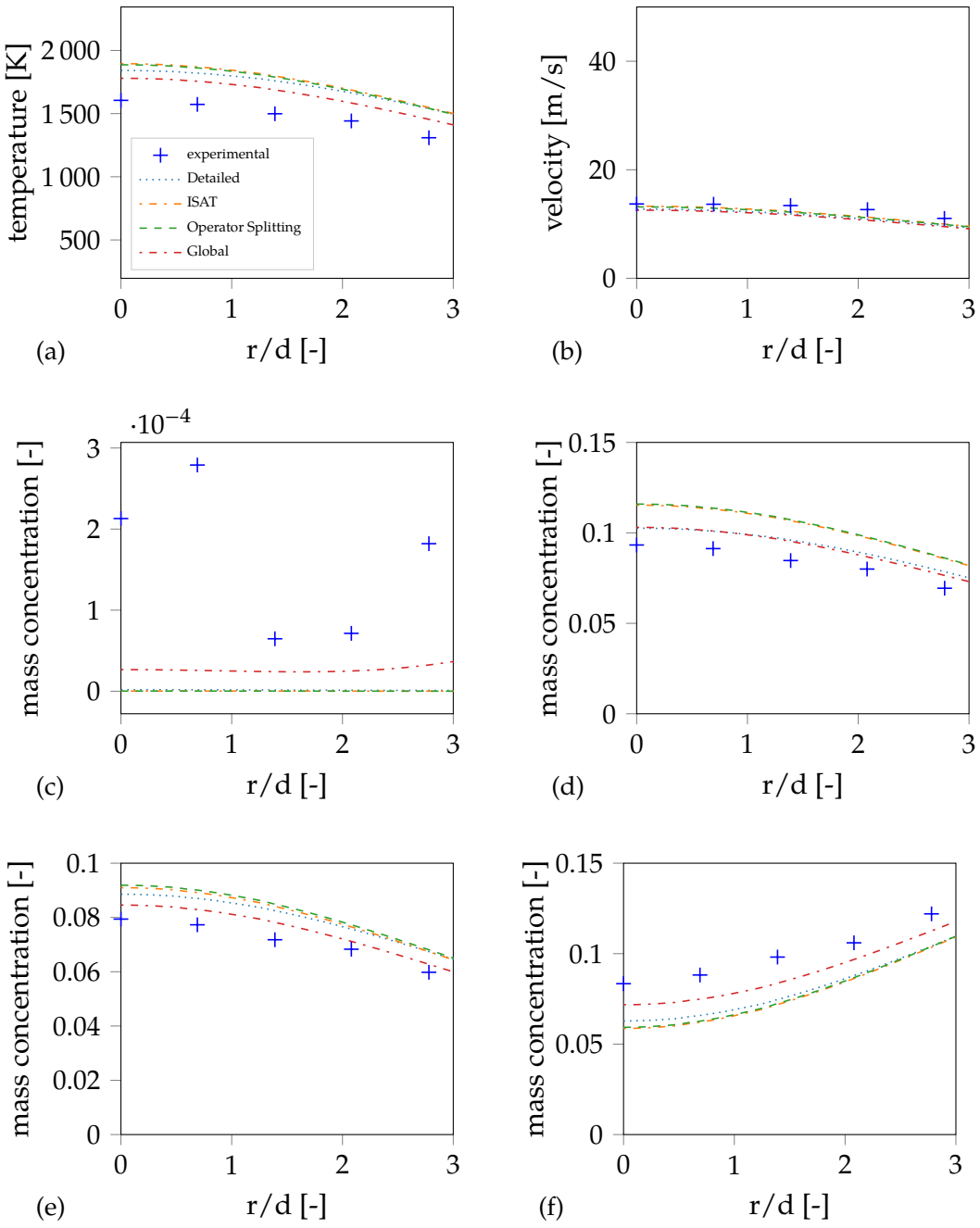

Figure A.33: Radial profiles at x/d=60 comparing settings for simulations using GRI-3.0 for (a) temperature, (b) velocity and species concentrations (c) CH_4 (d) CO_2 (e) H_2O (f) O_2

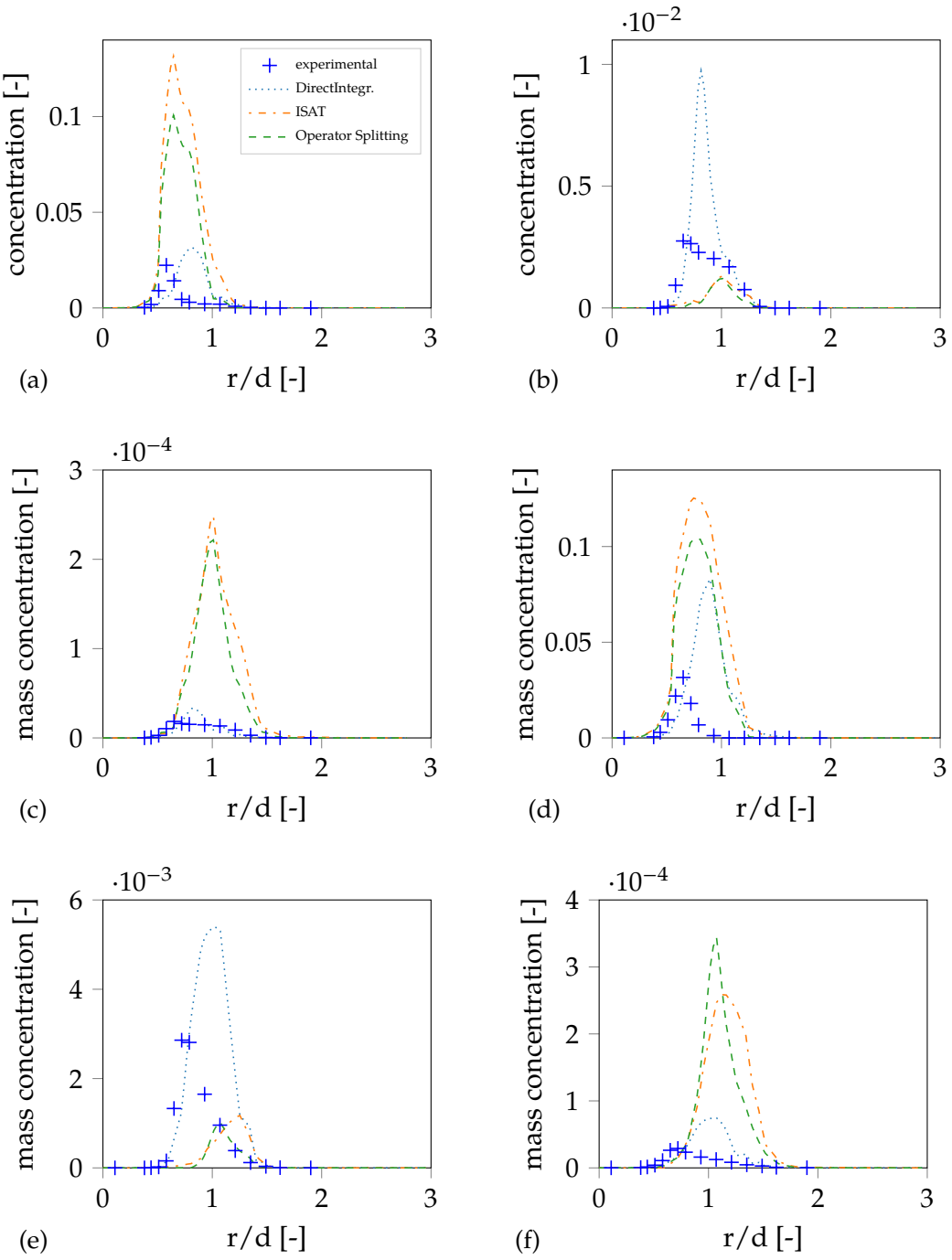

Figure A.34: Radial profiles at x/d=1 and x/d=2 comparing settings for simulations using GRI-3.0 for radical species (a) (d) CO, (b) (e) OH and (c) (f) NO

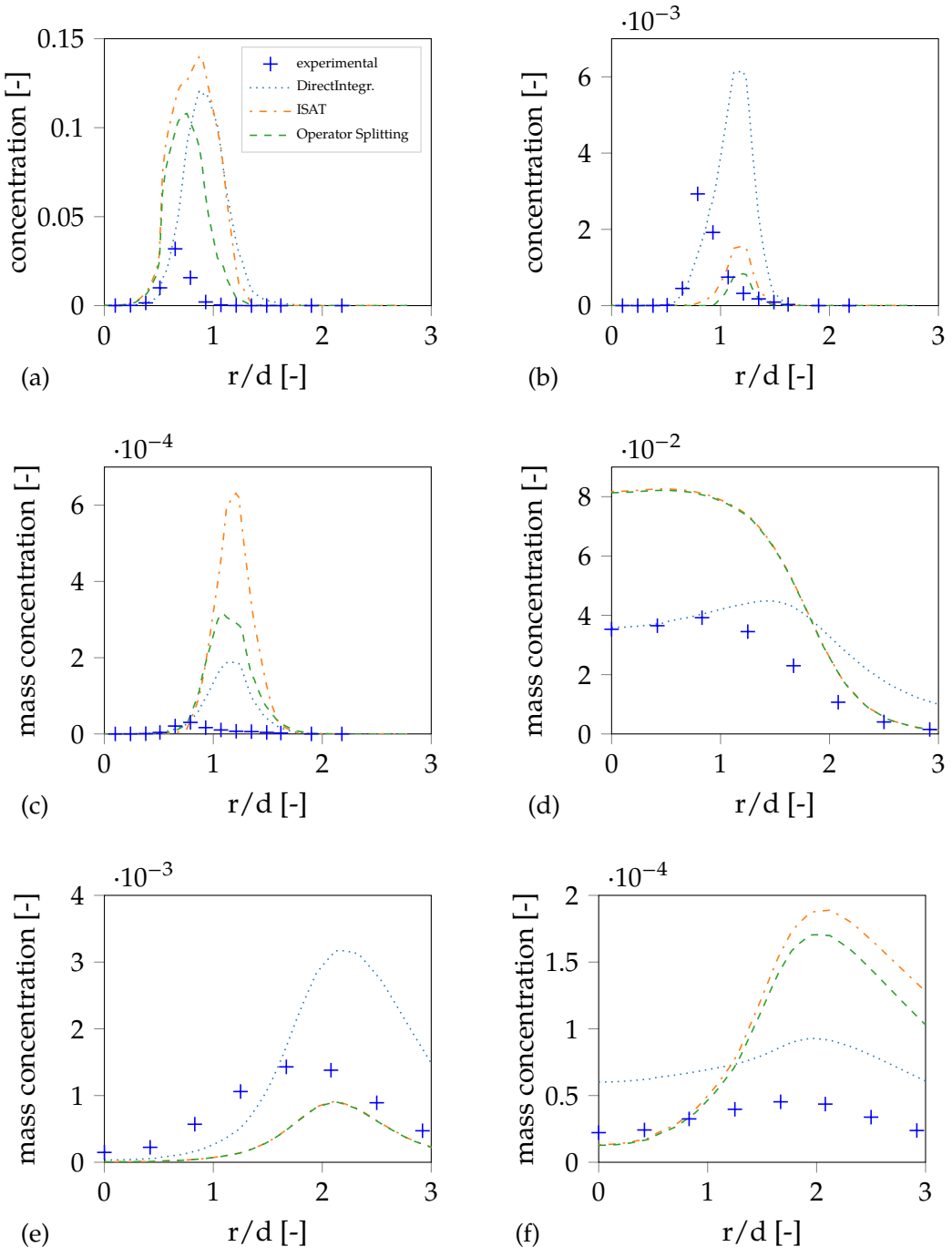

Figure A.35: Radial profiles at x/d=3 and x/d=30 comparing settings for simulations using GRI-3.0 for radical species (a) (d) CO, (b) (e) OH and (c) (f) NO

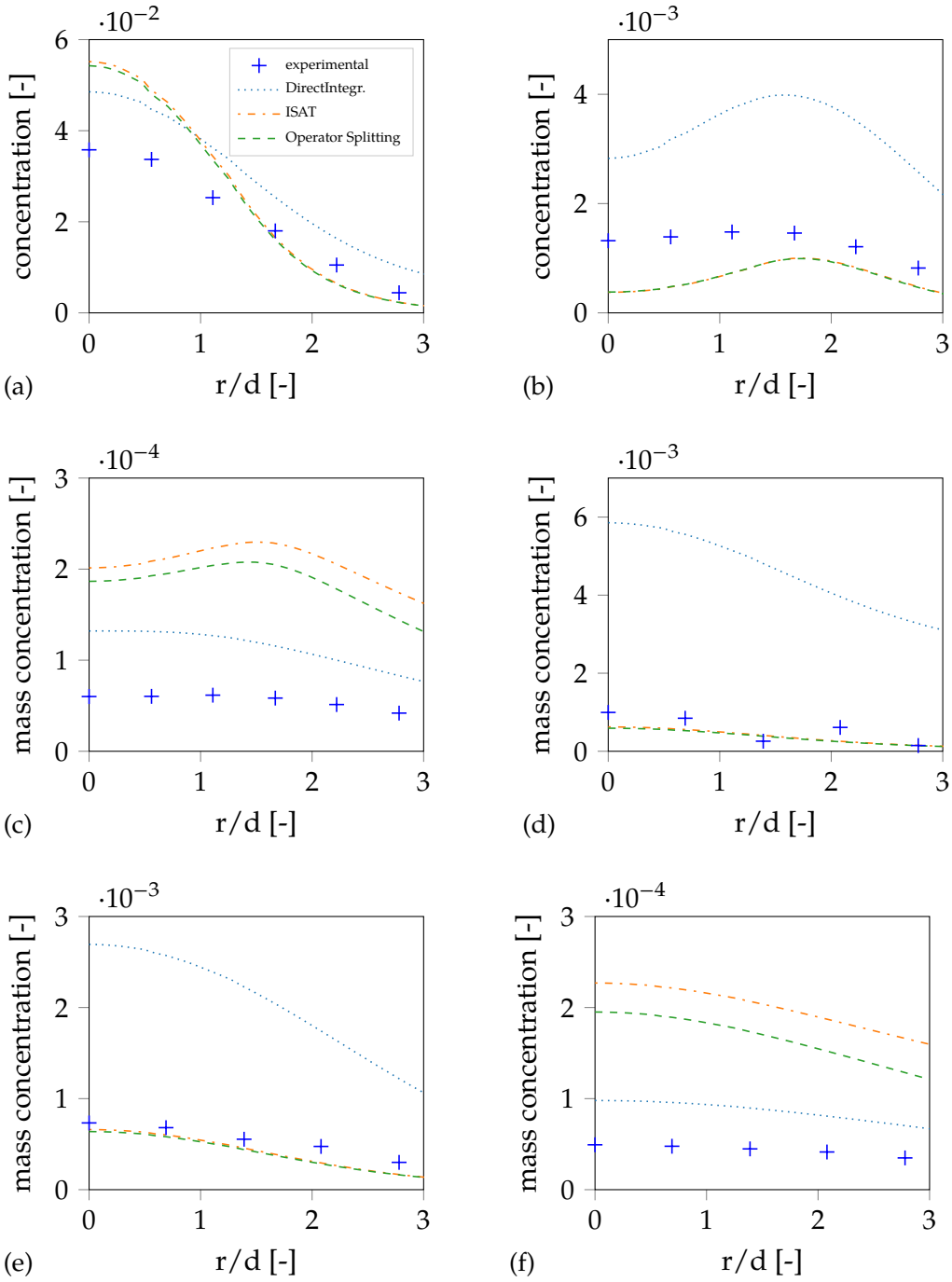

Figure A.36: Radial profiles at x/d=45 and x/d=60 comparing settings for simulations using GRI-3.0 for radical species (a) (d) CO, (b) (e) OH and (c) (f) NO

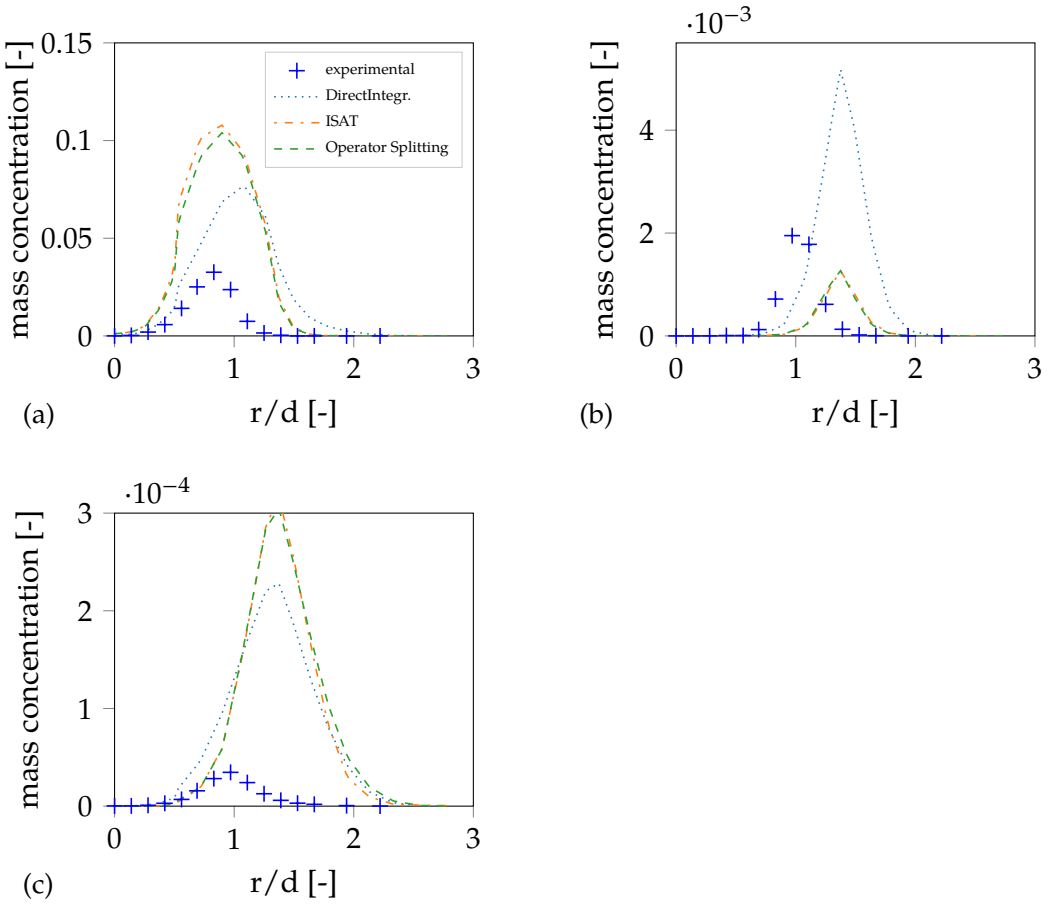

Figure A.37: Radial profiles at x/d=7.5 comparing settings for simulations using GRI-3.0 for radical species (a) CO, (b) OH and (c) NO

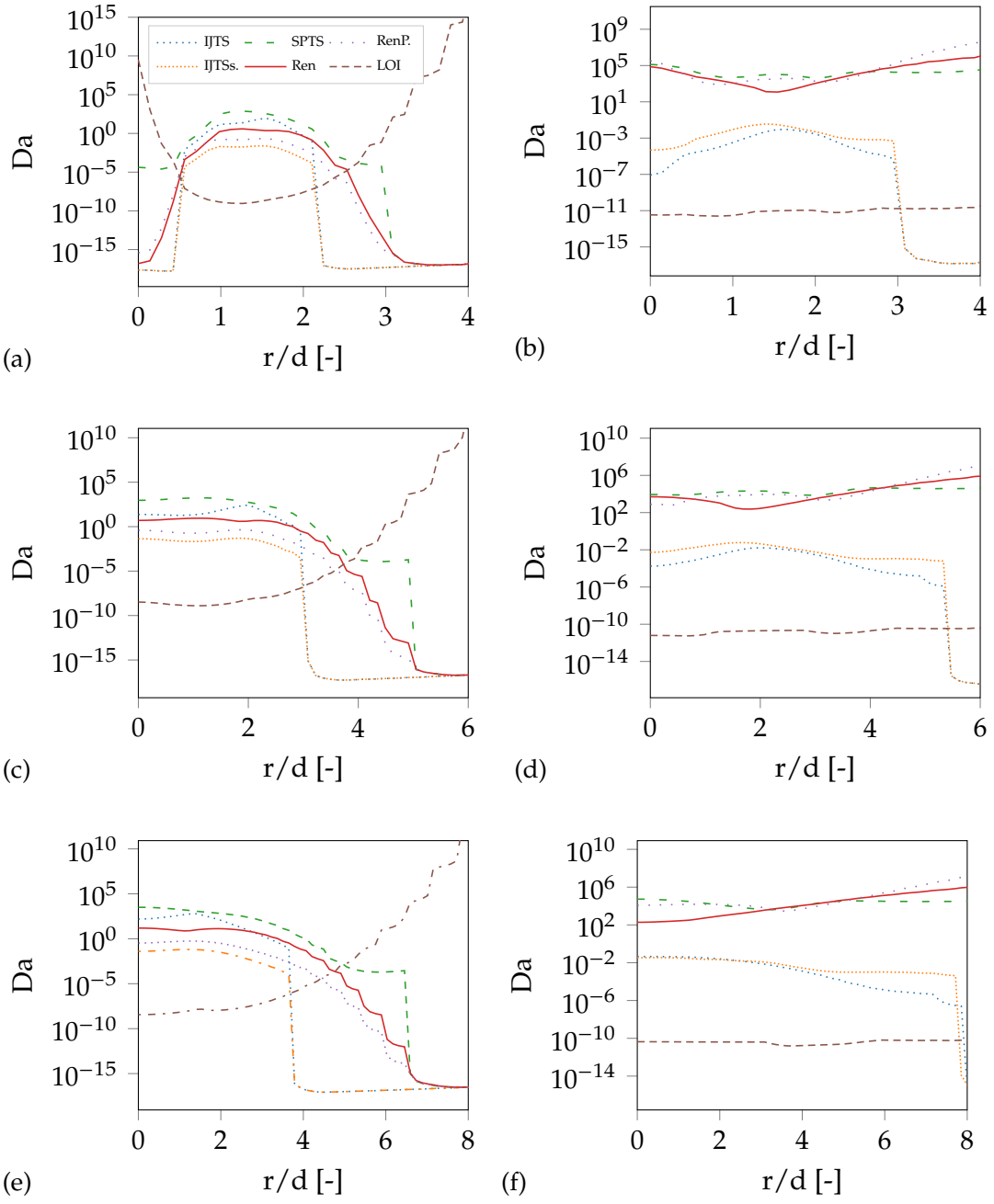

Figure A.38: Damköhler number for global and detailed chemical mechanisms respectively at (a) (b) x/d=15, (c) (d) x/d=30 and (e) (f) ad x/d=45